博士論文

# A study on the focused ion beam sputtering for the development of 3D shave-off SIMS

（三次元シェーブオフ二次イオン質量分析法の開発に向けた収束イオンビームスパッタリングの研究）

姜　少熙

# TABLE OF CONTENTS

CHAPTER

**I. INTRODUCTION** .......... 1

1.1 Three-dimensional analysis of micro sample internal structure.......... 1

1.2 (Ga) Focused ion beam SIMS .......... 5

1.2.1 Secondary ion mass spectrometry in surface analysis .......... 5

1.2.2 Operation modes of SIMS analysis.......... 9

1.2.3 Components of FIB-SIMS apparatus .......... 10

1.3 3D Shave-off method .......... 15

1.3.1 Shave-off method .......... 15

1.3.2 Development of shave-off method .......... 16

1.3.3 New 3D shave-off method .......... 17

1.4 Sputtering .......... 20

1.4.1 Sputtering mechanism .......... 20

1.4.2 Sputtering yield .......... 21

1.4.3 Distribution of sputtered particle .......... 22

1.5 Monte Carlo Simulation .......... 23

1.5.1 SRIM/TRIM .......... 24

1.5.2 SDTrimSP .......... 24

1.6 Objective of this study .......... 24

1.6.1 Goal of 3D shave-off SIMS .......... 25

1.6.2 Objective of this study .......... 26

1.7 References .......... 27

CHAPTER

**II. ANALYSIS OF CROSS-SECTIONAL SHAPE** .......... 31

2.1 Introduction .......... 31

2.2 Experiments.......... 33

2.2.1 Sample preparation.......... 33

2.2.2 Scan condition .......... 34

2.3 Results and discussion.......... 36

2.3.1 Analysis of cross-sectional shape ..... 36
2.3.2 Simulation of particle bombardment ..... 39
2.4 Conclusion ..... 43
2.5 References ..... 44

**CHAPTER**
**III. INFLUENCE OF THE SHAVE-OFF SCAN SPEED ON THE CROSS-SECTIONAL SHAPE** ..... 45
3.1 Introduction ..... 45
3.2 Experiments ..... 46
3.3 Results and discussion ..... 48
3.3.1 Influence of the shave-off scan speed on cross-sectional shape ..... 48
3.3.2 Sputtering yield ..... 51
3.3.3 Assumption of Beam profile ..... 55
3.4 Conclusion ..... 58
3.5 References ..... 59

**CHAPTER**
**IV. ANGULAR & ENERGY DISTRIBUTION OF SPUTTERED PARTICLES** ..... 60
4.1 Introduction ..... 60
4.2 SDTrimSP simulation with shave-off condition ..... 61
4.2.1 Method ..... 61
4.2.2 High incident energy ..... 64
4.2.3 High angle of incidence ..... 65
4.3 Angular distribution of sputtered W particles ..... 70
4.4 Energy distribution of sputtered W particles ..... 74
4.5 Conclusion ..... 76
4.6 References ..... 77

**CHAPTER**
**V. SIMULATION OF SECONDARY IONS POSITION ON THE DETECTOR** ..... 79

5.1. Introduction ........................................................................................ 79
5.2. Simulation condition .................................................................................. 80
5.2.1 Target ......................................................................................... 80
5.2.2 Sputtering position on the target ....................................................... 80
5.2.3 Procedure of simulation. .................................................................. 82
5.3 Simulation of surface erosion process........................................................ 85
5.3.1 Procedure......................................................................................... 85
5.3.2 Cross-sectional shape ........................................................................ 88
5.4 Monte Carlo simulation for sputtering process .......................................... 94
5.5 Simulation of secondary ion trajectories..................................................... 94
5.5.1 Position on the mass detector of the secondary ions.......................... 94
5.5.2 Improvement resolution of secondary ion distribution ...................... 99
5.6 Conclusion................................................................................................. 103
5.7 References ................................................................................................. 105

**CHAPTER**
**VI. CONCLUSION** ........................................................................................ 106
6.1 Conclusion................................................................................................. 106
6.2 Summary ................................................................................................... 107

APPENDIX ....................................................................................................... 110
PUBLICATIONS ............................................................................................... 112
ACKNOWLEDGEMENTS ................................................................................ 113

# CHAPTER I

# INTRODUCTION

## 1.1 Three-dimensional analysis of micro sample internal structure

Over the past several years, surface analysis has been an essential technique in research manufacture and quality control to develop and produce for high innovation technologies such as metal manufacture, chemicals, mechanical engineering, electronics, electric vehicles, and aircraft, etc. [1.1]. The outermost of a solid matter is the first part of interacting and being affected from the outside condition. Therefore, the behavior and properties of the surface of material play an important role to the whole of the solid matter. The analysis of the surface materials is required to understand the characteristics of matter, and it has been developed with several techniques [1.2, 3].

However, increasing interest in the development of new materials with advanced and their application, analysis of interior information has also been demanded to take necessary as well as surface analysis. In particular, for instance, the microcapsules which are composed of different material with core and shell cannot obtain sufficient capability for the application by only the surface analysis due to depending on the encapsulated core material (Fig. 1.1). The investigation and revelation of hidden interior information of material are required for research and development and quality management of matter in many techniques.

In many cases, two-dimensional (2D) images which are projected or detected them using several techniques are insufficient to investigate the relationship between the 3D structure and the function of precision objects [1.4]. In recent decades, new technologies have emerged and improved to analyze internal microstructures with three-dimensional (3D) images such as confocal laser scanning microscopy (CLSM), micro-computed

tomography (Micro-CT), and secondary ions mass spectrometry (SIMS), etc. The 3D analysis for internal (interior, in-depth) information is a powerful technique to provide in a variety of valuable information for an internal defect, 3D distribution of chemical species, instance materials fraction, porosity, phase boundaries [1.5, 6]. Table 1.1 presents three typical three-dimensional analysis techniques [1.7-10].

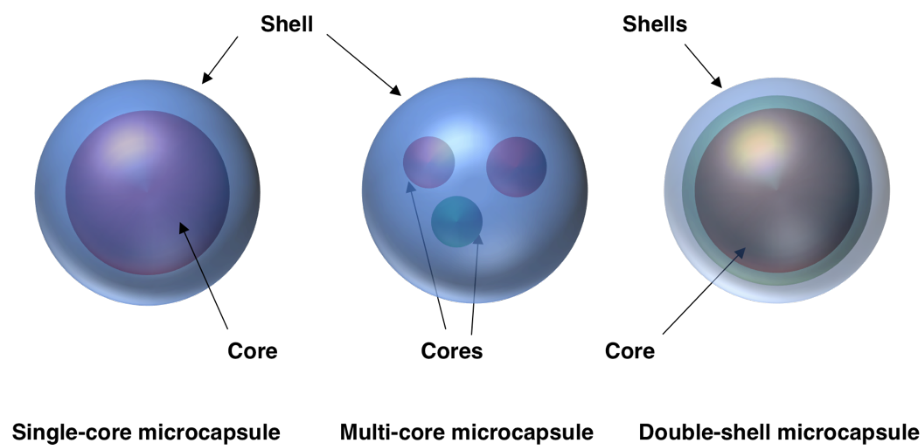


**Fig. 1.1 Types of microcapsules**

**Table 1.1** Three represent analysis method to analyze three dimensional analysis; CT [1.8], CLSM [1.9] and SIMS [1.10].

| Technique | Source | Resolution (μm) | Advantages | Disadvantages |
|---|---|---|---|---|
| CT | X-ray | 1 | ■ Non-destructive 3D imaging<br>■ Imagine in ambient environment | ■ Sample size normally around 1mm |
| CLSM (LCSM) | Laser | 0.18-0.25 (X,Y),<br>0.5-0.7 (Z) | ■ Non-invasive optical sectioning<br>■ Shorter acquisition time | ■ Limited subsurface imaging depth<br>■ Low resolution |
| SIMS (Dynamic) | Ions | 0.02-1 (X,Y),<br>0.01- 0.02 (Z) | ■ High resolution (~10 nm)<br>■ Depth resolution of 2-5 nm possible | ■ Destructive<br>■ Unevenly milled surfaces |

- X-ray Computed tomography (CT)

X-ray CT is widely used to obtain 3D images in medical, biological, zoological and other material science. CT is a technique using the X-ray radiation through penetrate an object. It acquires 2D projections from the X-ray radiation at many orientations, and these images will reconstruct to a 3D image. It allows visualizing internal structure of objects non-destructively without preparation [1.3, 11]. Nano-CT is capable of fine resolution (0.1 μm) with faster scanning speed, but the size of the sample should be in hundreds of micrometers [1.4]. Recently laboratory-based CTs which are able to scan samples at a sub-micron and nano-scale resolution [1.12] are also reported, but still, the X-ray CT technique is suitable with sample volumes ranging from tens of $\mu m^3$ to tens of $cm^3$.

- Confocal laser scanning microscopy (CLSM)

CLSM (or called Laser scanning microscope, LSM) is an optical technique used a highly focused laser beam as a light source for obtaining images from selective depths formed only with in-focus information [1.3, 5]. The laser beam scans over and into the sample by changing the focus, a series of two-dimensional images obtained at various depth in the sample have emerged to 3D reconstruction image. The CLSM which has been extensively used for imaging the internal structure specific in medicine and biology is direct and non-invasive [1.6, 7]. CLSM is able to image the internal structure without the need for physical sectioning. However, in the CLSM, the internal structure can analyze only substrates that penetrate with lasers, and it has low resolution due to the diffraction of light when the laser beam passes through the sample. X, Y and Z resolution can be $\leq 0.2$ μm, and $\leq 0.5$ μm, respectively, it is insufficient to analyze the micro-sample.

- Secondary ion mass spectrometry (SIMS)

SIMS is a powerful mass spectrometry technique to provide the 3D images of surface and subsurface with high sensitivity as well as good spatial resolution. Surface information of the sample is provided with lateral distribution as 2D images, and these are able to generate a 3D image in a stack as the series of 2D images. However, the conventional SIMS technique cannot reply topographical information of the sample surface due to detecting the secondary ions in a planar way without topography. For

accurate 3D data reconstructions and visualization, the SIMS is required to measure with an complementally technique which provides topographic information, for instance, atomic force microscopy (AFM) [1.13].

As above mentioned there are several methods for 3D internal analysis, but only SIMS can analyze specific and untargeted chemical information without additional preparations or measurements. In particular, the focused ion beam SIMS (FIB-SIMS) is possible to achieve superior pixel size than other techniques due to having fine beam size (~nm) and enable to identify smaller features in the structure that require a more accurate measurement of characteristics.

However, the conventional 3D SIMS images have a drawback to represent the laterally distorted element distributions due to the layer mixing and surface roughness by the differences of the sputtering yields. The shave-off method [1.14] has developed to improve on these drawback of conventional SIMS, it is expected the most suitable for the 3D internal analysis of micro samples. Therefore, our group proposed a new 3D shave-off SIMS and it will be discussed in the following sections.

## 1.2 (Ga) Focused ion beam SIMS

### 1.2.1 Secondary ion mass spectrometry in surface analysis

The secondary ion mass spectrometry (SIMS) is a most powerful tool for the analysis of the uppermost monolayer (~30 μm) of a solid sample [1.15]. Now SIMS has represented a commercialized technology that is widely used in both industry and academia for defining the isotopic, elemental, or molecular composition over highly localized microscopic regions within the surface of the solid matter. There are many methods for the analysis of the sample surface, and Table 1.2 compares the critical performance characteristics of the three typical surface analysis technique [1.16].

**Table 1.2** Techniques for surface analysis.

| | AES | XPS | SIMS (Dynamic) |
|---|---|---|---|
| Probe Species | Electrons | Photons | Ions |
| Detected Species | Auger Electrons | Photo-electrons | Secondary Ions |
| Spatial resolution | 0.01-2 μm | 10 μm | 10 μm |
| Depth resolution | 2-20 nm | 1-10 nm | 2-30 nm |
| Sampling depth | 0.5-7.5 nm | 0.5-7.5 nm | 0.1-1nm |
| Sensitivity | 0.1 to 1% | 0.1 % | < 1ppm |
| Elemental identification | All except H, He | All except H, He | All |
| Depth information | 1 to 5nm | 1 to 5nm | 1 nm |

- Auger electron spectrum (AES)

AES is a technique which uses an electron probe to generate Auger electrons at the surface. The most characteristic feature of AES compared to other analytical techniques is the high spatial resolution and depth resolution with several nanometers. However, the Auger electrons can generally only move a few nanometers in the solid, it is possible to detect elements only the information of the outermost the solid surface quantitatively [1.17].

- X-ray photoelectron spectroscopy (XPS)

XPS uses the emission of electrons from atoms by absorption of photons (photo-electrons). The XPS technique is one of the most widely used surface analysis methods today, and it obtains not only the element information but also the chemical bonding state of each element leading to the estimation of the compounds constitution [1.18]. The relative sensitivity coefficient is introduced in the quantitative analysis by XPS, and the detection limit for the element having high sensitivity reaches about 0.1 at%.

- Secondary ion mass spectrometry (SIMS)

SIMS technique uses the energetic primary ions beam to sputter the sample surface. In this process, several particles (such as photons, electrons, neutral atoms, molecules, and secondary ions) are created, and the secondary ions are analyzed and detected in a mass spectrometer. Fig. 1.2 has schematically illustrated ion bombardment and the main components found in a SIMS instrument. It can detect almost all elements include $H^+$ ions, isotopes of all elements, and it is a unique capability of SIMS. Moreover, the dynamic SIMS has not only excellent detection sensitivity (down to ppm) with very low detection limits than other techniques but also can confirm the presence of certain characteristic elements [1.10].

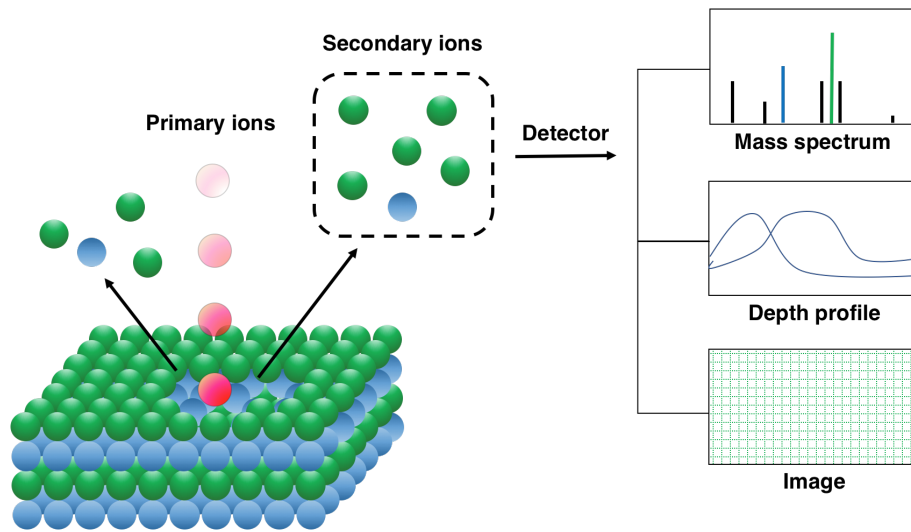


**Fig. 1.2 Principle of SIMS technique.**

The advantages of SIMS are summarized as follows

1. All elements (H-U) are detectable.
2. Isotopes can be distinguished.
3. High sensitivity and high dynamic range, and extensive detection limits of many elements/molecules. (ppm level for most elements and ppb atomic for favorable elements.
4. High spatial resolution of 1um depending on primary ion source and high depth resolution (2-5 nm possible, and 10-20 nm typical).

## 1.2.2 Operation modes of SIMS analysis

The analyzed secondary ions provide the surface analytical information as mass spectra, depth profiles, and ion imaging. Depending on the analytical information, there are two kinds of operation modes of SIMS: Static SIMS (Fig. 1.3(a)) and Dynamic SIMS (Fig. 1.3(b)) [1.19].

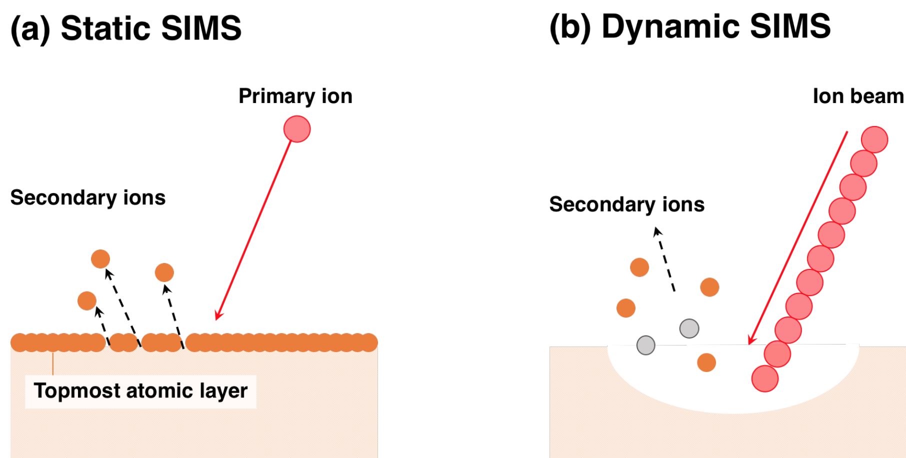


**Fig. 1.3 SIMS operation modes. (a) Static SIMS. (b) Dynamic SIMS.**

- Static SIMS

In static SIMS, it is used to get the mass spectrum of uppermost monolayer analysis. In order to achieve the original surface information, the primary ion beam is used a very low current density of under $10^{-9}$ A/cm$^2$ to minimize surface damage. The static SIMS usually composed with a pulsed ion beam and a time of flight mass spectrometer has been applied for characterization of metals, semiconductors, and polymer surfaces, and so on.

- Dynamic SIMS

For the dynamic SIMS, a high primary ion beam intensity (up to some A/cm$^2$) is used to get the depth profiling with a high sputtering rate. During the sputtering process, the top few monolayers of the sample are removed by the high energy primary ion beam. The ion beam produces a crater steadily deeper into the sample depth, and the SIMS

can achieve the depth profiles by monitoring the secondary ion count rate as a function of time. This depth information is particularly useful for the analysis of layered structures such as in the semiconductor industry. The dynamic SIMS instruments usually used magnetic sector and quadrupole mass analyzers, and it can be achieved with high sensitivity (lower ppb range). Moreover, Dynamic SIMS with focused ion beam also uses to generate a secondary ion image for lateral distribution analysis of materials. A series of images combined with depth analysis are reconstructed into a three-dimensional (3D) map of the element distribution.

In this study, our shave-off SIMS apparatus is the dynamic SIMS type. It is suitable for obtaining high resolution of depth profiling and 3D images of a sample.

### 1.2.3 Components of FIB-SIMS apparatus

Generally SIMS apparatus consists of several components: (1) Vacuum system, (2) Sample insertion/manipulation system, (3) Ion sources, (4) Primary ion optics, (5) Secondary ion extraction and transfer optics, (6) Energy filter, (7) Mass spectrometer, and (8) Detector [1.19]. Figure 1.4 presents our FIB shave-off SIMS apparatus used in this study. The shave-off FIB-SIMS apparatus used the gallium(Ga) liquid metal ion source (LMIS) as an ion source, the Mattauch-Herzog double focusing magnetic sector as a mass spectrometer, and multichannel detector system. These three main components of our FIB-SIMS apparatus are described details as follows.

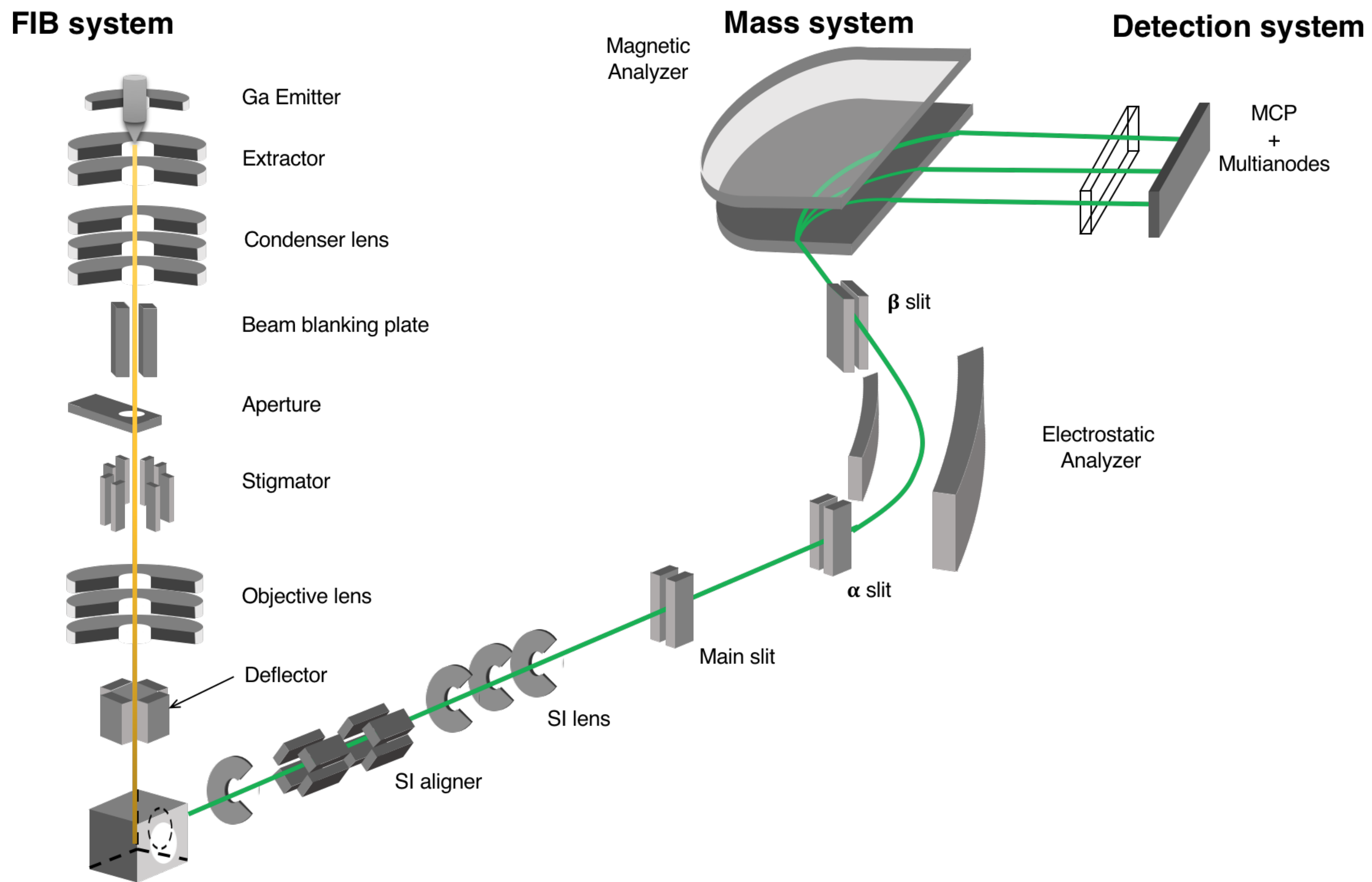


Fig. 1.4 Schematic illustration of a Focused ion beam SIMS for shave-off.

■ Focused ion beam system

A focused ion beam is equipped with a gallium liquid metal ion source (Ga-LMIS) for imaging, analysis, and sputtering etching. Because the gallium has a low melting temperature of 29.78° C with low volatility and low vapor pressure, the ion sources can produce a constant beam with limited heating and a long source lifetime with 300 μA-hours/mg [1.20]. Figure 1.5 shows the liquid metal ion source creates the primary ion beam. Heated liquid gallium in a Ga reservoir flows to the tungsten needle tip with a radius 2-5 μm (operation by 3.2A). The extractor (5-8 μA) generates an electric field in the order of $10^{10}$ $Vm^{-1}$ at the needle tip. Between the electrostatic force and the Ga surface has achieved equilibrium tension, it forms the liquid into a Taylor cone with an apex of ~5 nm in diameter. The $Ga^+$ ions are extracted by field evaporation, and the accelerated through an aperture towards the sample. (30 keV accelerated voltages). The vacuum of the ion beam system surround was kept $2 \times 10^{-7}$ Torr without beam emitting using ion pump, and the specimen chamber was kept $2 \times 10^{-7}$ Torr by turbomolecular pumps and rotary pumps. The primary ion beam is controlled and focused to the sample by ion optics system. The primary ion optics system consists of apertures, stigmators, alignments, electrodes, objective lens, deflector, and several sublens as shown in Fig. 1.4.

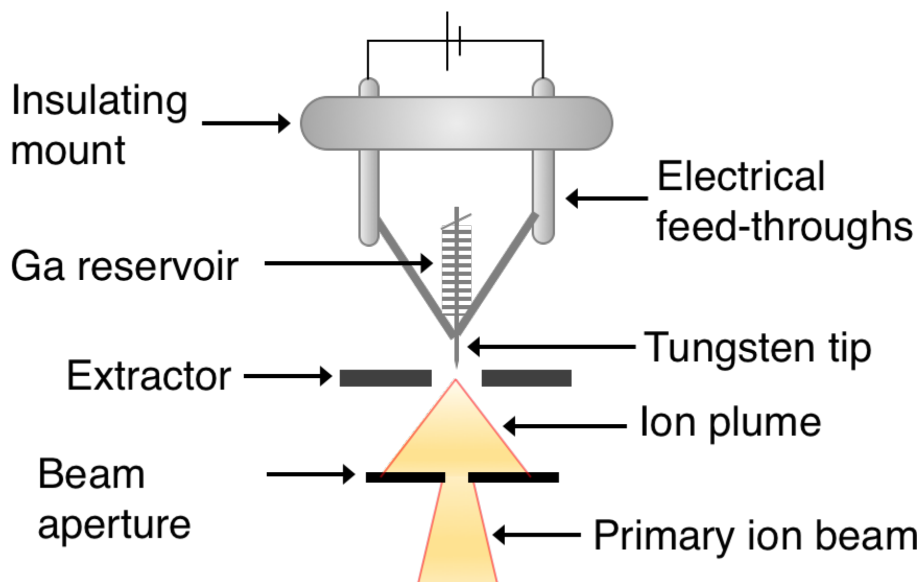


**Fig. 1.5 Schematic drawing of the liquid-metal ion source ($Ga^+$) in a FIB system.**

- Mass spectrometry

Mass spectrometry is a technique to separate the ions of the samples according to their mass-to-charge ratio. There are many types of mass analyzers in SIMS such as Time-of-flight, Magnetic sector, Quadrupole, and ion cyclotron resonance. Table 1.3 summarizes the common mass analyzers employed in use today.

In this study, the FIB-SIMS apparatus used a Mattauch-Herzog double focusing mass spectrometry for a high mass resolution. The Mattuch-Herzog double focusing mass spectrometer [1.21] is one kind of magnetic sector mass spectrometry which consists of a 31.8 degrees electrostatic sector and a 90 degrees magnetic sector (Fig. 1.6). In double focusing mass spectrometer, the electrostatic sector reduces the kinetic energy distribution of secondary ions. Hence the secondary ions successively pass through the magnetic field and are focused onto a point on a focal plane detector depending on *m/z*. This Mattuch-Herzog double focusing is known that can improve the resolving power of a magnetic sector instrument more than ten times, and attain the double-focusing over the total image plane resulting in resolving powers of $R > 10{,}000$ [1.22].

- Detector

The secondary ions focused by magnetic sector are electrically amplified to ~$10^6$ electrons by a microchannel plate (MCP), and a bunch of electrons reaches to one of the 120 channel multianode (plate) which applied the position of the mass range of 1:2 (total length of 80mm). The SIMS is equipped with a multichannel parallel detection system for high spatial resolution, the resolution of the detector is depended on the number of channels.

**Table 1.3** Mass analyzers for SIMS

| Type | Principle |
|---|---|
| Time-of-flight (ToF) | Time dispersion of pulsed ion beam; separation by time-of-flight |
| Magnetic sector | Deflection of continuous ion beam; separation by momentum in magnetic field due to Lorentz force |
| Quadrupole | Continuous ion beam in linear radio frequency quadrupole field ; separation due to stability of trajectories |
| Quadrupole Ion trap | Trapped ions; separation 3D radio frequency quadrupole field due to stability of trajectories |
| Ion cyclotron resonance | Trapped ions; separation by cyclotron frequency (Lorentz force) in magnetic field. |

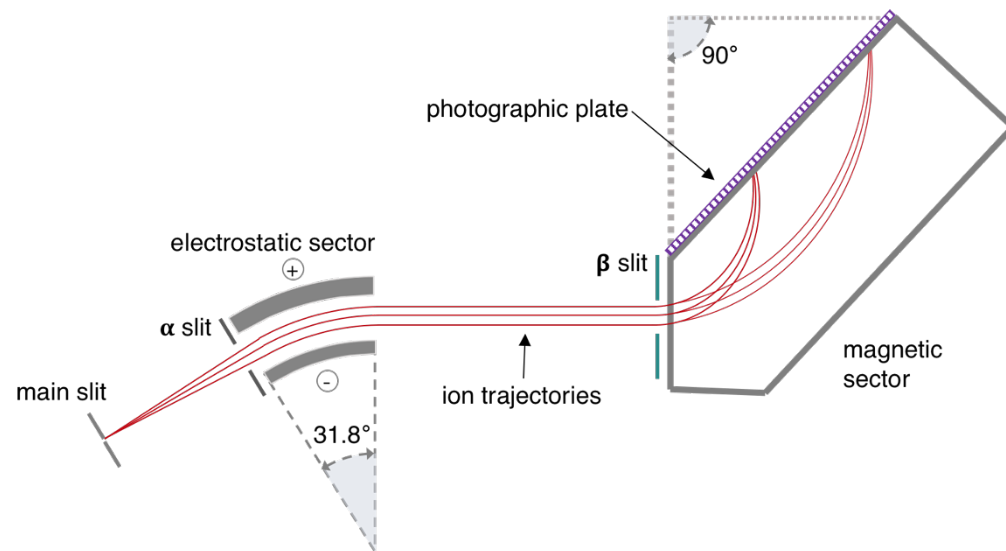


**Fig. 1.6** Schematic of Mattuch-Herzog double-focusing mass spectrometry.

## 1.3 3D Shave-off method

### 1.3.1 Shave-off method

The shave-off method was proposed for the analysis of uneven samples quantitatively [1.14]. Figure 1.7 compares the conventional raster scan mode and shave-off mode. In the commercial SIMS using raster scan mode, the primary ion beam scans over an area rapidly and repeatedly in both vertical and horizontal sweep as shown in Fig. 1.7(a). Therefore, if the surface of the sample is not flat, the conventional SIMS imaging has disadvantages that cannot provide precise topographical information of the sample. The secondary ions sputtered from the topmost planar surface are detected with neglect of the surface topography. For this reason, the SIMS imaging has been required using AFM images to correct topographic information [1.13].

However, in the shave-off method (Fig. 1.7(b)), the primary ion beam always scans over the edge of the sample with fast horizontal sweep and a 1000 times slower vertical sweep. The speed of vertical sweep is slow enough to entirely remove the sample from one edge to the other side, and the shave-off method can minimize the topographic effect, the sputter deposition, and knock-on mixing. Therefore, the shave-off method has a higher axial resolution of the sample and a reduction of shape effects [1.23].

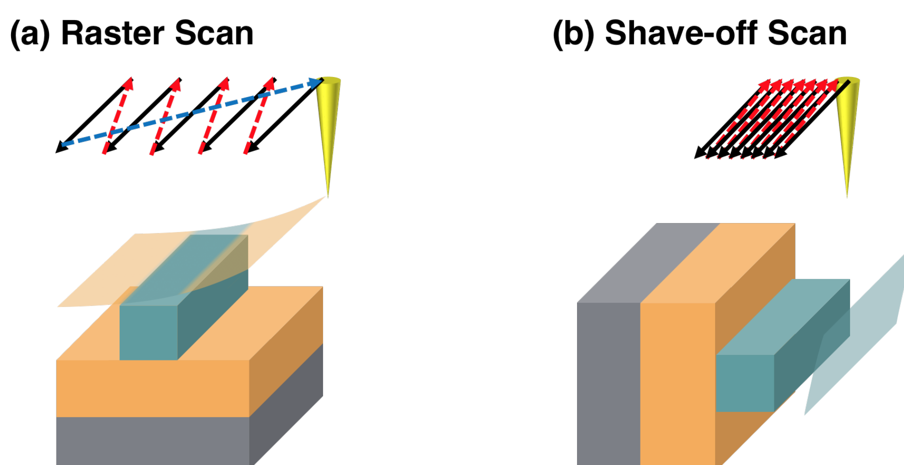


**Fig. 1.7** Illustration of a procedure of conventional raster scan mode (a) and the shave-off scan mote (b).

### 1.3.2 Development of shave-off method

The shave-off method had been developed with dimensional data acquisition.

At first, the shave-off method had been proposed for the high resolution depth profiling. The one-dimensional shave-off apparatus composed separate beam scanning system and mass spectrometry [1.24, 25], the data was able to achieve only depth information as a function of time (Fig. 1.8(a)) because of the FIB scanning system and data acquisition system function independently. And then our group developed the apparatus which can control the FIB system with synchronizing signal acquisition, called as a “multilane shave-off profiling”. This method can acquire the secondary ion signal as a function of the two-dimensional position of the beam as shown in Fig. 1.8(b). In the multilane shave-off system, the shave-off resolution on the X-axis and Y-axis has as high as the resolution of the raster scan, and the method has enabled the various materials and devices to provide more detailed elemental distribution information [1.26, 27].

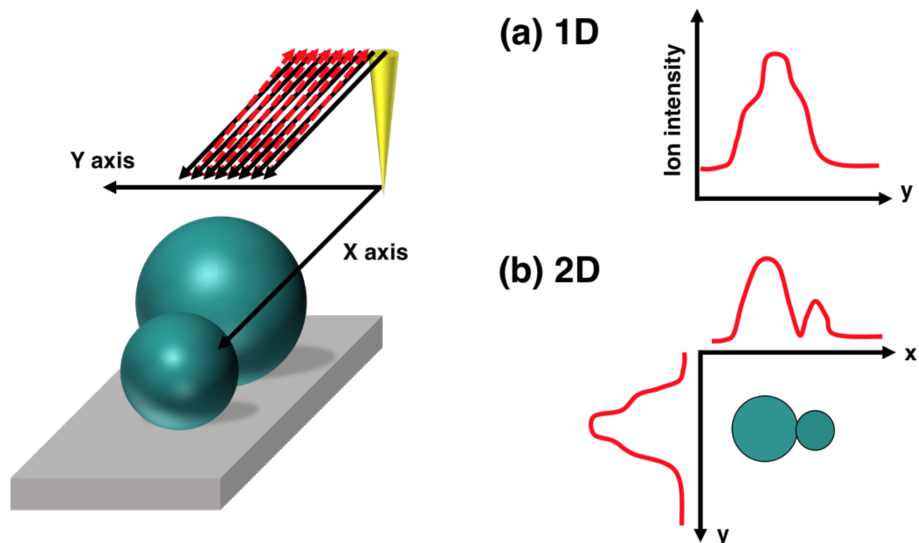


**Fig. 1.8** Data acquisition of the shave-off. (a) One-dimensional depth profiling. (b) Multilane (two-dimensional) depth profiling.

The three-dimensional (3D) shave-off method had developed using the dual beam system which composed of two gallium ion beams as a non-destructive microprobe and

the shave-off microprobe. Figure 1.9 illustrated the 3D shave-off method. In the 3D shave-off method, one FIB is applied for the mapping the sample surface (X-Y axis) as the non-destructive microscope with pulsed TOF-SIMS, another FIB uses for sectioning of the sample along the sample depth direction (Z-axis) with shave-off method [1.28]. However, this dual beam system has a long time to analyze the sample due to repeat the process with two ion beams and is also used raster scanning for mapping the sample images, and it means that also has the drawback of conventional SIMS as mentioned above

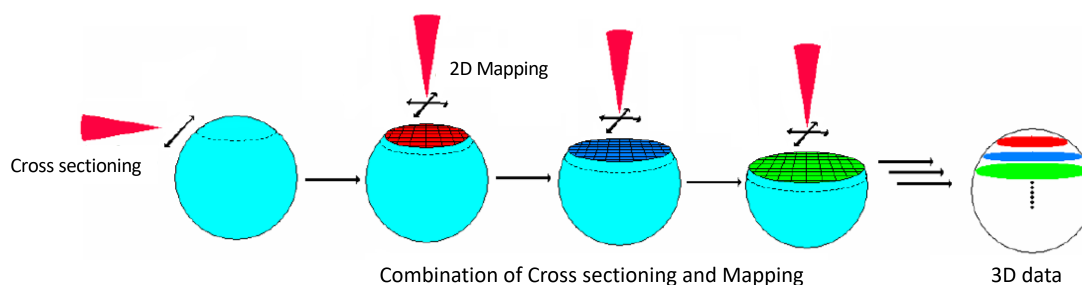


**Fig. 1.9** Schematic 3D mapping method for conventional 3D shave-off using dual beam system.

### 1.3.3 New 3D shave-off method

For the development of a three-dimensional shave-off method, our group has proposed to expand the 2D data acquisition of multilane shave-off profiling by adding the information of the sample depth. A concept of new 3D shave-off method is to obtain the mass information and the depth locational information at the multichannel parallel detector simultaneously. Z-axis of the detector is used to figure out the sample depth position. Figure 1.10(a) schematically shows the concept of the new 3D shave-off method. The sputtered secondary ions from the sample at the different depth position are magnified by cylindrical lens systems and are detected on the detector with maintaining location information.

To distinguish the depth information, the secondary ions which are sputtered from some μm unit of the sample should be magnified with units of some mm on the detector.

Figures 1.10(b) and 1.10(c) depict a schematic representation of the blueprint of the cylindrical lens system. The lens systems (L) demonstrate the enlargement process of the secondary ions only in the depth direction (Z-axis). The cylindrical lens which composed of the electrostatic lens systems has no interaction between the focused lens (F) and main slit (M) in X direction. Thus the secondary ions are converged to the main slit (position A) and then placed to the detector (D) as the same magnification under the effect of the electric field and the magnetic field. (Fig. 1.10(b)). Further, if the distance (b) from the lens to the detector is about several hundred to thousand times the distance (a) (Fig. 1.10(c)), it is possible to magnify the secondary ions to several mm units on the detector. This cylindrical lens system was simulated and evaluated using SIMION program by our members [1.29, 30]. From the simulation results, we could verify that the lens system magnifies only in the Z-axis of the sputtered secondary ions and transfer the ions to MCP of the mass analyzer with maintaining X and Y-axis scale. Using this principle, we will design and fabricate the electrostatic cylindrical lens for development the 3D shave-off SIMS.

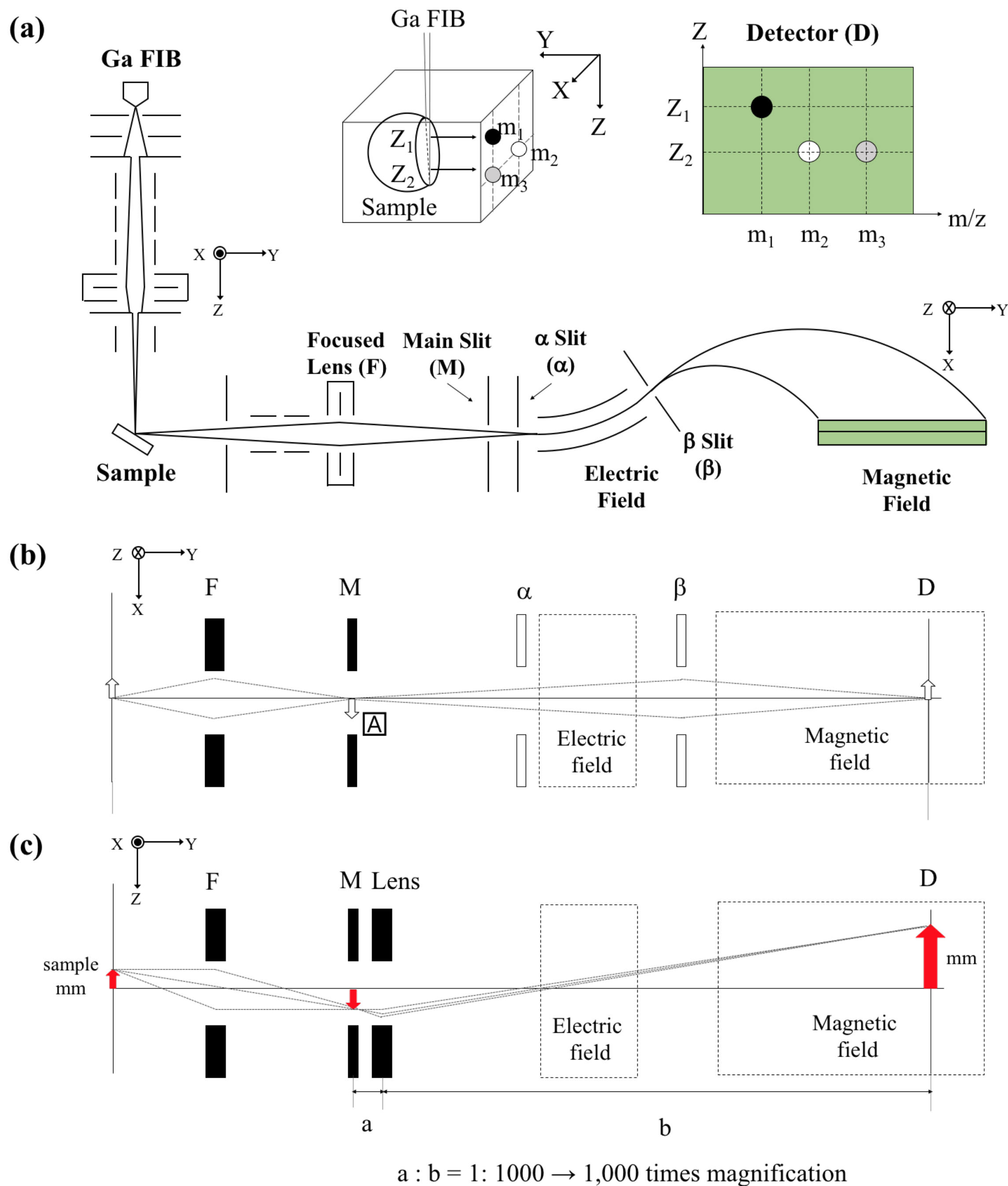


**Fig. 1.10** Schematic diagram of a secondary ion transport optical system in 3D shave-off analysis. (a) 3D shave-off SIMS apparatus. (b) Lens system in XY plane view. (c) Lens system in YZ plane view.

## 1.4 Sputtering

### 1.4.1 Sputtering mechanism

In SIMS, sputtering is a process that target atoms are emitted from the target surface by a collision of energetic incident ions (called primary ions). Figure 1.11 illustrates the collision cascade and sputtering process.

When the incident ions hit the target sample, a small fraction of ions are backscattered in collisions with surface atoms, and others penetrate through the target to other atoms along its path. The collision cascade occurs by the energy transferred to other target atoms. This process repeatedly occurs several times, and the recoiled atoms are given speed and removed from their original sites, collide with other atoms distributing the energy through a collision cascade. At this time, the surface atoms will be escaped from the sample surface if the transferred energy has larger than the surface binding energy, we called this state as "sputtering". The incident ions may be trapped and implanted in a target at the end of their binary collision until the energy of the ions has under 10 eV [1.31, 32].

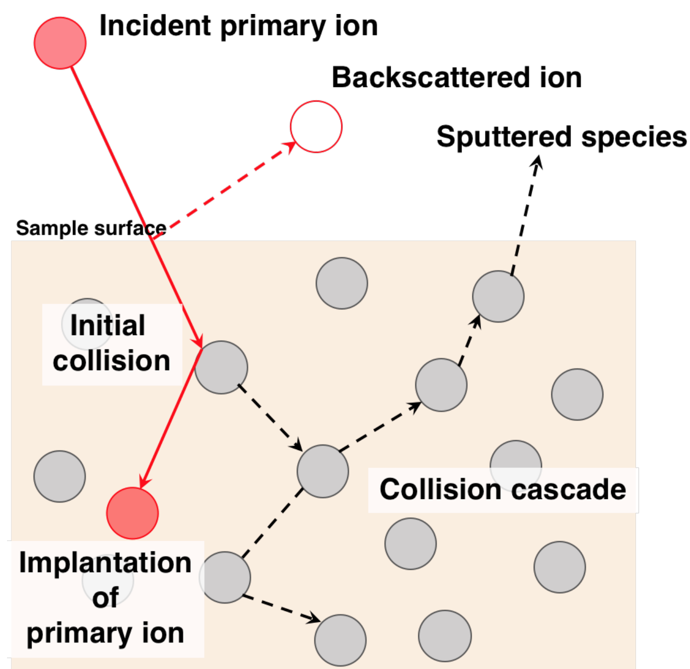


**Fig. 1.11 The collision cascade and sputtering process**

### 1.4.2 Sputtering yield

In the sputtering process, the sputtering yield ($Y$ = atoms/ion) has been described as the most important and widely investigated quantity parameter, defined as the mean number of sputtered atoms from the surface per incident particles. Most of the sputtered particle from metallic samples are composed of neutral atoms in the ground state, and some of part are ions and excited atoms, and clusters which are partly excited and ionized.

$$Y = \frac{Number\ of\ sputtered\ atoms}{Number\ of\ incident\ ions}$$

Several parameters affect the sputtering yield such as characteristics of primary ions (species, energy, and angle of incidence) and the target (mass, surface binding energy, crystallinity). The maximum value of sputtering yield was known that it depends on the bombarding particle energy, mass, and the surface topography [1.33-35]. However, once we determined the target to analyze with an instrument, only two parameters can be easily changed to improve sputtering yield; the energy of incident particles and the primary ion angle of incidence.

- Energy of incident particles

  Below threshold energy which is the minimum necessary energy transfer between the primary ion and the atoms of the target, sputtering does not take place. Above this energy, the sputtering yield is known that it increases with incident energy and reach a broad maximum in the energy region of 5 to 50 kV. At the region larger than these energies, the sputtering yield decrease due to the larger penetration of the ions into the target.

- Incident angle of incident particles

  The angle of incidence of primary ion is defined as the angle between incident ions and the line perpendicular to the surface at the point of incidence. The angle of incidence is a strong function to change the sputtering yield of the sample materials easily. In the conventional SIMS apparatus, the angle of incidence between the sample and the primary ion beam is controlled by adjusting the angle of the sample stage. The sputtering yield increased up to near 70 to 80 degrees of the incident angle then

decreases for larger angles. Figure 1.12 provides an example of the simulated sputtering yield as a function of the angle of incidence for Si bombardment with 30 keV Ga ions. The sputtering yields of Si are increased up to 80 degrees, and at the 80 degrees of incident angle, the sputtering yield is approximately seven times that at normal incidence angle.

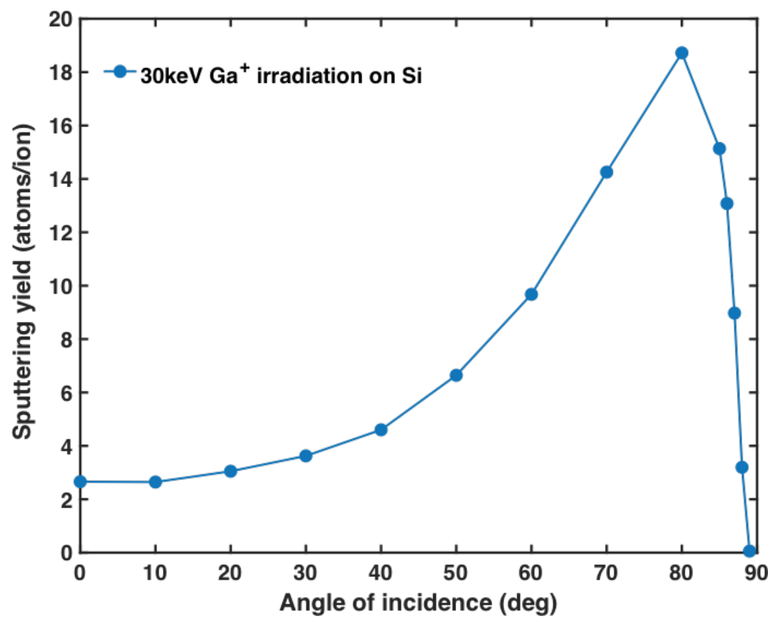


**Fig. 1.12** Sputtering yield as a function of angle of incidence for 30keV $Ga^+$ ions irradiation on Si simulated by SDTrimSP [1.34].

### 1.4.3 Distribution of sputtered particle

Target particles sputtered from the solid surface by ion bombardment are ejected with energy (E) and an emission angles (Ω). The distribution of the parameters is described with sputtering yield as a differential value, $\partial Y/\partial E$ (energy distribution of sputtered particles) and $\partial^2 Y/\partial^2 \Omega$ (angular distribution of sputtered particles). This differential sputtering yields provide the extraction of detailed information about the sputtering process and the collision cascade [1.31, 32].

Investigation of the angular distribution of sputtered particles allows the information on the basic mechanisms of the sputtering, and it is important to obtain direction function

in the momentum distribution. Ejected particles of polycrystalline materials are commonly approximated as a cosine distribution and compared with more or fewer asymmetries. The sputtered particles have larger emission angles for heavy ions and low bombarding energies around the threshold and are emitted from the surface with normal direction for light ions and higher energies.

The angular distribution is also known to shift related to the angle of incidence [1.33]. In the 3D shave-off system, the angular distribution particles are one of the essential factors in the development and design of lens system for achieving high focusing particles.

The energy distribution of sputtered particles generally has a maximum at $E = E_b/2$ ($E_b$ = Surface binding energy). When the energy of the secondary ion is enough larger than surface binding energy, the number of sputtered particles mostly decreases proportionally to $1/E^2$ (E=Secondary ion kinetic energy) [1.35].

## 1.5 Monte Carlo Simulation

Many Monte Carlo computer simulation programs have been developed to describe specific aspects of ions bombardment in ion-solid interactions, and the programs are such as TRIM/SRIM (Transport of Ions in Matter/ Stopping and Range of Ions in Matter) [1.36], MARLOWE [1.37], and TRIM.SP [1.38], TRIDYN [1.39] and SDTrimSP [1.34], etc. The Monte Carlo simulation is limited to particle energies well above the characteristic binding energy of solid (several eV), and it is not elaborate procedures like molecular dynamics (MD) simulation. However the computational speed is considerably larger, it can be easily conducted on a personal computer. The programs were based on the binary-collision approximation (BCA), it has been successful to understand the interaction of fast-moving atoms with solids [1.40]. The simulation of BCA is an assumption that a series of binary collisions can approximate the interaction between energetic ion and target atoms. The process includes implantation, scattering, deposition, the formation of collisional cascade and defect damage, ion mixing, and sputtering of particles from the surface. The two Monte Carlo simulation which used for this study are briefed as follows.

### 1.5.1 SRIM/TRIM

Stopping and Range of Ions in Matter (SRIM) and Transport of Ions in Matter (TRIM) are most widely used programs for a computer simulation of studying of ion-solid interaction due to having convenient user interface and its extensive database. However this program only can treat the implemented rudimental because it was originally designed for the calculation of stopping and ranges only. Therefore, it shows different angular distribution of sputtered particles. Moreover it has drawback which having overestimated sputtering yield for large angle of incidence [1.41, 42].

### 1.5.2 SDTrimSP

Static and Dynamic TRIM sputtering program for Sequential and Parallel computing (SDTrimSP) is a further development version which combined two programs, TRIM.SP (Transport of Ions in Matter Sputtering Program ) and TRIDYN.

The TRIM.SP can calculate the all target atoms trajectories, all moving particles are followed until they leave the target or their kinetic energy below predetermined cutoff energy. And the TRIDYN allows dynamic alteration of the material under irradiation due to the deposition or implantation of incident atoms, due to atomic relocation in the bulk and due to sputter erosion at the surface [1.43]. SDTrimSP program has a variety of input options than SRIM, it has been reported good agreement with angular distribution experimental data [1.42].

## 1.6 Objective of this study

In a various field, a study on new materials and its performance improvement have been continuous, and it is undoubtedly important. In addition to this, it is inevitable to develop analytical techniques that characterize the material and improve the performance of the surface / interface physical conditions and the spatial structure of the distribution, which plays an important role in advanced technologies as well as research on the materials.

As developed new and innovative technologies, the size of the material becomes to be smaller, and the range of its application becomes wide. This is required more accurate analytical techniques which can have high spatial resolution and excellent detection limits, and it corresponds with an advantage of SIMS technique.

Recently, our group proposed a new 3D shave-off SIMS apparatus, the detailed plan for the development is introduced in following sections.

### 1.6.1 Goal of 3D shave-off SIMS

The final goal of this project is the development and instrumentation of the new 3D shave-off method which enables to

(i) Analyze several $\mu m^3$ sized solid sample,
(ii) Short time for analysis (1-2 hours),
(iii) Realize high spatial resolution and high sensitivity
(X, Y-axis; a few nm, Z-axis; 10 nm).

To achieve this goal, we divide the development plan into three steps, and it is summarized in Fig. 1.13.

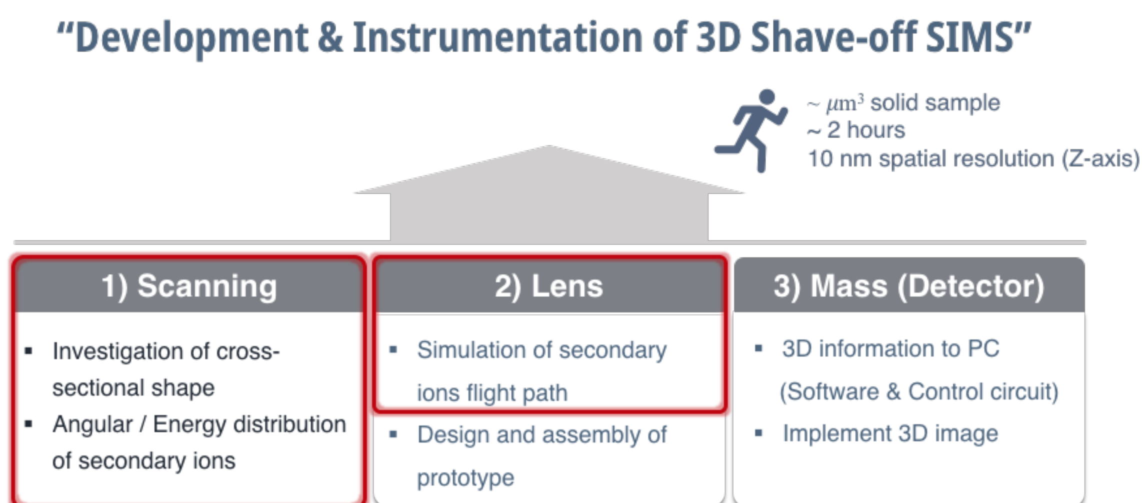


**Fig. 1.13** Three steps for development and instrumentation of 3D shave-off SIMS.

In the scanning step, behaviors of secondary ions are investigated to design the lens system. Because difficulty to change the magnification lens system once made, we need more sufficient simulations of secondary ion trajectories and lens conditions.

In the second step, the prototype of the lens system will be made with a fixed specification. Based on the information of the first step, the secondary ions flight path is simulated with various conditions, and the final optimized conditions of the lens system are determined.

After prototyping and recalculation of the secondary ion flight path, the control circuit and software will be made for getting the 3D position information of secondary ions to PC. And algorithm and control software will be devised to reconstruct the 3D dispersion image from the measurement data. Through the improvement of the device repeatedly, it will be conducted examinations of 3D analysis.

### 1.6.2 Objective of this study

In this thesis, the objective of this study is to obtain information of sputtered particles generated by the primary ion beam. The obtained information will be used for optimization of design and assembly of the prototype magnification lens system (cylindrical lens systems) which is the second steps of the 3D shave-off SIMS. For that reason, I investigated and discussed the parameters of sputtered particles such as the angle of incidence of the primary ion beam, the emission angle of sputtered particles with angular, energy distributions, etc. It could affect the secondary ions trajectories in the 3D shave-off SIMS apparatus. Then through using these results, I simulated whether it can produce the 3D data which have distinguishable depth information in the system.

Firstly, the cross-sectional shape made by the shave-off scanning was observed to measure the angle of incidence. The shape and angle of the cross-sections are an important parameter to determine the emission of the sputtered particles regarding incident angle between the primary ion beam and a sample surface. Through comparing the cross-sectional shapes of three samples with different depth, the effects of the primary ion beam on the samples were investigated in Chapter II.

Secondly, the angle of incidence was investigated as a function of scan speed.
The angle of incidence is one of the factors that specifically affect a sputtering yield. In the conventional SIMS technique, the angle of incidence is easily controlled by changing

an angle of the sample stage. However, the shave-off method is difficult to control the angle of incidence by changing the sample stage because the beam always scans entire of the edge of the sample in the direction of the beam. Therefore, the slope of cross-sections can be finely adjusted by changing the scan speed. In Chapter III, I investigated the angle of incidence and the sputtering yield with three different scan speeds through the cross-sectional shape observation.

In Chapter IV, I investigated the angular and energy distribution of sputtered particles using a simulation program. To optimize and design the lens system, essential parameters of the secondary ion trajectories simulation are emission angle and initial energy of secondary ions. The two parameters can be obtained by Monte-Carlo simulation, but the simulations had no references data with shave-off conditions, high incident energy (over 20 keV $Ga^+$ ions) and a high angle of incidence. Hence, I performed a confirmation work which is a simulation with the condition of existing shave-off experiments and compared the simulation results to the experimental data. Then I simulated the angular and energy distribution on the sputtered tungsten sample for 30 keV irradiation of $Ga^+$ ions beam with shave-off scanning.

Based on the investigation so far, in Chapter V, I simulated the detection position of the sputtered particles by the primary ion beam with shave-off scanning on the 3D shave-off SIMS system. A three-dimensional virtual target which composed of two elements, Ge and Si, was designed and simulated to determine a possibility of 3D shave-off SIMS. For investigation of final detection position on the mass detector, the simulations are conducted with three-steps from sputtering by the FIB to ion flight path in the optical systems of SIMS apparatus.

## 1.7 References


1.1. D. S. Mcphail, *J. Mater. Sci.*, 2006, **41**, 873–903.

1.2. P. Ercius O. Alaidi, M. J. Rames G. Ren, Adv Mater. **27** (38), 2015, 5638-5663.

1.3. M. H. N. Yio, M. J. Mac, H. S. Wong and N. R. Buenfeld, *J. Microsc.*, 2015, **258**, 151–169.

1.4. Y. Ruan, D. Dan, M. Zhang, M. Bai, M. Lei, B. Yao and X. Yang, *Front. Zool.*, 2016, **13**, 1–10.

1.5 C. Sheppard and D. Shotton, "*Confocal Laser Scanning Microscopy*," BIOS Scientific, 1997.

1.6 D. B. Hovis and A. H. Heuer, *J. Microsc.*, 2010, **240**, 173–180.

1.7 T. F. Johnson, J. J. Bailey, F. Iacoviello, J. H. Welsh, P. R. Levison, P. R. Shearing and D. G. Bracewell, *J. Chromatogr. A*, 2018, **1566**, 79–88.

1.8 V. Cnudde, M.N. Boone, *Earth-Science Reviews*, 2013, **123,** 1–17.

1.9 L. Schermelleh, R. Heintzmann and H. Leonhardt, *J. Cell Biol.*, 2010, **190**, 165–175.

1.10 R. G. Wilson, F. A. Stevie and C. W. Magee, "*Secondary ion mass spectrometry: a practical handbook for depth profiling and bulk impurity analysis*," Wiley, 1989.

1.11 S. Carmignato, W. Dewulf and R. Leach, "*Industrial X-Ray Computed Tomography*," Springer International Publishing, 2017.

1.12 Lavery, L. L., Gelb, J., Merkle, A. P. & Steinbach, A. *Microscopy Today*, 2014, **22**, 16–21.

1.13 S. Jung, N. Lee, M. Choi, J. Lee, E. Cho and M. Joo, *Appl. Surf. Sci.*, 2018, **432**, 90–96.

1.14 H. Satoh, *J. Vac. Sci. Technol. B.,* 1988, **6**, 915–918.

1.15 L. A. Giannuzzi and N. C. S. University, "*Introduction to Focused Ion Beams: Instrumentation, Theory, Techniques and Practice*," Springer US, 2004.

1.16 F. M. Company, *J. Mater. Eng. Perform.*, 1998, **7**, 303–311.

1.17 J. C. Vickerman, J. C. Vickerman and I. Gilmore, "*Surface Analysis : the Principal Techniques*," Wiley, 2011, 9–45.

1.18 J. C. Vickerman, J. C. Vickerman and I. Gilmore, "*Surface Analysis : the Principal Technique*," Wiley, 2011, 47–109.

1.19 D. Briggs and M. P. Seah, "*Practical Surface Analysis by Ion and Neutral Spectroscopy*", 2nd Edition, John Wiley & Sons, Chapter 2, 1992, 22–23.

1.20 Denka, Denka L-MION Technical note (Rev. 6), 2016, 1–8.

1.21 R. Herzog, Z. Phys., 1934, **89**, 447–473.

1.22 J. H. Gross, "*Mass Spectrometry: A Textbook*," Springer Berlin Heidelberg, 2011.

1.23 M. Fujii and M. Owari, *Surf. Interface Anal.*, 2013, **45**, 122–125.

1.24 M. Nojima, M. Toi, A. Maekawa, B. Tomiyasu, T. Sakamoto, M. Owari and Y. Nihei, *Appl. Surf. Sci.*, 2004, **231**–**232**, 930–935.

1.25 M. Nojima, B. Tomiyasu, Y. Kanda, M. Owari and Y. Nihei, *Appl. Surf. Sci.*, 2003, **203**–**204**, 194–197.

1.26 D. Shirakura, B. Tomiyasu and M. Owari, *e-Journal Surf. Sci. Nanotechnol.*, 2016, **14**, 179–184.

1.27 M. Fujii, Y. Ishizaki, M. Nojima, M. Owari and Y. Nihei, *Nucl. Instruments Methods Phys. Res. Sect. B Beam Interact. with Mater. Atoms*, 2009, **267**, 660–664.

1.28 T. Sakamoto, K. Shibata, K. Takanashi, M. Owari and Y. Nihei, *e-Journal Surf. Sci. Nanotechnol.*, 2004, **2**, 45–51.

1.29 Y. Takagi, S. Kang, K. Matsumura, T. Azuma, B. Tomiyasu and M. Owari, *e-Journal Surf. Sci. Nanotechnol.*, 2018, **16**, 324–328.

1.30 K. Matusmura, S. Kang, T. Azuma, B. Tomiyasu and M. Owari, Journal of Surface Analysis, [submitted]

1.31 K. Wittmaack, "*Sputtering by Particle Bombardment III*," 1991, **64**. (Chapter 1,2)

1.32 R. Behrisch, "*Sputtering by Particle Bombardment I*," Springer Berlin Heidelberg, 2014, **47**.

1.33 G. K. Wehner and D. Rosenberg, *J. Appl. Phys.*, 1960, **31**, 177–179.

1.34 A. Mutzke, R. Schneider, W. Eckstein, R. Dohmen, Max-Planck-Institute for Plasma-physics, IPP-Report, 2011, **12/8**, 1–70.

1.35 A. Benninghoven, F. G. Rüdenauer and H. W. Werner, "*Secondary Ion Mass Spectrometry: Basic Concepts, Instrumental Aspects, Applications, and Trends*," J. Wiley, 1987.

1.36 www.srim.org.

1.37 M. Robinson and I. Torrens, *Phys. Rev. B*, 1974, **9**, 5008–5024.

1.38 J. P. Biersack and W. Eckstein, *Appl. Phys. A Solids Surfaces*, 1984, **34**, 73–94.

1.39 W. Möller, W. Eckstein and J. P. Biersack, *Comput. Phys. Commun.*, 1988, **51**, 355–368.

1.40 W. Möller and W. Eckstein, *Nucl. Instruments Methods Phys. Res. Sect. B Beam Interact. with Mater. Atoms*, 1984, **2**, 814–818.

1.41 J. F. Ziegler, M. D. Ziegler and J. P. Biersack, *Nucl. Instruments Methods Phys. Res. Sect. B Beam Interact. with Mater. Atoms*, 2010, **268**, 1818–1823.

1.42 H. Hofsäss, K. Zhang and A. Mutzke, *Appl. Surf. Sci.*, 2014, **310**, 134–141.

1.43 W. Möller, TRIDYN-User guide 2017, 1–35.

# CHAPTER II

## ANALYSIS OF CROSS-SECTIONAL SHAPE

In this chapter, the cross-sectional shape after the scanning with the shave-off method was investigated to measure the angle of incidence and verify the relation between the primary ion beam and sample surface. The cross-sectional shape in the shave-off method is an important factor regarding with emission angle of the sputtered atom as well as the angle of incidence of the primary ion beam. Through the observation and simulation of the cross-sectional shape, I discussed the influence of the incident ion beam on the sample and a sputtering process by ion/particle bombardment.

### 2.1 Introduction

In the shave-off method, the cross-sectional shape is an important parameter closely related to the angle of incidence of the beam as well as the sputtering position of secondary ions. Figure 2.1 schematically shows the cross-section of the sample after the raster scan (a) and shave-off scan (b). The cross-sectional shape was defined as a shape of the sample along YZ plane after scanning. The raster scan mode which is usually applied in the conventional SIMS is scanned over the whole of the scan area, and this process is repeated to remove the exposed sample surface. However, in the shave-off method, the ion beam is always scanned over the edge of the sample during the scanning without back to the starting point [2.1]. Therefore, a slope of the cross-sectional shape made by the beam will be related to the angle of incidence between the ion beam and sample surface in the shave-off scan mode (Fig. 2.1(b)).

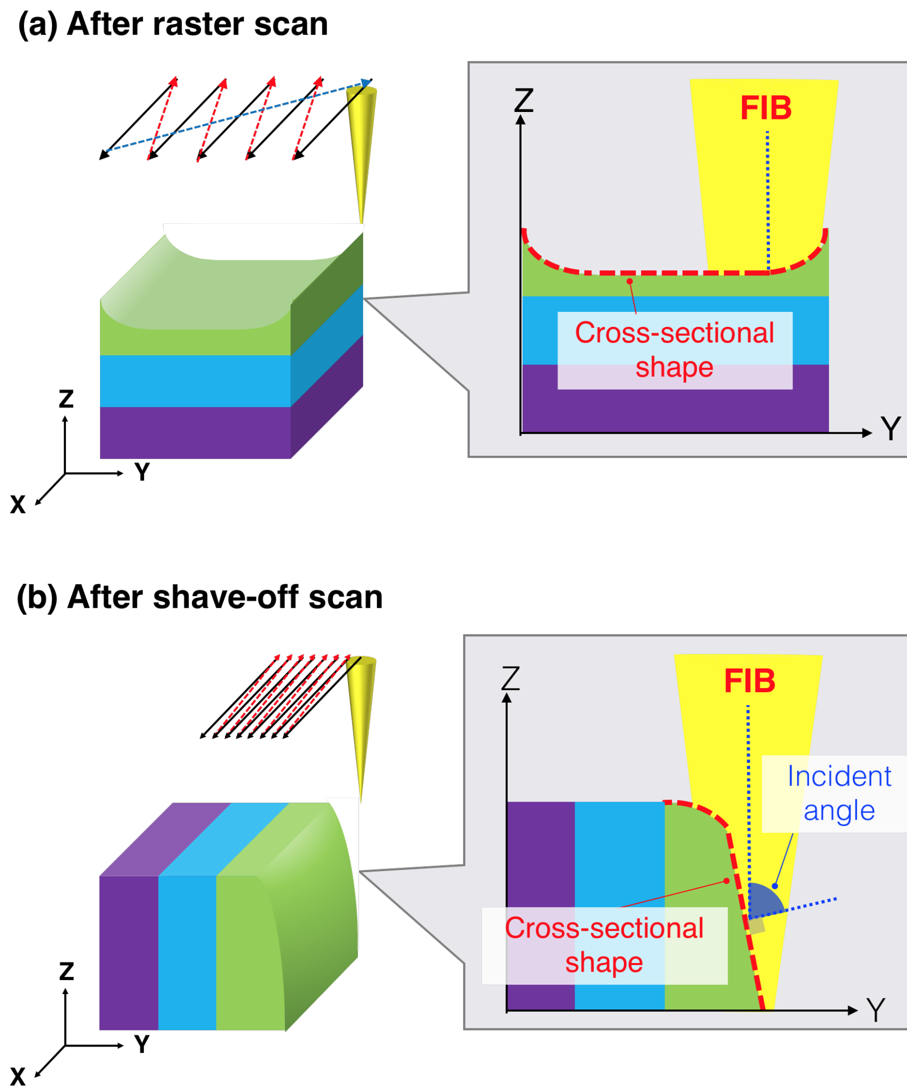


**Fig. 2.1** A schematic of the cross-sectional shape after each scanning mode. (a) Conventional raster scan. (b) Shave-off scan.

For designing and assembly of the magnification lens system in the three-dimensional (3D) shave-off method, we should investigate the angular distribution of sputtered particles.

The emission angles depend on the energy of the primary ion beam and angle of incidence between a sample surface and the ion beam [2.2-5]. Therefore, as a first step for the development of 3D shave-off SIMS, I estimated the incident angle by observing the cross-sectional shape of the sample which was scanned by gallium focused ion beam (Ga-FIB)

with the shave-off method. In addition, I compared the tungsten samples with three different depths which are scanned under the same conditions and discussed the effect of surface erosion factors.

## 2.2 Experiments

All experiments in this part were performed using the focused ion beam scanning electron microscopes (FIB-SEM, SII NanoTechnology Inc, SMI-3050 SE) operating at $4 \times 10^{-6}$ Pa residual gas pressure. A gallium liquid-metal ion source was used to generate an ion beam with 30 keV accelerated energy. The nominal beam size was 40 nm for probe current 260 pA. The cross-sectional shape was measured using transmission electron microscope (TEM, JEOL, JEM-1010, operated at 100 kV).

### 2.2.1 Sample preparation

A tungsten wire (99.95%, Nilaco) with a diameter 40 μm were prepared for the sample using a two-step FIB-milling. Firstly, the tip of tungsten wire was diced into cuboid shape with 3.5 μm (X-axis) and over 6.7 μm (Y-axis). Subsequently, the sample was rotated 90 degrees and cut out the bottom part of the sample for adjusting sample thickness of 30 μm, 20 μm, and 10 μm (Z-axis). Figure 2.2(a) illustrates prepared sample and Figs. 2.2(b) and 2.2(c) show SEM images which are seen the top view and side view of finished prepared sample.

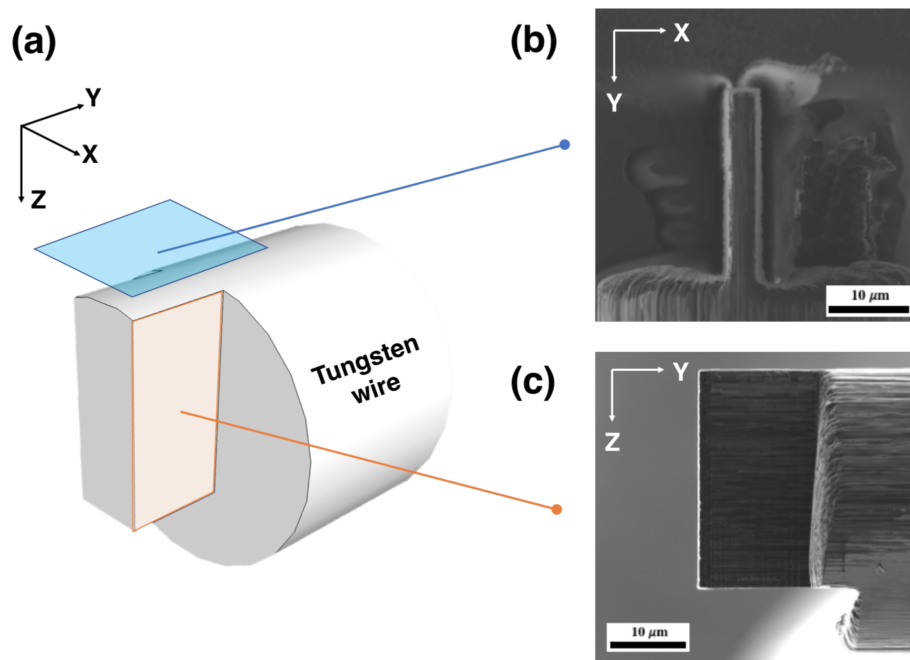


**Fig. 2.2** Prepared tungsten sample by FIB-milling. (a) Isometric view. (b) Top view. (c) Side view. Top view and side view were observed by using FIB-SEM.

### 2.2.2 Scan condition

Figure 2.3 depicts the details of each condition and Table 2.1 provides the experimental scanning condition for raster scan mode and shave-off scan mode.

The raster scan mode was followed a commonly used etch process which is set in the FIB system. Both of X, Y-axis interval length were 50 nm, and dwell time for a pixel was 100 μs. The scanning took a time of 1.34 second for a single frame, and it was repeated 2985 times during the total scanning time (Fig. 2.3(a)).

In the shave-off scanning, the scan speed of the beam was 5.0 μm/s in the horizontal direction (X-axis) and $1.68 \times 10^{-3}$ μm/s in the vertical direction (Y-axis). The scan speed was applied for the interval length of 10 nm for X-axis, and 1.68 nm for Y-axis. The scanning of one single-frame took one second, it repeated 4000 times along the Y-axis of the sample 6.7 μm (Fig. 2.3(b)). For comparison, both of two scanning modes were conducted with the same ion dose. The scanning area for experiments was 5.0 μm (X-axis) × 6.7 μm (Y-axis), the total scanning time was 4000 seconds.

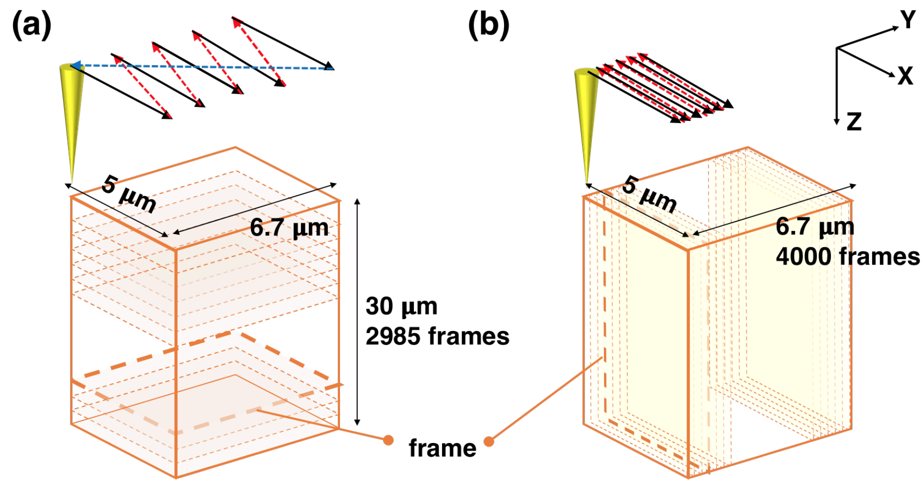


**Fig. 2.3** Procedures of FIB scanning. (a) Raster scan mode. (b) Shave-off scan mode.

**Table 2.1** The conditions of raster scan and shave-off scan mode.

| | | Raster scan | Shave-off scan |
|---|---|---|---|
| X interval length | nm | 50 | 10 |
| Y interval length | nm | 50 | 1.68 |
| Dwell time | μs | 100 | 2000 |
| Horizontal speed (X) | μm/s | 500 | 5 |
| Vertical speed (Y) | μm/s | 5 | $1.68\times10^{-3}$ |
| Single-frame sweep time | s | 1.34 | 1 |
| Number of single frame | times | 2985 | 4000 |
| Total scanning time | s | $4 \times 10^{3}$ | |
| Scan area (X × Y) | $\mu m^2$ | 5.0 × 6.7 | |

## 2.3 Results and discussion

### 2.3.1 Analysis of cross-sectional shape

Figure 2.4 shows TEM images from before and after scanning with raster mode (a), and shave-off mode (b). In the figures, a gray part is the cross-sectional shape of the sample before scanning, the black in the figures is cross-sectional shape after scanning. The experiment was conducted in the same beam condition, the same scan area (5.0 × 6.7 μm$^2$) and scanning time (4000 s) with tungsten sample (W, depth; 30 μm). However, the profiles of raster scan mode (Fig. 2.4(a)) and shave scan mode (Fig. 2.4(b)) were clearly different.

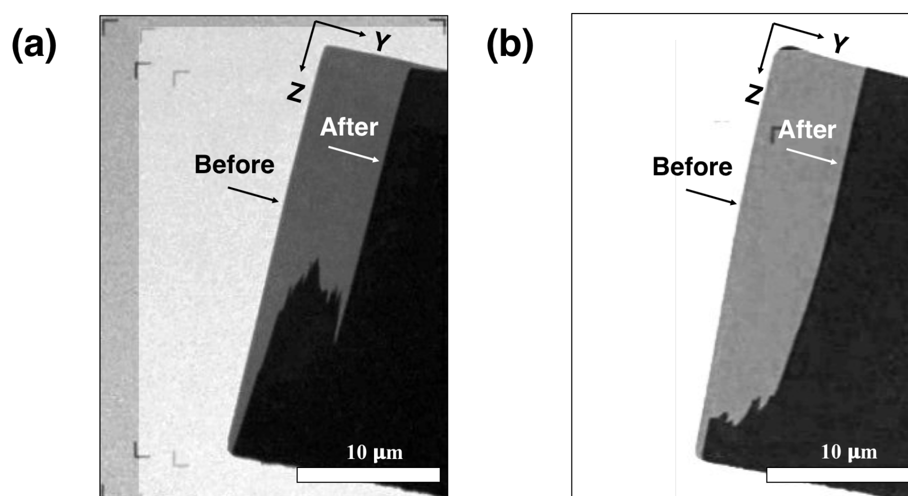


**Fig. 2.4** A composite TEM image of before and after scanning. (a) Raster scan mode. (b) Shave-off scan mode.

To investigate the influence of the ion beam on the sample, three tungsten samples with different depth (30 μm, 20 μm, and 10 μm) were scanned under the same FIB shave-off conditions and the cross-sectional shapes of the samples were compared. Figure 2.5 shows SEM images of the samples seen in the top view before and after the shave-off scanning. The sample having a depth of 30 μm was not completely etched (Fig. 2.5(a)),

the 20 μm depth sample has remained about 2 μm (Fig. 2.5(b)). However, the sample with a depth of 10 μm was wholly removed off (Fig. 2.5(c)) by the primary ion beam.

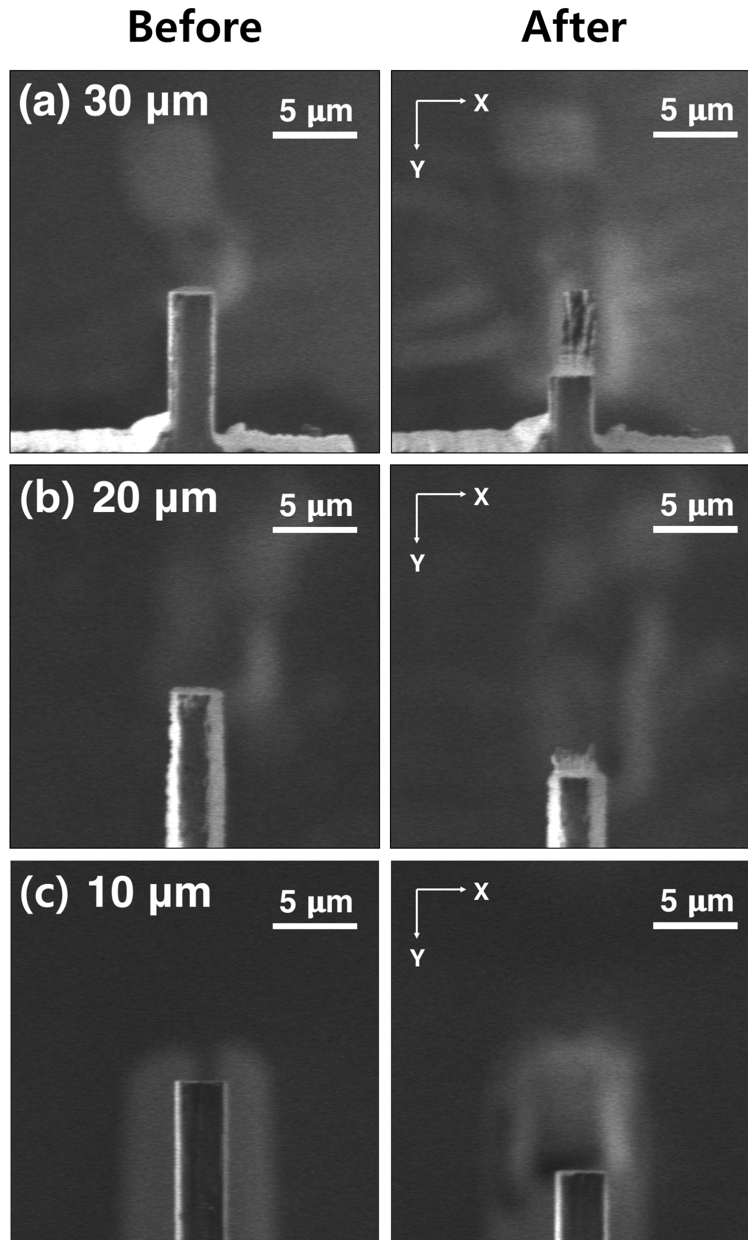


**Fig. 2.5** Top view of the SEM sample images before (Left) and after (Right) scanning. Sample depth is (a) 30 μm, (b) 20 μm, and (c) 10 μm.

Figure 2.6 presents the cross sections (YZ plane) of the three samples. The cross-sectional shapes were observed by using TEM. For a more accurate comparison, the images were digitized to coordinates system. The composite graph of each coordinated cross-sectional shape is shown in Fig. 2.7.

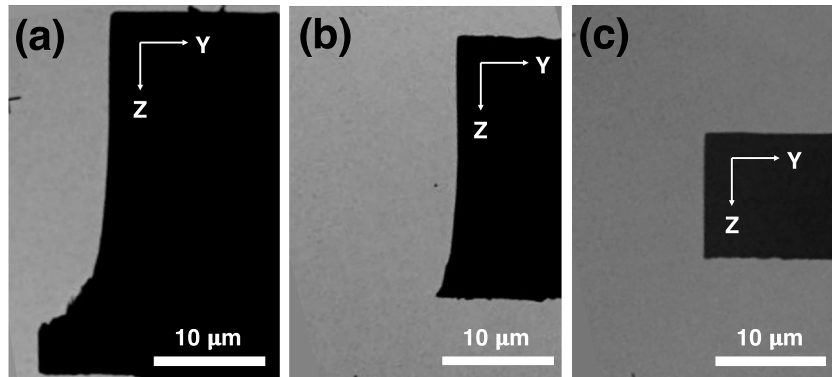


**Fig. 2.6** Transmission electron microscopy (TEM) images of cross-section view of the tungsten samples after shave-off scanning: sample depth (a) 30 μm, (b) 20 μm, and (c) 10 μm.

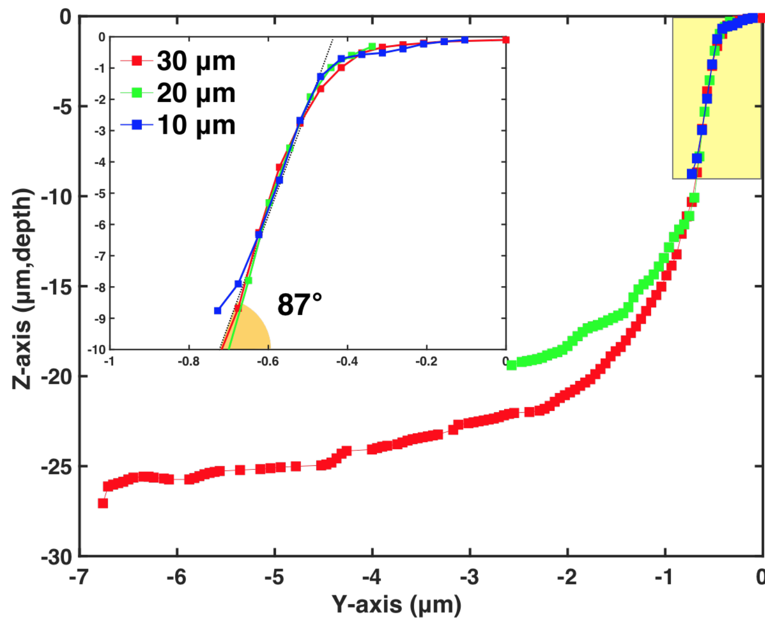


**Fig. 2.7** Digitized coordinates of the cross-sectional shape of TEM images in Fig. 2.6. The inset figure shows a magnification of highlighted part.

The cross-sectional shapes of the three different samples were considerably similar to each other. The part from the surface (0 μm) to 13 μm on the Z-axis shows a similar slope, whereas a part of lower than 13 μm has a different shape even though scanned under same shave-off condition. From this observation of the cross-sectional shape, the unusual shape at the lower part of the sample could be expected to be the results from mixed three factors by; (1) primary beam ions ($Ga^+$), (2) re-sputtered $Ga^+$ ions from the 0 μm to 13 μm of Z-axis, and (3) sputtered neutral tungsten atoms from the sample.

Additionally, the angle of incidence can be measured from the three cross-sectional shapes. Because the lower part of the sample was expected that affected by not only the primary ion beam also others, the angle of incidence was determined at the part showing the similar slope. The average angle between the primary ion beam and the cross-sectional sample surface of 87° is calculated (Fig. 2.7). This value will be used the angle of incidence for $Ga^+$ ion irradiation of the tungsten sample with the shave-off scanning.

### 2.3.2 Simulation of particle bombardment

The particle bombardment was simulated by using SDTrimSP program to verify the above expected three factors and effect of the primary ion beam to the sample. To compare the particle bombardment as a function of the angle of incidence of the primary ion beam, I performed that 100 gallium ions incident to the target surface with a normal angle (0 degree) and 87 degrees, respectively. Figure 2.8 presents the results of the simulation for 30 keV $Ga^+$ ion irradiation on the tungsten. In case of normal incident angle, 85 of 100 $Ga^+$ incidence ions are trapped into the sample, and 15 of the rest particles are scattered. 502 particles of the tungsten are sputtered by this bombardment (Fig. 2.8(a)). However, when the gallium ions incident with 87 degrees, the only 5 of $Ga^+$ ions are implanted into the tungsten. The rest 95 of Ga atoms are backscattered in a single collision, and 248 of tungsten particles are sputtered by Ga ions, as shown in Fig. 2.8(b). The angle of incidence 0 degree which is the normal condition of raster scan has a higher sputtering yield (5.02 = 502/100) than 87 of incidence angle (2.48 = 248/100), but it also has higher the implanted particles. The implanted Ga particles generate the mixing effects which damage the sample. It could be interpreted as the previous result that the shave-off method has a lower mixing effect than the raster scan mode [2.6, 7].

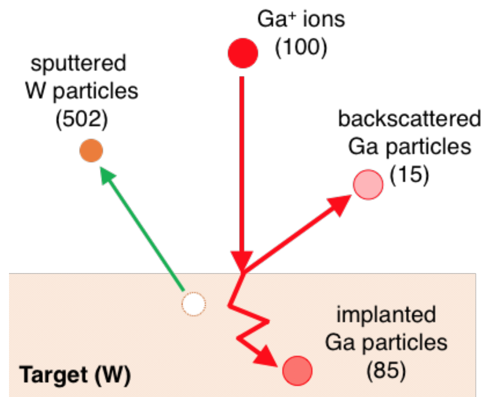


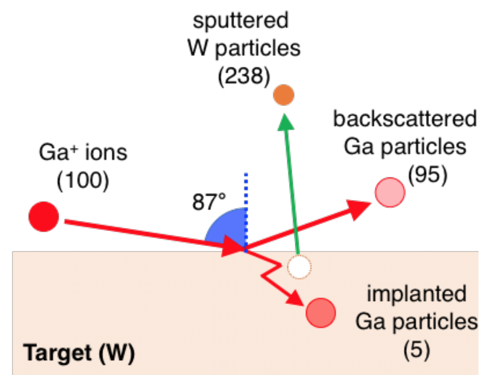


**Fig. 2.8** Ion bombardment at each condition simulated using SDTrimSP. (a) Raster scan (angle of incidence = 0°) mode. (b) Shave-off scan (angle of incidence = 87°) mode.

Figure 2.9 provides trajectories of the 95 of scattered particles and the 5 of implanted Ga particles (blue) with recoils tungsten particles displaced in a collision cascade (red) for the ion irradiation at $\theta = 87°$. The surface of the tungsten is located at depth zero, and the gallium ions affected the tungsten sample maximum depths of 12 nm at this condition.

(a)

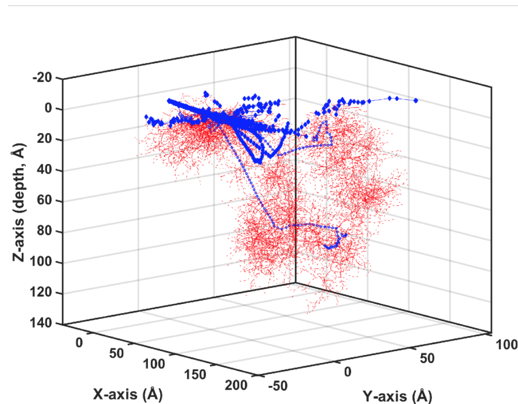


(b)

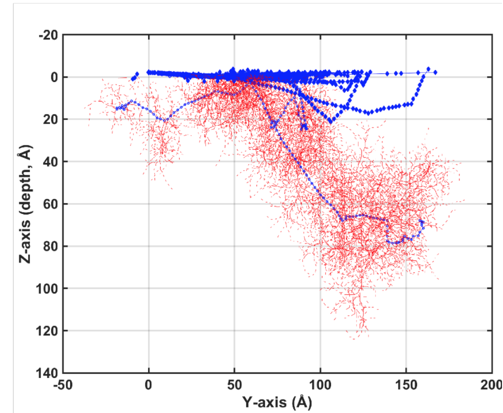


**Fig. 2.9** (a) Trajectories of a 30 keV $Ga^+$ ions of 100 penetrating a tungsten sample at angle of incidence $\theta = 87°$. The color indicates the incident Ga particles (blue) and the recoiled W particles (red). (b) In a view of the YZ plane.

Figure 2.10 presents only the trajectories of 95 scattered Ga particles and the angular distribution of the scattered particles. The Ga particles were scattered in a direction with 87 degrees which is the same as an angle of incidence. Figure 2.11 shows the emission angle of 238 sputtered W particles as a function of energy and number of particles.

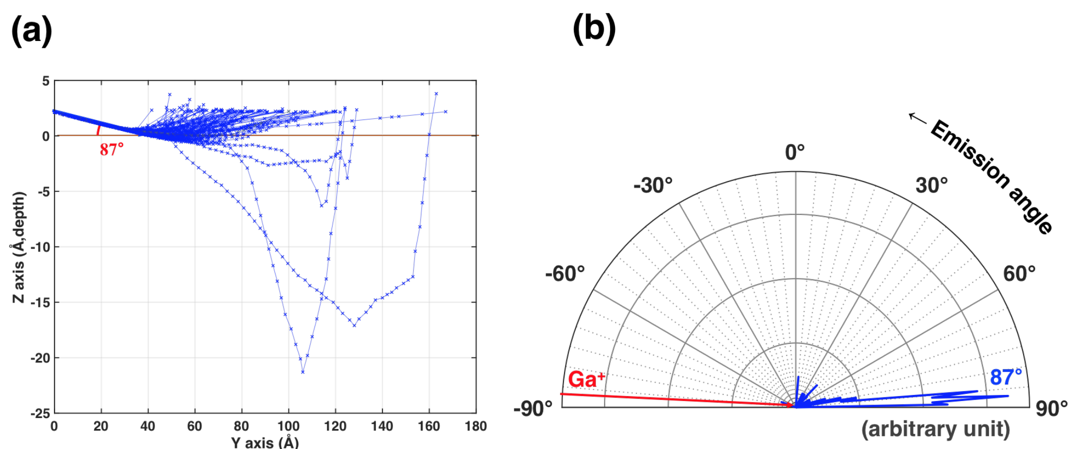


**Fig. 2.10** (a) Trajectory of scattered Ga particles. (b) Angular distribution of 95 scattered Ga particles.

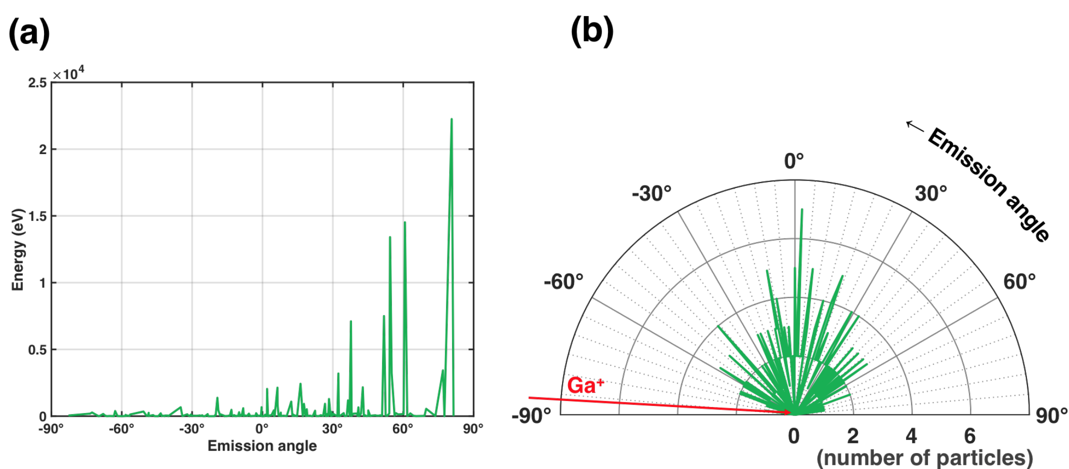


**Fig. 2.11** (a) Energies of 238 sputtered particles as a function of emission angle. (b) Angular distribution of the sputtered W particles.

In Fig. 2.11(a) shows a tendency that the particles having high energy had high emission angle. However, a large number of the particles showed a perpendicular direction (0°) from the surface (Fig. 2.11(b)). It is considered that most of the sputtered particles are emitted in the perpendicular direction in the sample with small energy, and some particles which having high energy are emitted in the horizontal direction.

From this simulation result, I could verify that the two cases of particles having high emission angles affected the bottom part of the sample, which is the result of the difference in the cross-sectional shape. However, in the practical experiment, we do not need to consider the effects on the sample. In this study, I used sample depths of 20 μm and 30 μm for investigation of the particles generated by the primary ion beam, but we usually use samples of less than 10 μm in depth, In addition, the shave-off method always removes the edge of the sample completely, the particles with high emission angles will be directed downward without affecting the sample.

From this investigation, I could discuss that the high-energy particles such as neutral atoms among the sputtered particles or scattered particles are emitted in the direction of downward, that low-energy particles such as ions are emitted in the direction of perpendicular to the sample surface (Fig. 2.12). It is expected that we can obtain the ions effectively except for high-energy particles.

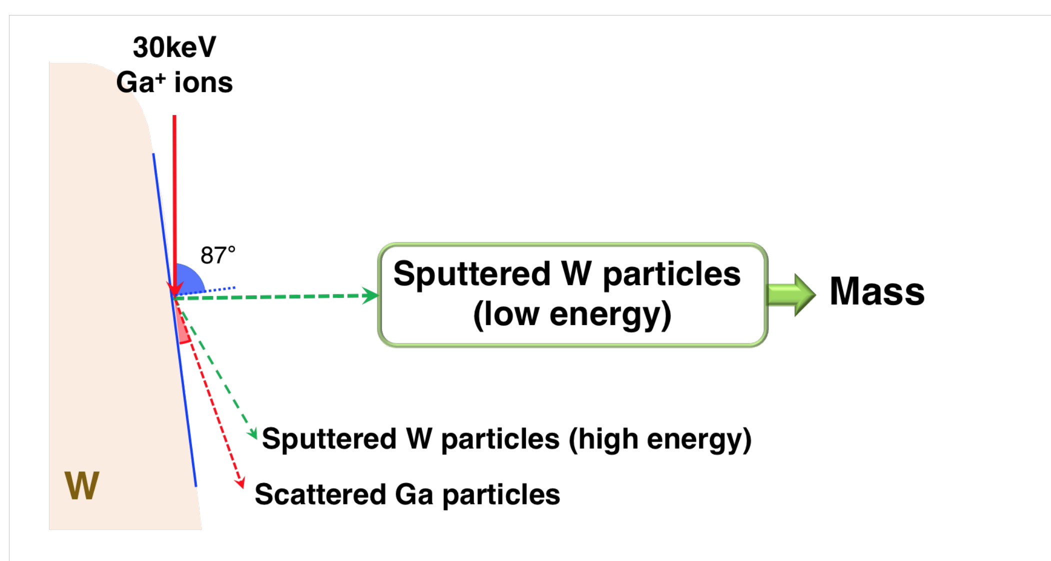


**Fig. 2.12** Schematic representation of the emission angle of the sputtered and scattered particles.

## 2.4 Conclusion

In this chapter, I observed the cross-sectional shape after shave-off scanning. In order to verify the effect of the primary ion beam on the target sample and sputtered particles, the cross-sectional shape of samples with three different depth (30, 20 and 10 μm) were compared under the same beam condition. Three cross-sections have a similar slope at up to certain depths (10 μm) of the sample, the angle of incidence was measured 87 degrees from a trend line of the slope. The rest of the lower part showed a differences slope. It was expected to be formed by other factors, not only the primary ion beam.

The other factors were investigated through the simulation of particle bombardment using SDTrimSP simulation program. For the 30 keV 100 of $Ga^+$ ions irradiation on tungsten with 87 degrees of incident angle, the only 5 of Ga ions were trapped in the tungsten. Most of Ga ions (95 particles) were scattered out with 87° of emission angle which same as the angle of incidence. 248 of tungsten particles were sputtered away from the sample by ion bombardment, and the sputtered particles were observed that the particles with higher energy have a higher emission angle.

It can be concluded that the scattered particles of the primary ion beams and the sputtered particle having high energy emitted with the directions of downwards, it affected the remaining lower part of the sample.

This novel approach for the analysis of shave-off cross-sectional shape will have helpful functions for providing information about the relationship between the primary ion beam and the sample surface. The observed 87° from the cross-sectional shape will provide as a base incident angle parameter to a process of 3D shave-off SIMS development.

## 2.5 References


2.1 H. Satoh, M. Owari and Y. Nihei, *J. Vac. Sci. Technol. B.,* 1988, **6**, 915–918.

2.2 K. Wittmaack, "*Sputtering by Particle Bombardment III,*" 1991, vol. 64, Springer Berlin Heidelberg, 17–59.

2.3 A. Benninghoven, F. G. Rüdenauer and H. W. Werner, "*Secondary Ion Mass Spectrometry: Basic Concepts, Instrumental Aspects, Applications, and Trends,*" 1987, J. Wiley, 260–276.

2.4 T. Okutani, M. Shikata, S. Ichimura and R. Shimizu, *J. Appl. Phys*., 1980, **51**, 2884–2887.

2.5 C. Verdeil, T. Wirtz, H. N. Migeon and H. Scherrer, *Appl. Surf. Sci*., 2008, **255**, 870–873.

2.6 M. Karasawa, M. Fujii, M. Morita, S. Ishimura, N. Mayama, H. Uchida, Y. Kawamura, K. M. Itoh and M. Owari, *Surf. Interface Anal.,* 2014, **46**, 1200–1203.

2.7 M. Fujii and M. Owari, *e-Journal Surf. Sci. Nanotechnol.*, 2012, **10**, 463–466.

# CHAPTER III

## INFLUENCE OF THE SHAVE-OFF SCAN SPEED ON THE CROSS-SECTIONAL SHAPE

In this chapter, I measured the angle of incidence as a function of scan speed by observing the cross-sectional shape. The relation of between angle of incidence and the cross-sectional shape in the shave-off method was mentioned in previously CHAPTER II. The cross-sectional shape depends on the scan speed, and moreover, its influence to the sputtering yield. In order to verify the angle of incidence dependence on the scan speed, the cross-sectional shape was observed and compared with three different scan speed. The sputtering yield could be calculated by the angle of incidence.

### 3.1 Introduction

In a sputtering process, the angle of incidence of a primary ion beam is an essential parameter to effect sputtering yield, secondary ion yield, depth resolution and angular, energy distribution [3.1]. It also has an important function on the development of the 3D shave-off SIMS because the emission angle that determines the secondary ion transport trajectory in the SIMS is depended on the angle of incidence. There are two major parameters of the secondary ions to affect the position on the mass detector of the secondary ions, one is the emission angle, and the other is the energy of secondary ions [3.2]. These two functions determine the trajectories in the electric fields inside the SIMS apparatus. The energy of secondary ions is hard to control, but the angle of incidence can easily be changed. Usually, in the conventional secondary ion mass spectrometry (SIMS) or focused ion beam (FIB) system, the angle of incidence was easily controlled by changing the angle of the sample stage [3.3]. However, in the shave-off method, the angle of incidence is hard to adjust by controlling the sample stage. Because the primary beam always scans an edge of the sample, it has a high incident angle in the direction of incident beam regardless of the stage angle.

As reported by Santamore et al. [3.4], the reason for changed sputtering yield as a function of FIB scan speed was explained with the angle of incidence between the ion beam and sample surface. In the raster scan, they achieved results that the slower the scan, the larger the angle, and the larger the angle, the larger the sputtering yield.

In this chapter, I investigated the relationship between scan speed of the FIB and angle of incidence under the shave-off condition. It can be a way of changing the angle of incidence in the shave-off method. From the observation of the cross-sectional shape of the sample, the angle of incidence was measured, and I could calculate the sputtering yield from the result.

### 3.2 Experiments

The scanning the sample and observation of cross-sectional shape were conducted using the focused ion beam scanning electron microscopes (FIB-SEM, SII NanoTechnology Inc, SMI-3050 SE) operating at $4 \times 10^{-6}$ Pa residual gas pressure. Gallium primary ion beam generated by 30 keV accelerated energy with a probe current 260 pA was irradiated on a tungsten sample. The preparing of the sample and the condition of the primary beam are the same as the experiment of CHAPTER II, the depth of the samples was 30 μm.

In order to investigate the angle of incidence of sputtered particles and the sputtering yield change as a function of scan speed, the cross-sectional shapes were compared under three different scan speeds. In the digital FIB scanning systems, the scan speed of the primary ion beam can be changed by adjusting two factors, dwell time and interval length. When the scanning of the FIB, the primary ion beam pauses on a pixel point for a certain time and then moves to the next pixel point. The time to stay at the pixel is called dwell time, and the distance between two adjacent pixels is defined as the interval length [3.5].

In this experiment, the scan speeds were changed by Y-axis interval length of the primary ion beam. Table 1 is summarized the shave-off conditions of three different scan speed. Each condition had the Y interval lengths as 0.84, 1.68 and 3.35 nm, the dwell time and the X-axis interval length were constant as 2000 μs and 10 nm respectively. The scan time and scan area at each condition were adjusted to have same beam ion dose $2.32 \times 10^{9}$ ions/μm$^2$. Figure 3.1 schematically shows the scanning conditions of the three different scan speed.

The experiment was conducted three times at each scan speed, and the shave-off method gave comparable and repeatable results. The angle of incidence was measured with the trace of the beam as 90°. The traces made by the FIB were left on the sample. The error factor of the angle from the width of the mark is about 0.007°.

**Table 3.1** The conditions of shave-off scan mode

| | | standard | 2 times faster | 2 times slower |
|---|---|---|---|---|
| X interval length | nm | 10 | 10 | 10 |
| Y interval length | nm | 1.68 | 3.35 | 0.84 |
| Dwell time | µs | 2000 | 2000 | 2000 |
| Horizontal speed (X) | µm/s | 5 | 5 | 5 |
| Vertical speed (Y) | µm/s | $1.68 \times 10^{-3}$ | $3.35 \times 10^{-3}$ | $0.84 \times 10^{-3}$ |
| Total scanning time | s | $4 \times 10^3$ | $2 \times 10^3$ | $4 \times 10^3$ |
| Scan area (X × Y) | $\mu m^2$ | 5.0 × 6.7 | 5.0 × 6.7 | 5.0 × 3.35 |
| Ion flux | ions/$\mu m^2$ | | $2.32 \times 10^9$ | |

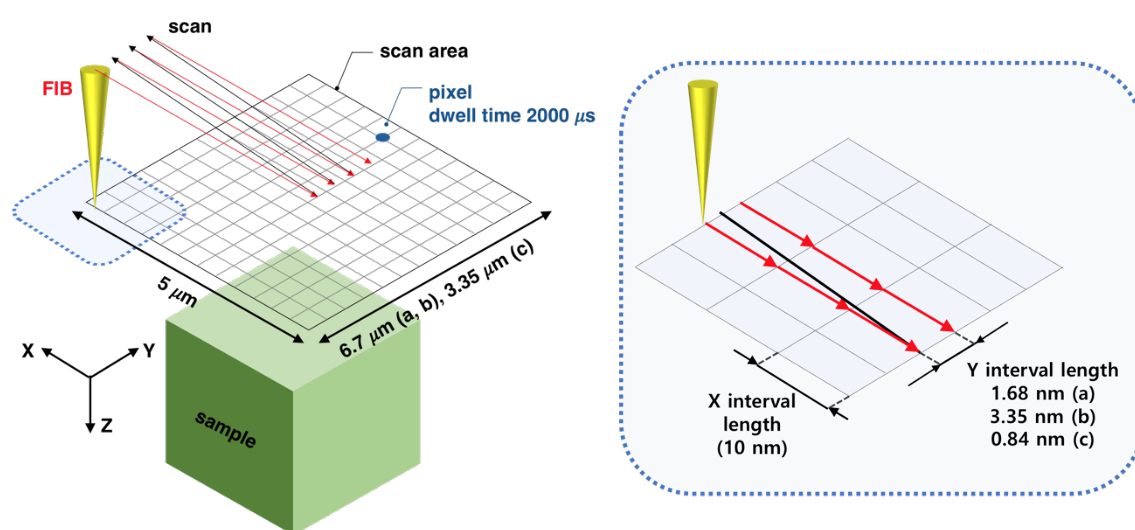


**Fig 3.1** Schematic representation of experimental scan conditions. (a) standard, (b) 2 times faster, and (c) 2 times slower.

## 3.3 Results and discussion

### 3.3.1 Influence of the shave-off scan speed on cross-sectional shape

The cross-sectional shapes according to scan speed were examined by using SEM. Figure 3.4 shows the SEM images of cross-sectional shapes after shave-off scan with three different scan speed. The results showed the distinctly different shape and the depth of the sample removed by the beam. For scan speed of standard (a) and two times faster (b), the samples remained 4 μm and 14 μm of the depth, respectively, after scanning. In contrast, the sample with the scan speed of two times slower (c) was entirely removed the 30 μm of sample depth by the primary ion beam. It can explain that the faster scan speed which has large interval length removes fewer atoms per unit area than slower scan speed, and the sample is shallow eroded by once FIB sweep due to the lower number of scan per the same area [3.4, 3.6]. By comparing the results, we could see a change between scan speed and sputtered atoms under the shave-off scan mode. The results indicated that when the scan speed was decreased, the cross-sectional shape of the sample shows more deep and steep shape, and when the scan speed was increased, the slope of cross-sectional shape shows decreased slope.

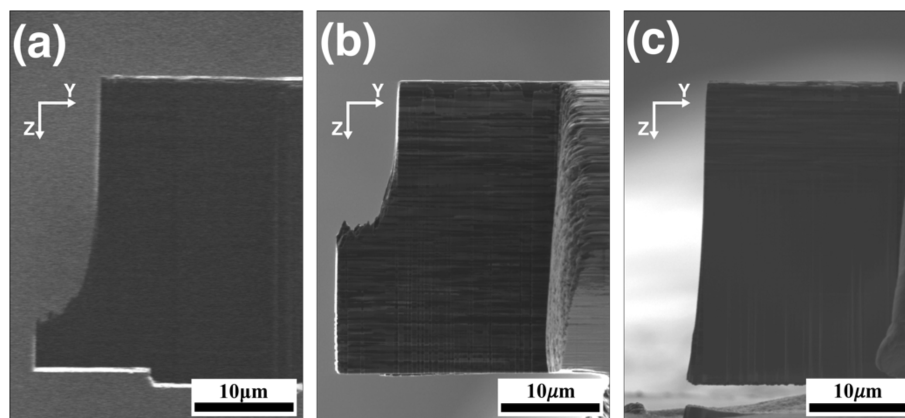


**Fig. 3.2** Scanning electron microscopes (SEM) images of sample profile after shave-off scanning with three different scan speed (a) standard, (b) 2 times faster, (c) 2 times slower.

For comparison, the cross-sectional SEM images were digitized graphically using a program made by our laboratory member based on the Visual Basic software. In previous CHAPTER II, the bottom part of the cross-sectional shape was affected by the primary ion beam and other factors. Therefore, only part of the 10 μm depth from the sample surface (0 μm) was converted to a graph of the cross-sectional shape. The graphs of the cross-sectional shape are shown in Fig. 3.3(a). In the graph which shows the surface position of the sample as 0 μm of the Z-axis, each final scan position differed due to the differences in Y interval length. Thus, the graphs were compared at the highest slope positions of each. The positions of each highest slope were measured from the peak of a differential of the cross-section graphs in Fig.3.3(a) as shown in Fig. 3.3(b). The dash lines in Fig. 3.3(a) present the cross sections of the tangent line at the peak point. It revealed that the slower scan speed increased the slope of the cross sections. The slope is referred to the angle of incidence between the primary ion beam and the sample surface, and its details will be discussed in the next section with sputtering yield.

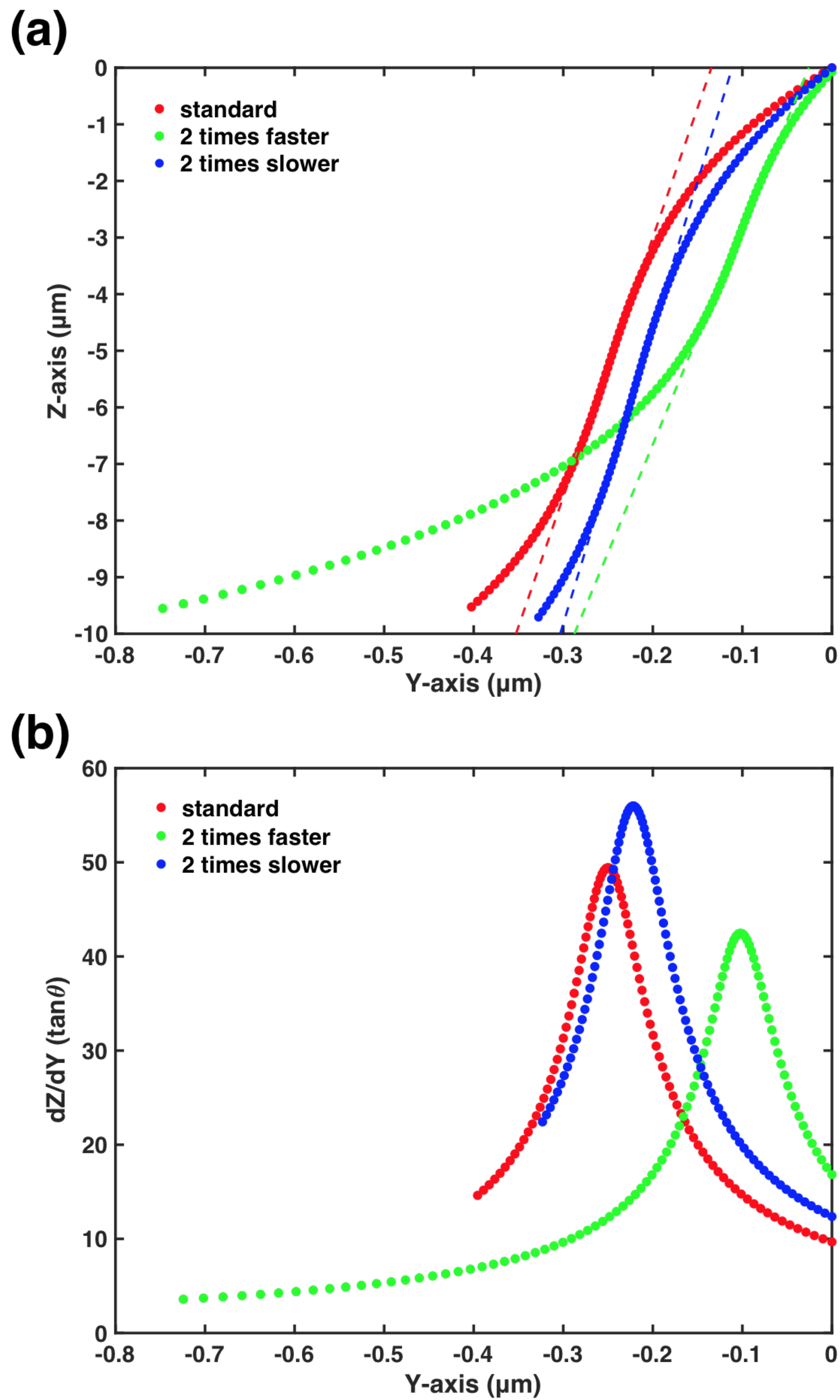


**Fig. 3.3** (a) The cross-sectional shapes were digitized from the SEM images (only a part from the sample surface to 10 μm of Z-axis). (b) Differential graph of the cross-sectional shape from (a). The dash line in Fig 3.3(a) is a tangent line at each peak point in Fig. 3.3(b).

### 3.3.2 Sputtering yield

The erosion depth and sputtering yield depend on the scan speed [3.4, 7-9]. From the differences of erosion in the cross-sectional shape, it could be inferred that the sputtering yield was changed as a function of scan speed. I could calculate the sputtering yield using a surface erosion calculation. The shave-off method always keeps the focused ion beam at one edge of the sample during the scanning, and the cross section can be maintained its shape after each horizontal sweep without re-deposition. Thus the calculation of sputtering yield had not taken into consideration the re-deposition and reflection of sputtered atoms. The relation of ion flux and scan speed is given by the Eq. (1) [3.4, 10, 11]

$$\frac{J(x)}{NV_x} = \frac{\tan\theta}{S(\theta)} \tag{1}$$

where, $J$ is the ion flux (ions/μm$^2$/s), $V$ is the beam scan speed (μm/s), $N$ is the atomic density of the target (atoms/μm$^3$), and $S(\theta)$ is the sputtering yield (atoms/ion). The ion flux from the primary ion beam is $2.32 \times 10^9$ ions/μm$^2$/s, and the atomic density of W is $6.3 \times 10^{10}$ atoms/μm$^3$.

The angle of incidence ($\theta$) was measured at the highest angle of slope in the cross-sectional shape. Figure 3.4 presents the angles between the primary ion beam and cross-sectional shape, the Y-axis value at the highest peaks were 0.25 μm for standard, 0.10 μm for 2 times faster speed, and 0.22 μm for 2 times slower speed, respectively.

As mentioned above, the angle of incidence was associated with the cross-sectional shape using the shave-off method. The sputtering yield was calculated from Eq. (1) using the measured angle of incidence. Table 2 summarized the sputtering yields and the angles of incidence. Although it is a small difference, the angle of incidence decreased with faster scan speed. Figure 3.5 represents the relationship between these three factors.

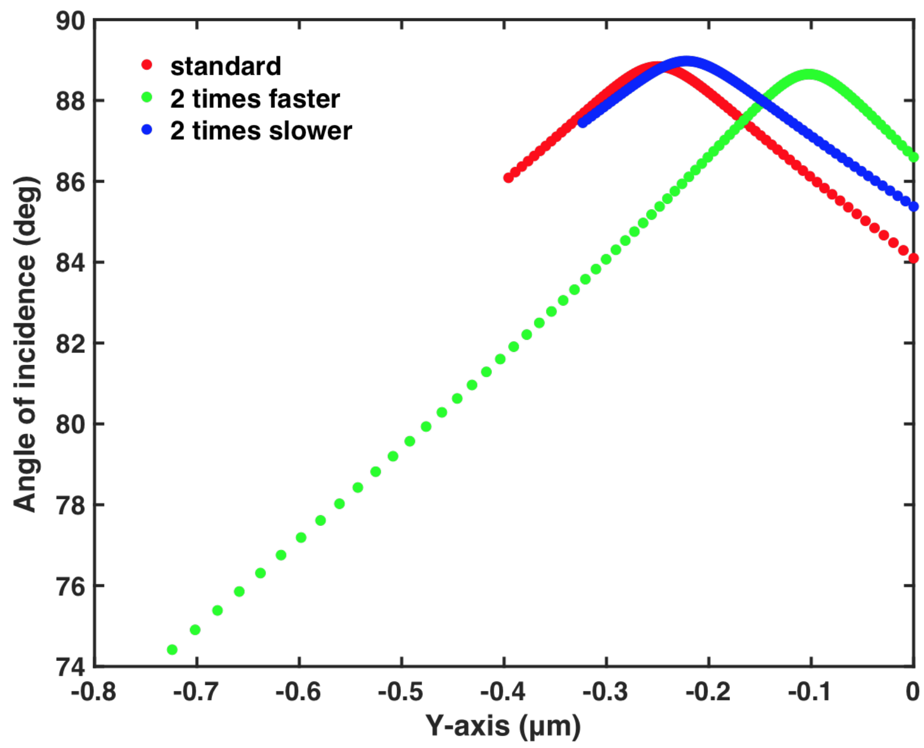


**Fig. 3.4** Angle of incidence between primary ion beam and cross sections on the sample.

**Table 3.2** The angle of incidence at steepest position on the cross-sectional shape and calculated sputtering yield as function of scan speed.

| | | standard | 2 times faster | 2 times slower |
|---|---|---|---|---|
| Vertical speed ($V$) | μm/s | $1.68 \times 10^{-3}$ | $3.35 \times 10^{-3}$ | $0.84 \times 10^{-3}$ |
| Angle of incidence ($\theta$) | ° | 88.84 | 88.65 | 88.98 |
| Sputtering Yield [$S(\theta)$] | atoms/ion | 2.27 | 3.87 | 1.28 |
| | Ratio | 1 | 1.71 | 0.57 |

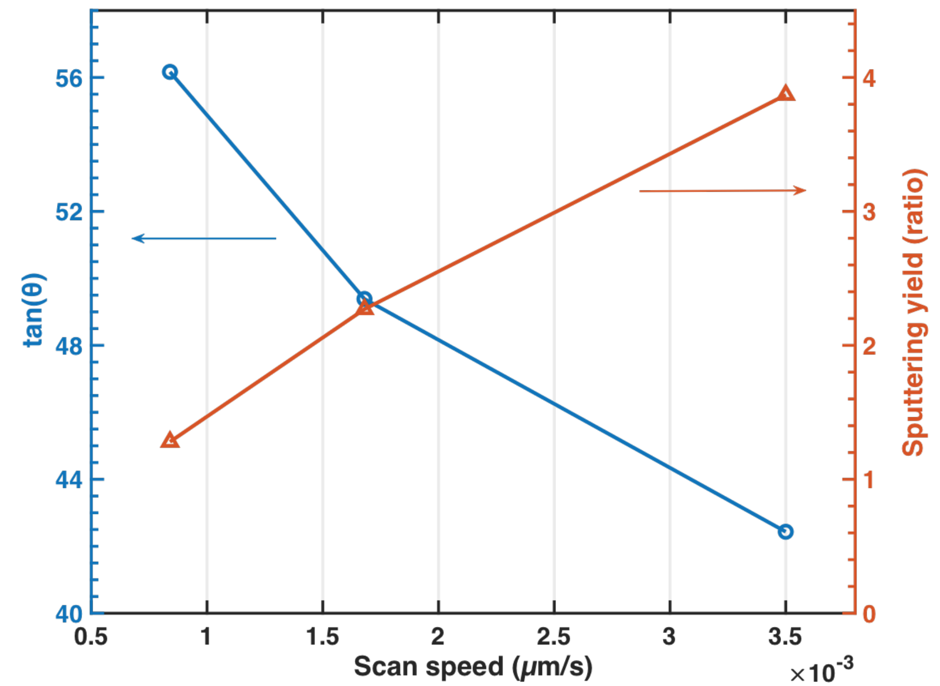


**Fig. 3.5** Angle of incidence (blue) and sputtering yield (orange) as a function of scan speed.

For the raster scan method, a slower scan speed has a larger the angle of incidence and a larger the angle leads to increasing sputtering yield [3.4]. However, this study about the shave-off method showed opposite results that the sputtering yield decreases with decreasing scan speed. If the ratio of the sputtering yield of the standard condition was set to 1, the sputtering yield at a two times faster scan speed was about 1.71 times higher, and the two times slower scan speed had about 0.5 times the lower sputtering yield. This contrary result can be explained by the unusual incident angle of the shave-off scan mode compared with the conventional raster scan mode.

The shave-off scan mode always had an incident angle above 75° as shown in Fig. 3.4. When I simulated the sputtering yield as a function of incident angle for 30keV Ga ion irradiation of W using the SRIM 2013 [3.12] and SDTrimSP V5.7 [3.13], the results are shown in Fig. 3.6. The sputtering yield increases with increasing incident angles until 70° (SDTrimSP) and 75° (SRIM) for the two types of simulation, respectively. At the larger than these angles, the sputtering yield decreases sharply. It was due to the increasing the reflection of ions [3.9]. It also was the corresponding results in previous chapter 1 that most of the incidence ions were scattered at the high angle of incidence.

In the conventional raster scan method of the FIB system, the scanning is usually operated with an incident angle under 60°. Thus the angle between the ion beam and the surface is generally increased with decreasing scan speed, and the larger angle has the larger sputtering yield. However, for the shave-off method, the slope of the sidewall has an angle of more than over the 75° as shown in Fig. 3.4, and it becomes the incident angle of the primary ion beam. Thus, a slower the scan speed has a smaller the incident angle with decreasing sputtering yield. This result was expected to give the relation between the angle of incidence, scan speed, and sputtering yield when using the shave-off method with Ga-FIB.

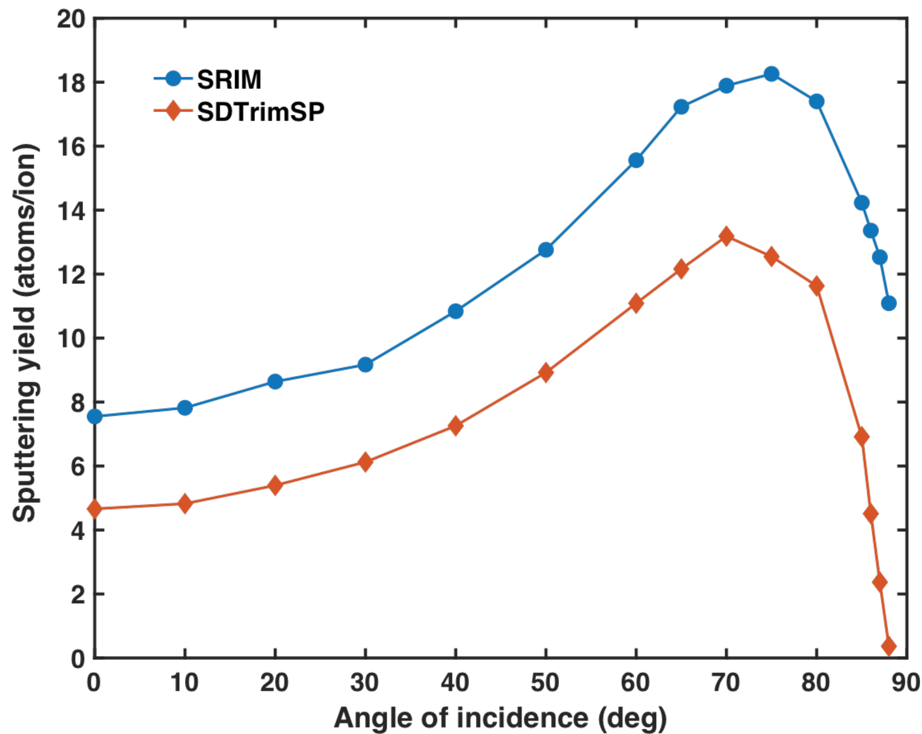


**Fig. 3.6** Sputtering yields as a function of the angle of incidence for 30 keV $Ga^+$ ions irradiation of W. The values were obtained from the simulation of SRIM (blue) and SDTrimSP (orange).

### 3.3.3 Assumption of Beam profile

The erosion rate was shown to be affected by ion flux of incidence beam, sputtering yield, and the atomic density of the sample in Eq. (1). Here, if the sputtering yield and the atomic density of the sample have constant value during the scanning, the erosion rate is only relative by the ion flux of the beam. Therefore, I could consider that the cross-sectional shape is a sum of the ion flux during the scanning, and a profile of the primary ion beam could be expected from the cross sections. The beam profile of the FIB used in this experiment was estimated from the derivative of the cross-sectional shape as shown in Fig. 3.3(b).

Figure 3.7 (a) is that each peak of derivative graphs in Fig. 3.3(b) was moved as 0 μm to compare. The height difference between the standard and the two times faster scan speeds was equal to the difference between the standard and the two times slower scan speeds, it indicates that the sputtering yield changes according to the scan speed. If the

sputtering yields are the same at each scan speed, the peak of the two times faster scan speed should have been twice as high as the standard scan speed, and the height of the two times slower scan speed should be the half value of the standard speed. However, the highest peak in the experiment had a value of only 1.13 times higher and 0.85 times lower than the standard, respectively. These difference in value was almost the same. It could be expected that the fact that the faster the scan speed, the higher the sputtering yield.

Figure 3.7(b) presents normalized curves at the maximum height of Fig. 3.7(a), it was shown that the all of three derivative graphs had coincided as one graph. In the experiments, although the shave-off was conducted the samples with different scan speed, the condition of the primary ion beam was always the same as the beam current of 260 pA. Thus all three derivations of the cross-sectional shape shown that a one graph which was regarded as a profile of the primary ion beam.

As reported by Vladov et al. [3.14], the effective footprint of a primary beam which causes damage to the surface is larger than the physical size of the beam, and they defined the effective footprint as an “apparent beam size”. This experiment had also been shown that the nominal beam size presented in the FIB apparatus was 40 nm, but the results of the experiment showed 147 nm. The beam profile obtained by the cross-sectional shape was about 3.7 times larger than equipped beam size. From the results, we could assume the apparent beam size which has effectively influenced on the sample.

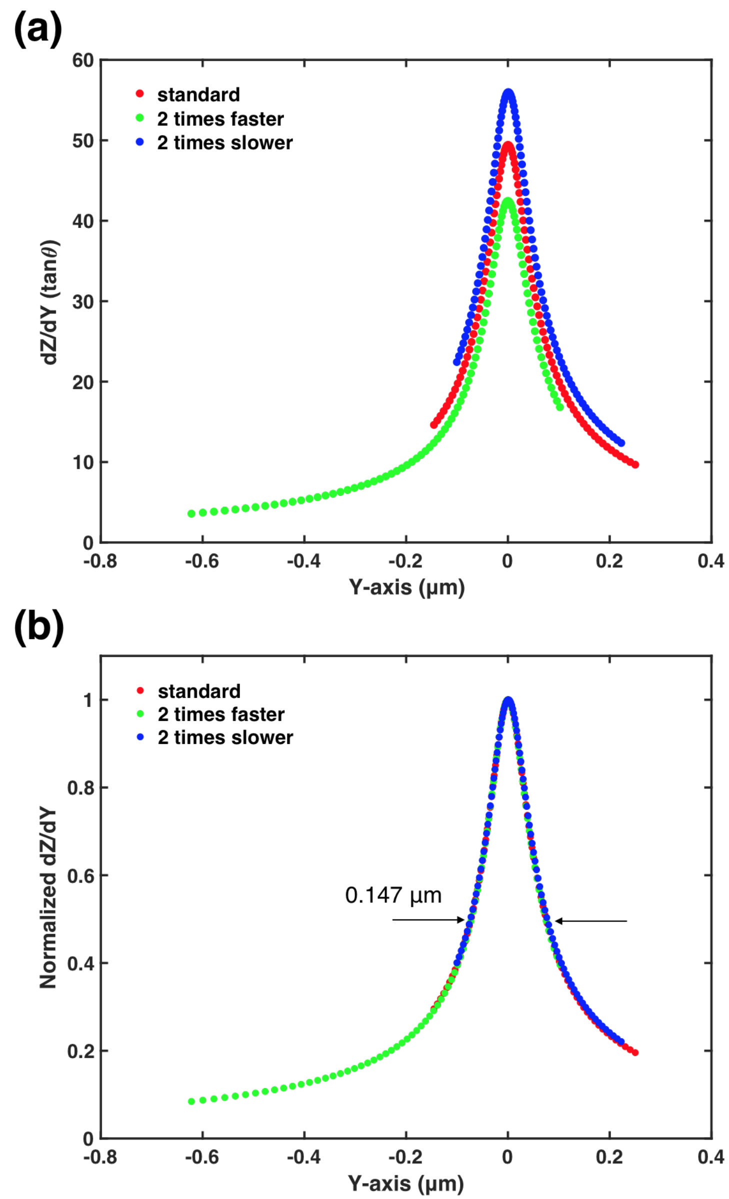


**Fig. 3.7** (a) Differential graphs of Fig. 3.3(b) where the peaks are set as 0 μm on the Y-axis. (b) The normalized graph of Fig. 3.7(a).

## 3.4 Conclusion

The angle of incidence is an important parameter to affect several functions in the sputtering process. In the shave-off method, the slope of the cross section is closely related to the angle of incidence due to the unique sectioning technique, and the cross-sectional shape could be changed by the scan speed. From the comparison of three different shave-off scan speeds on the tungsten sample, I could conclude that the slope of the cross sections increased with decreasing scan speed. Moreover, the sputtering yield decreases with decreasing scan speed and with increasing the angle of incidence. This result is opposite to the tendency of the raster scan method because the shave-off method is usually conducted with a larger the angle of incidence than the raster scan method. In this experiment condition, the sputtering yield decreased for the angles of incidence larger than 75°. This is due to the increase in the reflection of incidence ions at the sample surface. In addition, I could assume the beam profile from the cross-sectional shape. Although the cross sections have different shapes as a function of scan speed, the normalized derivative graphs have been shown as one composite graph. It could be estimated as an apparent beam size of 147 nm.

Going forward, I expect that this study would enable us to calculate the scan speed and angle of incidence for getting the highest sputtering yield on our shave-off method.

## 3.5 References


3.1 A. Benninghoven, F. G. Rüdenauer and H. W. Werner, "*Secondary Ion Mass Spectrometry: Basic Concepts, Instrumental Aspects, Applications, and Trends*," J. Wiley, 1987.

3.2 Y. Takagi, S. Kang, K. Matsumura, T. Azuma, B. Tomiyasu and M. Owari, *e-Journal Surf. Sci. Nanotechnol.*, 2018, **16**, 324–328.

3.3 C. Li, G. Habler, L. C. Baldwin and R. Abart, *Ultramicroscopy*, 2018, **184**, 310–317.

3.4 D. Santamore, K. Edinger, J. H. Orloff and J. Melngailis, *J. Vac. Sci. Technol. B.*, 1997, **15**, 2346–2349.

3.5 M. Y. Ali, W. Hung and F. Yongqi, *Int. J. Precis. Eng. Manuf.*, 2010, **11**, 157–170.

3.6 C. S. Kim, S. H. Ahn and D. Y. Jang, *Vacuum*, 2012, **86**, 1014–1035.

3.7 D. P. Adams and M. J. Vasile, *J. Vac. Sci. Technol. B*, 2006, **24**, 836–844.

3.8 H. B. Kim, G. Hobler, A. Lugstein and E. Bertagnolli, *J. Micromechanics Microengineering*, 2007, **17**, 1178–1183.

3.9 L. Frey, C. Lehrer and H. Ryssel, *Appl. Phys. A Mater. Sci. Process.*, 2003, **76**, 1017–1023.

3.10 G. Carter, M. J. Nobes, K. I. Arshak, R. P. Webb, D. Evanson, B. D. L. Eghawary and J. H. Williamson, *J. Mater. Sci.,* 1979, **14**, 728–736.

3.11 T. Ishitani and T. Ohnishi, *Jpn. J. Appl. Phys.,* 1989, **28**, L320–L322.

3.12 J. F. Ziegler, M. D. Ziegler and J. P. Biersack, *Nucl. Instruments Methods Phys. Res. Sect. B*, 2010, **268**, 1818–1823.

3.13 A. Mutzke, R. Schneider, W. Eckstein, R. Dohmen, Max-Planck-Institute for Plasma-physics, IPP-Report, 2011, 12/8, 1–70.

3.14 N. Vladov, J. Segal and S. Ratchev, *J. Vac. Sci. Technol. B.*, 2015, **33**, 41803 1–6.

# CHAPTER IV

## ANGULAR & ENERGY DISTRIBUTION OF SPUTTERD PARTICLES

In this chapter, the angular distribution and the energy distribution of secondary ions were investigated by the simulation. The information of emission angle and initial energy is one of the essential parameters for the development of three-dimensional (3D) shave-off SIMS which is directly related to the detection position. The simulation was conducted for 30 keV gallium ion beam irradiation on the tungsten sample by using SDTrimSP program, one kind of Monte-Carlo simulations. Firstly, I investigated whether or not the simulation program has good agreement with experimental data under the shave-off condition, then the angular distribution and energy distribution of sputtered W particles were simulated according to the angle of incidence.

### 4.1 Introduction

In the 3D shave-off system, our group proposed to introduce the cylindrical lens system (magnification lens system) which magnifies the depth locational information of secondary ions from a few micrometers to some millimeters scale. The magnified sample depth information has appeared to the Z-axis of a detector with elemental analysis (mass information m/z, X-axis of the detector) at the same time. As our previous report [4.1], the sample depth locational information on the detector depended on both the initial energy and emission angle of secondary ions. In particular, the angle distribution critically affected on detection position of the secondary ions, and it is the most critical and essential element to develop the 3D shave-off method. In this chapter, I investigated the angular distribution and energy distribution of sputtered particles using the Monte Carlo simulation SDTrimSP code with the shave-off condition. Today there are many computer simulations to research on the sputtering process such as SRIM/TRIM [4.2, 3], TRIDYN [4.4], MC_SIM [4.5], Geant4 [4.6] and SDTrimSP [4.7]. The simulations based on the

Monte Carlo simulations of binary collision process have been spread used to obtain features of the sputtering process, and its applications accompanied by the development of computer simulation. These computer simulations were variously compared with the experimental data of the sputtering yield, angular emission, and energy distribution [4.8-11] and they often obtained reasonable quantitative agreement.

Among the Monte Carlo simulations, the SDTrimSP code had been reported particular good agreement with experimental data of angular distribution better than the other simulation programs with common scanning condition [4.9, 11]. However, it was usually performed with a normal sputtering condition, and there is relatively little information about the simulation program for shave-off conditions implemented with the gallium focused ion beam at high energy (over 20 keV) and a high angle of incidence (over 80°).

Therefore, firstly I needed to verify that the SDTrimSP simulation results are in good agreement with experimental data even under the shave-off condition. The simulation for the angular distribution of the sputtered particle was conducted based on existing two experimental data and the results were compared. One of the experimental data is for the condition of the high incidence of energy, and the other is for the condition of a high angle of incidence. After that, the angular distribution and energy distribution of sputtered particles were simulated with the shave-off condition for 30 keV $Ga^+$ ion irradiation of tungsten sample at 87° ion incidence angle.

## 4.2 SDTrimSP simulation with shave-off condition

The simulation was conducted based on two shave-off condition experiments. For high incident energy condition, 30 keV of $Ga^+$ ions were incident on the Au at incident angle of 0°. For high angle of incidence condition, 20 keV $Ga^+$ ion beam were irradiated to the Si at incident angle of 87°

### 4.2.1 Method

All of the simulations for the angular distribution were performed with SDTrimSP (version 5.07) [4.12]. The input parameters of the simulation followed each existing experimental condition, and the surface binding energies of target were 3.79 eV (Au) and 4.72 eV (Si) which were tabulated by the program. The simulation used calculation results

with the extracted sputtered particles (10,000 of Au particles and 605,000 of Si particles) from 100,000 of incident $Ga^+$ ions. When the primary ion beam is irradiated the sample surface with an incident angle (θ), the angular distribution is indicated by the polar angle (φ), and azimuthal angle (ψ) of the sputtered particle (Fig. 4.1).

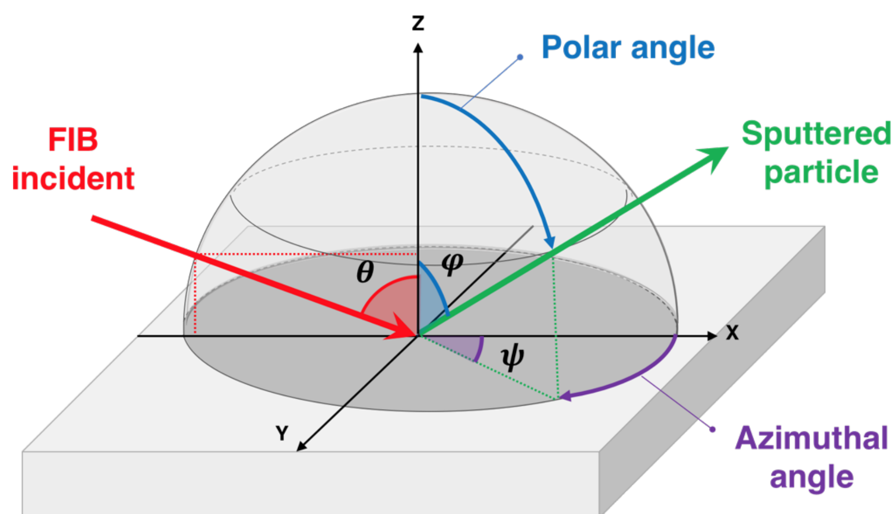


**Fig. 4.1** Geometry for the sputtered particles, where θ denotes the angle of incidence, φ is the polar angle and $\psi$ is the azimuthal angle.

First, as the condition of high incident energy, 30 keV $Ga^+$ ions were irradiated on a gold film at a normal incident angle (θ = 0°) along the scanning length (l) of 40 μm. The angular distribution of the sputtered gold particles were measured from the deposit position on the silicon substrate. The silicon substrate is located vertically at the height (h) of 10 μm, and the deposit position (P1) was calculated by using the simulation results of polar angle and azimuthal angle. The condition was illustrated as shown in Fig. 4.2(a).

The second investigation was conducted at a high angle of incidence. A silicon wafer is bombarded by $Ga^+$ ions of 20 keV at 87 degrees. Figure 4.2(b) depicts the experimental system for measuring the angular distribution of secondary ions with a high angle of incidence. The secondary ions which had energy under 10 eV were measured by position sensitive detector. The detector system composed of a grounded mesh grid, microchannel

plates (MCP) and resistive anode encoder (RAE), all of which are located parallel to the focused ion beam (FIB). The angular distribution of silicon sputtered particles were calculated as the deposit position (P2) on the detector using SDTrimSP and SIMION (SIMION Ver. 8.1, Scientific Instrument Services) program. To investigate the direction of secondary ions, the angular distribution was examined by changing the distance (d) which from the first layer of MCP to the FIB as 10 mm, 15 mm, and 20 mm.

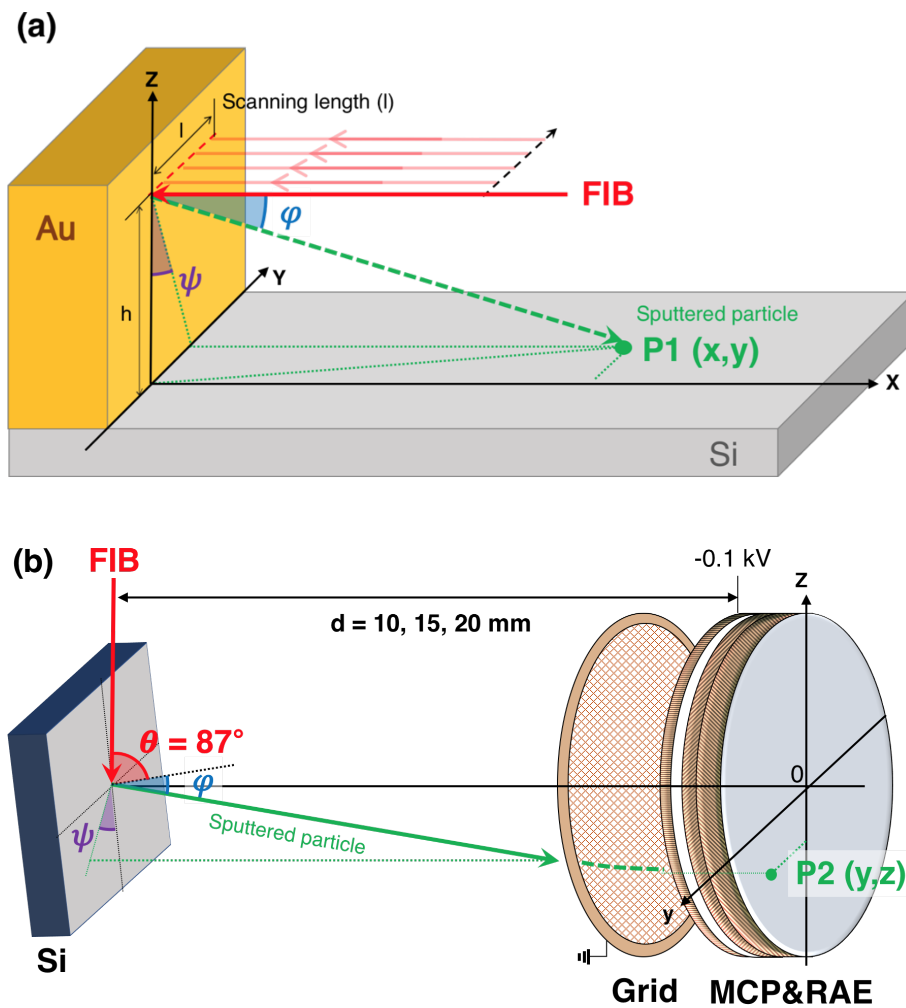


**Fig. 4.2** Schematic illustration of the shave-off experimental conditions. (a) High incident energy; Deposition of Au particles sputtered by 30 keV $Ga^+$ ions irradiation at a normal incidence angle (0°) on a Si substrate. (b) High incident angle; Position on the MCP of sputtered Si particles sputtered by 20 keV $Ga^+$ ions irradiation at 87°.

### 4.2.2 High incident energy

At the first example for high incident energy, the gold film was irradiated by 30 keV $Ga^+$ ions at the normal incident angle. Figure 4.3 shows the result of the angular distribution of the sputtering yield per solid angle resulted in this condition. The sputtered gold particles showed distribution symmetrically at azimuthal angles (0-180°), and at polar angles below about 30 degrees showed high sputtering yields.

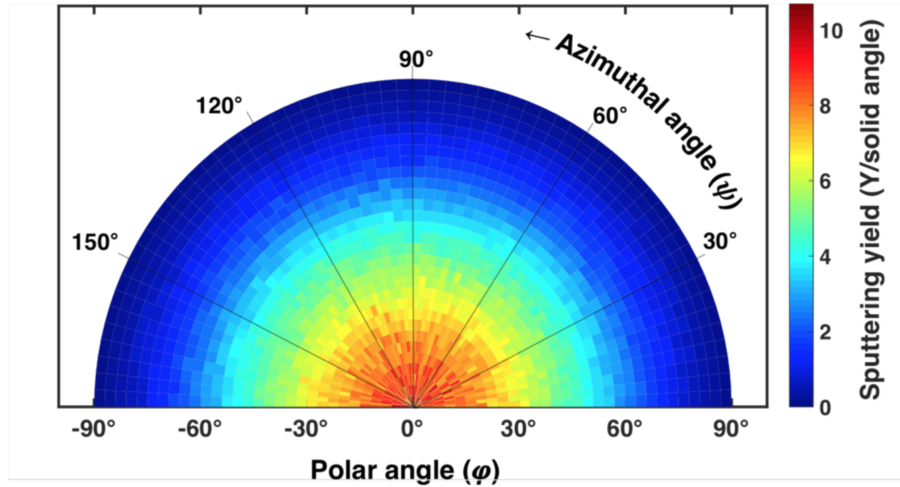


**Fig. 4.3** Contour plot of the angular distribution of the sputtered Au particles. The color bar indicates the sputtering yield per solid angle for Au atoms

For comparison to existing experimental data [4.13], I calculated the deposit positions of gold sputtered particles using the simulation results of emission angles (polar angle (φ) and azimuthal angle (ψ)). In the simulation, $10^5$ $Ga^+$ ions irradiated to the Au target, $10^4$ of particles among the total sputtered Au particles were extracted and used for the calculation. When the FIB irradiated at a point of Au target, the deposit position (P1) of sputtered Au particles on the Si substrate is calculated by Eq. 4–1.

$$P1\ (x) = \frac{1}{tan\varphi \times cos\psi}, \qquad P1\ (y) = \tan\psi \qquad (4-1)$$

Figure 4.4(a) shows the deposited Au particles by the FIB irradiated at one point on the Si substrate calculated by Eq. 4–1. It was represented by the histogram (Fig. 4.4(b)), the particles had the highest distribution at 12.5 μm of X-axis.

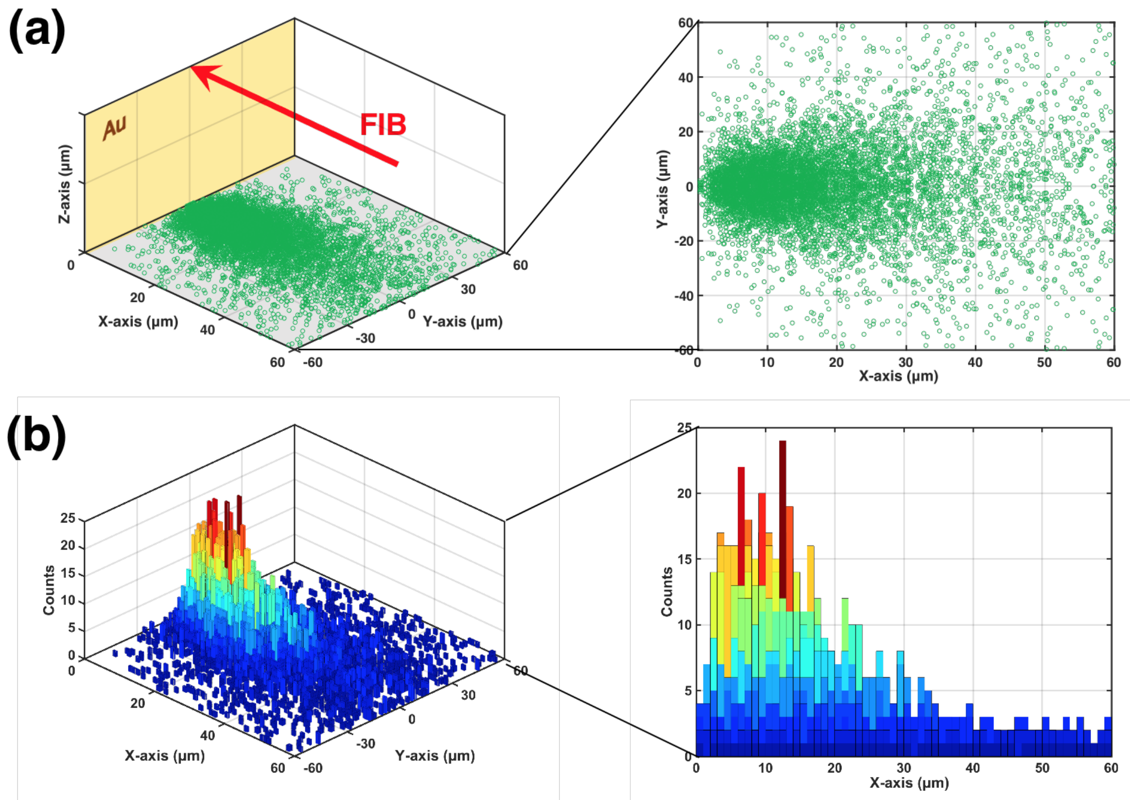


**Fig. 4.4** Deposited position of Au particles (green dot) on the Si substrate from FIB irradiated at a point. (a) Scatter plot of Au particles on Si substrate. (b) Histogram of (a).

In the experiment, the deposited particles were sputtered by line scanning for scanning length (l = 40 μm). Therefore, the Au particles sputtered from one point was recalculated to move up 40 μm by 1μm along the Y-axis, the results was presented as shown in Fig. 4.5(a). For comparison to experimental data, the Z-axis of histogram values were normalized, Fig. 4.5(b) shows the simulation result and experimental data of the side view along the XZ plane. In the experiment, thickness of the deposit film on the Si substrate were measured by a confocal laser scanning microscope, and the cross-section shape was

indicated as a dashed line in Fig. 4.5 (b). The simulation result shows good agreement with the experimental data. The emission angle calculated from the peak top of the graph (15 μm) was about 33.7 degrees ($\tan^{-1}(10/15)$). The emission angle was also in accordance with the results of polar angular distribution which showed high sputtering yield at 0-30 degrees in Fig. 4.3.

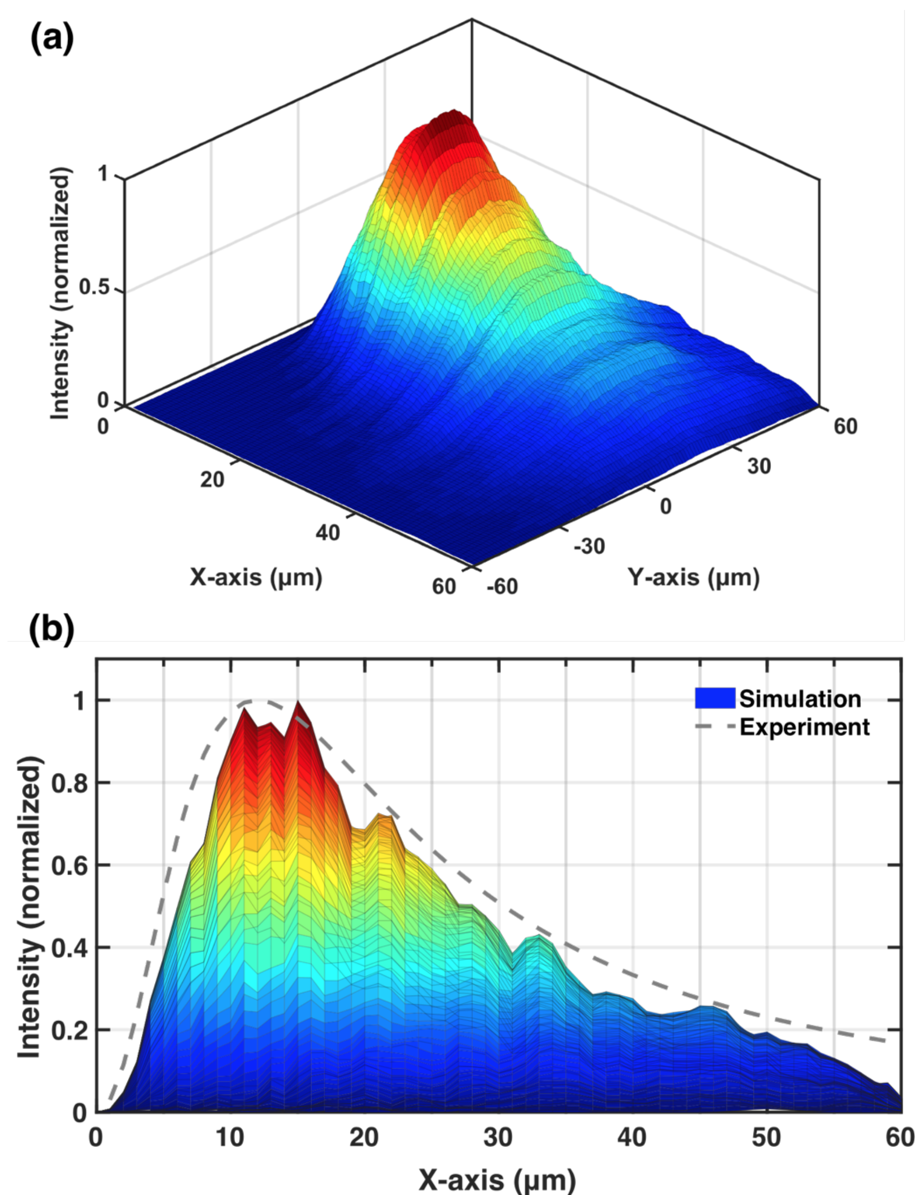


**Fig. 4.5** (a) Deposited Au particles on the Si substrate after FIB line scanning (l = 40 μm), the number of Au particles were normalized. (b) Comparison between simulation results (color) and experimental data (dash line) of deposited Au particles.

### 4.2.3 High angle of incidence

As the second example for the condition of the high angle of incidence, the simulation was conducted for 20 keV $Ga^+$ ions irradiated on the Si with 87 degrees of angle of incidence. The angular distribution for the sputtered Si particles are shown in Fig. 4.6(a). For comparison with existing experimental data [4.14], the angular distribution of the Si sputtered particles was calculated as a detection position (P2) on the detector by Eq. 4–2.

$$P2\ (y) = \tan\psi \times |z|,$$

$$P2\ (z) = \frac{I}{tan(90 - \boldsymbol{\theta}) + (\sqrt{(1 + tan^2\psi)} \times tan\ (\mathbf{90} - \boldsymbol{\varphi}))} \qquad (4-2)$$

Figure 4.6(b) shows the distribution of the sputtered Si particles position on the detector from the calculation by Eq. 4–2. The detection position could calculate only the half part of the detector due to 0-180° of azimuthal angle, but the other part also has the same with them as symmetric distribution.

In the simulation result of the angular distribution, the silicon particles sputtered had a slight out about 10° with the opposite direction of FIB from the vertical direction of the sample surface. It had shown on the detector, the distribution of sputtered particles has a downward direction to 5 mm from the center of the detector.

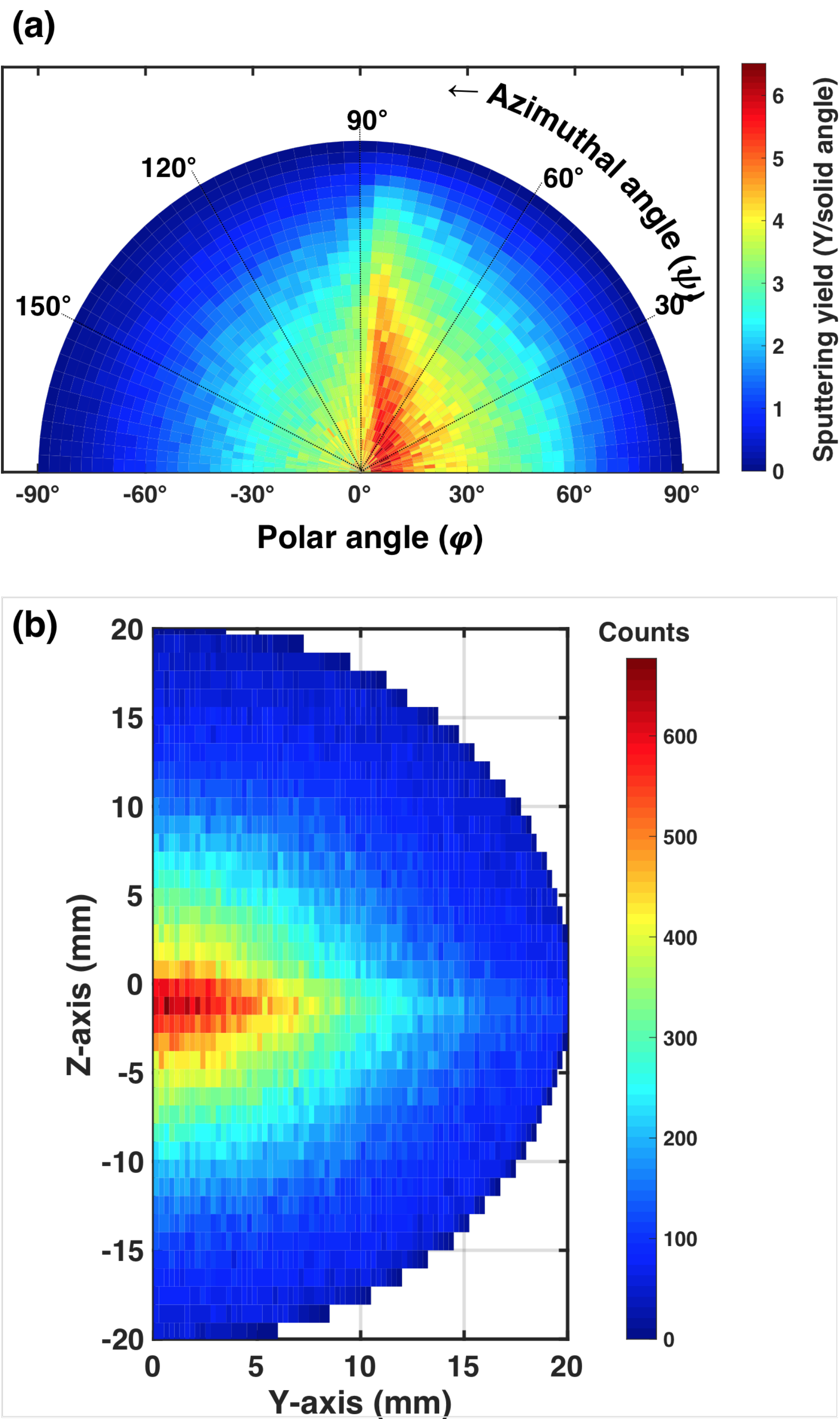


**Fig. 4.6** Simulation results for 20 keV $Ga^+$ ion irradiation on Si with a high incidence angle of 87°. (a) The angular distribution and (b) Position distribution on the detector for the sputtered particles. The color bars represent (a) the sputtering yield per solid angle and (b) the number of Si particles.

In this experiment, there is an electric field which was generated between the grounded mesh and the first layer of the MCP (- 0.10 kV), and it expected to affect to the trajectories of secondary ions. Therefore, the angular distribution was calculated including the electric field effects by using SIMION program. Based on the emission information (polar angles, azimuthal angles, and energy) obtained by SDTrimSP simulation, the final deposit position (P2 in Fig. 4.2(b)) on the detector was calculated using the SIMION program. Figure 4.7 compares the simulation results and experimental results when the distance between sample and detector is d = 10 mm (a), 15 mm (b), and 20 mm (c). In the existing experiment, the secondary ions had measured as the number of counts on the detector, and it had been obtained only along the Z-axis of the detector due to a limitation of A/D convert system. Therefore, the Z-axis data of the simulation results were presented by a sum of X-axis counts number, it was compared with the experimental result. The particle counts of each result were normalized for comparison, the sample position of Z-axis was set as the zero (0 mm).

All three distributions of the simulation results were located above the distribution of the experimental data as shown in Fig. 4.7. The experimental results showed that the emission direction of secondary ions is going to downward (negative value of Z-axis). However, in the simulation, the most of sputtered silicon particles having the energy under 10 eV were emitted in a vertical direction from the FIB (0 mm of Z-axis). The direction of the distribution about 5 mm downward in Fig. 4.6 was changed to the vertical direction of the sample surface by the electric field. The peak of the simulation distribution graph shows split ends, and it was supposed to occur due to the pass of the mesh grid. As the length (d) increase, the area of distribution showed wider in both simulations and experiments, the difference between simulation results and experimental data also increased. The angular distribution of simulations showed a difference about 3 mm (d = 10 mm), 5 mm (d = 15 mm), 7 mm (d= 20 mm) from the experimental data. The difference was represented by the average emission angle of about 18 degrees (the average angles of $\tan^{-1}(3/10)$, $\tan^{-1}(5/15)$, and $\tan^{-1}(7/20)$).

The simulation results had smaller emission angles than experimental results, but it was shown quite a similar shape of the distribution to the experimental results for the angular distribution of sputtered particles.

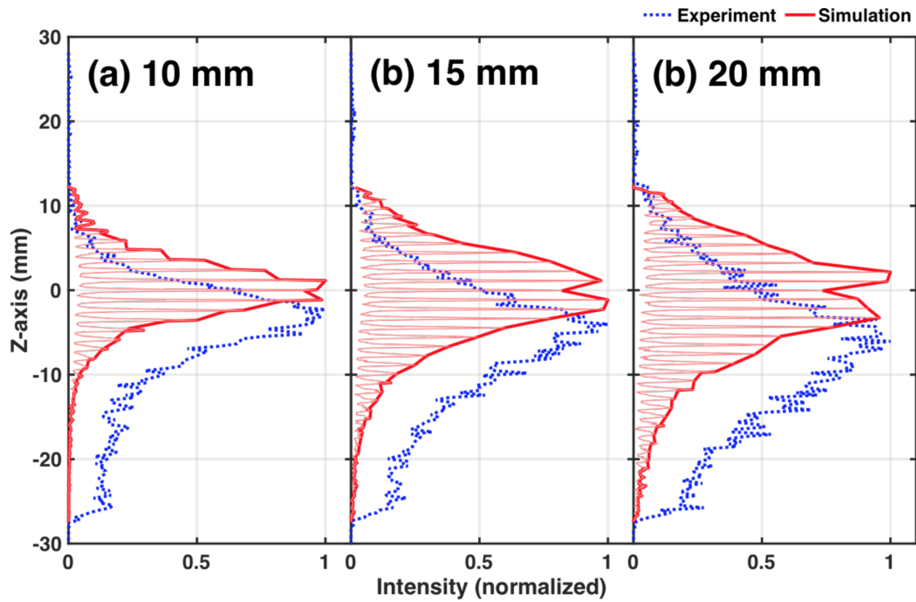


**Fig. 4.7** The number of normalized counts along the Z axis of the detector when the distance (d) between the sample and the detector are 10 mm (a), 15 mm (b), and 20 mm (c).

### 4.3 Angular distribution of sputtered W particles

From the previous section, the SDTrimSP program could be concluded that it shows a good agreement under the shave-off scanning condition. In this section, the angular distribution of sputtered tungsten particles emitted by 30 keV $Ga^+$ ions irradiation was simulated as a function of the angle of incidence using the SDTrimSP program.

The angular distributions of sputtered tungsten particles were simulated as a function of the angles of incidence ($\theta$ = 0°, 30°, 45°, 60°, and 87°) of FIB for the bombardment with 30 keV $Ga^+$ ions. Figure 4.8 shows the emission angles (polar angle ($\varphi$) and azimuthal angle ($\psi$)) of sputtering yield per solid angle (SY/$\Omega$). The polar plots show that symmetric distribution to surface normal direction at the angle of incidence of 0° and 45°, and 60°, the sputtered particles shows asymmetrically distributed on positive polar angle direction. At an incidence of the angle of 87°, the angular distribution shows slightly skewed direction toward the azimuthal angle of 80°-90° with the polar angle of 0°-30°.

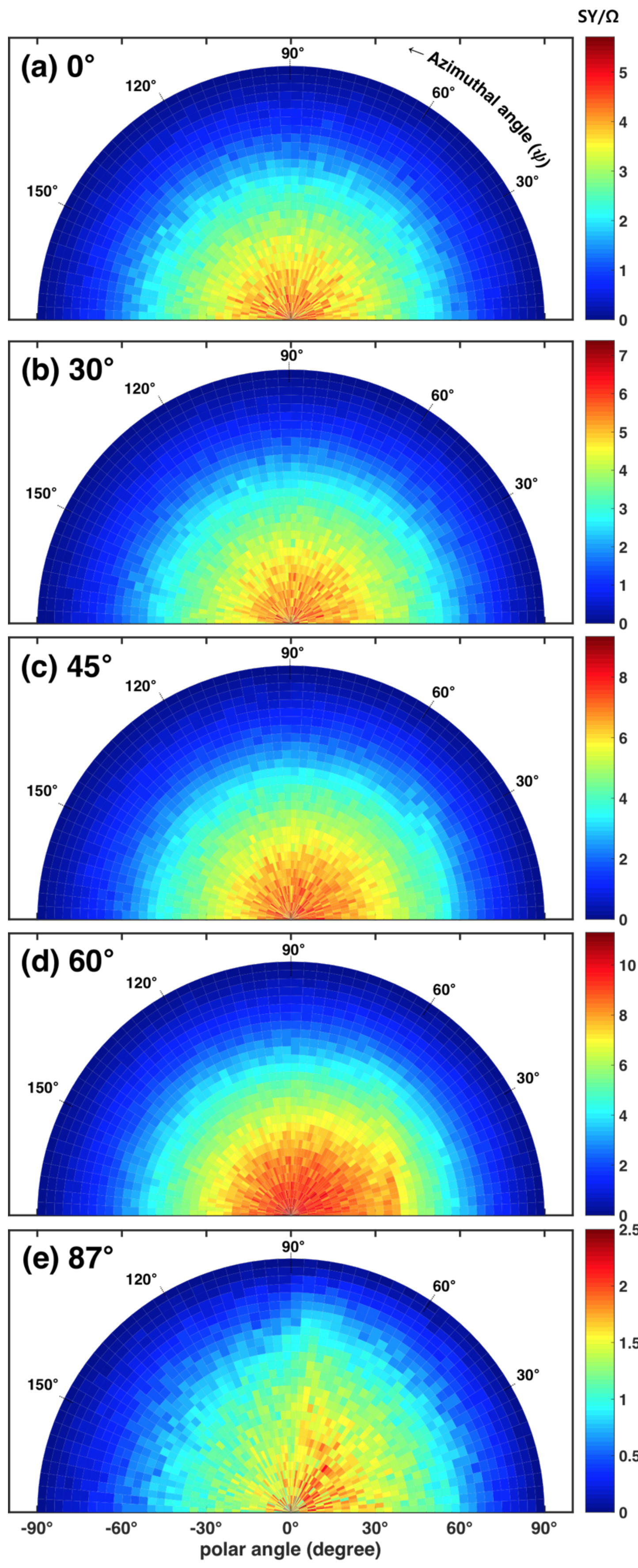


**Fig. 4.8** Contour plot of angular distribution with polar angle and azimuthal angle as a function of angle of incidence. (a) 0°, (b) 30°, (c) 45°, (d) 60°, and (e) 87°. The color bar indicated the sputtering yield per solid angle (SY/Ω).

Figure 4.9 presents the plots of emission angles of $10^5$ sputtered particles for ions incident at θ = 0°, 30°, 45°, 60°, and 87°. The emission angle calculated the angular distribution by a stereographic projection to the XZ plane of the emission hemisphere (Figure 4.1). For the comparison of the emission direction, the number of particles is normalized, the distributions are fitted with a cosine function as follows [4.15].

$$F(\theta) = cos^n(\theta)$$

where, $\theta$ is the angle of emission, n is the cosine exponent (under-cosine for $n < 1$and over-cosine for $n > 1$).

All the distribution curves had an over-cosine tendency on the fitting curve which n was 2. It could observe that the angular distributions had in a direction to peak 0°. When the incidence increases 0° to 87°, the peak shifted to the higher emission direction of 15°, and the distributions were slightly narrow.

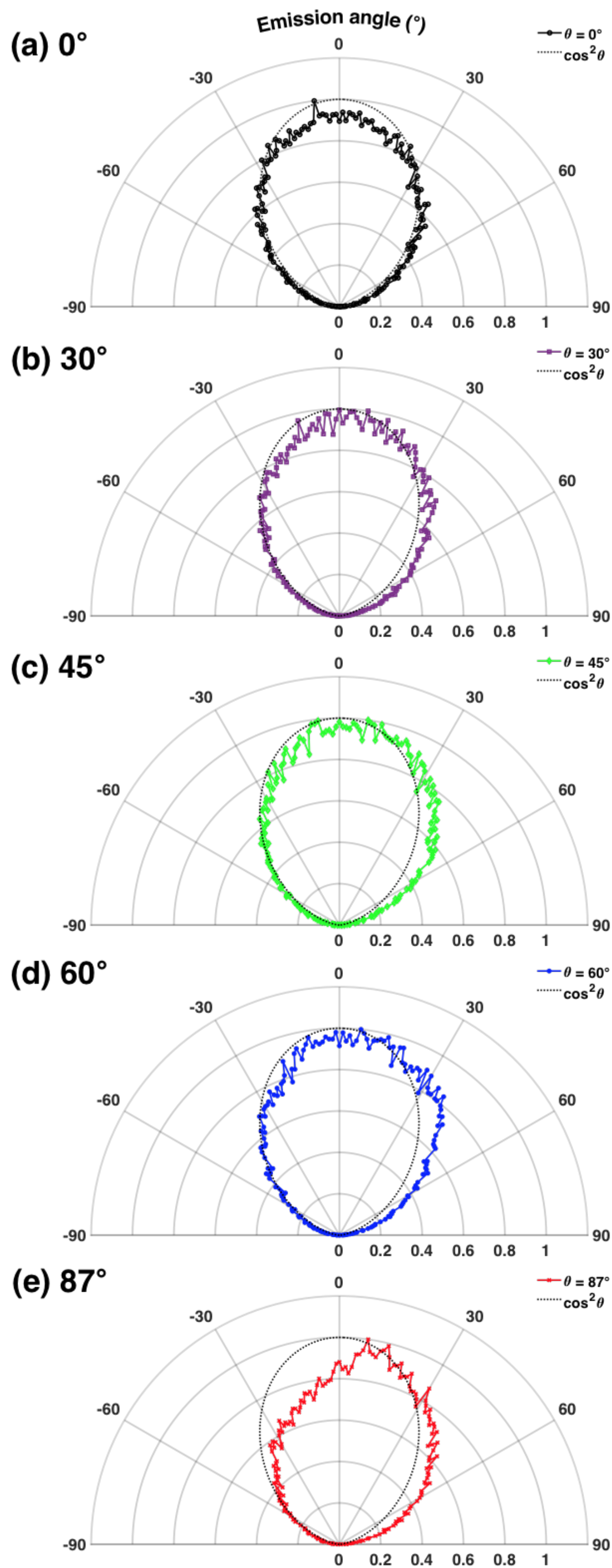


**Fig. 4.9** Angular distribution (emission angle) of sputtered W particles by 30 keV $Ga^+$ ions irradiation at the angle of incidence of (a) 0°, (b) 30°, (c) 45°, (d) 60°, and (e) 87°.
Dotted line is fitted cosine curve.

## 4.4 Energy distribution of sputtered W particles

The initial kinetic energy of secondary ions is an essential parameter to calculate related with ion velocities and divergent paths of the ion trajectories in the SIMS apparatus. The energy distribution of secondary ions of the sample depends on the emission angle, sample species, and bombardment conditions [4.16]. Figures 4.10 and 4.11 show the energy distribution of the sputtered tungsten particles for the bombardment incidence by $10^4$ of $Ga^+$ ions as a function of the angle of incidence ($\theta$ = 0°, 30°, 45°, 60°, and 87°). The energy of sputtered particles increases with increasing angle of incidence angle, and the particles which having highest energy are in direction on the increasing polar angle as shown in Fig. 4.10. Figure 4.11 shows the energy distributions at a selected energy range of 0–30°. All curves have a peak at around energy of 5 eV, the number of particles is increased with increasing angle of incidence until 60° and decreased at 87° due to the difference for sputtering yield.

In this simulation, the sputtered particles represent all particles which composed neutral, ions, molecules, and I could not distinguish that from the results. However, it is expected that the secondary ion energy distribution will not be significantly different from the result because it relates to the sputtered neutral energy distribution by a charged fraction of the sputtered species [4.17].

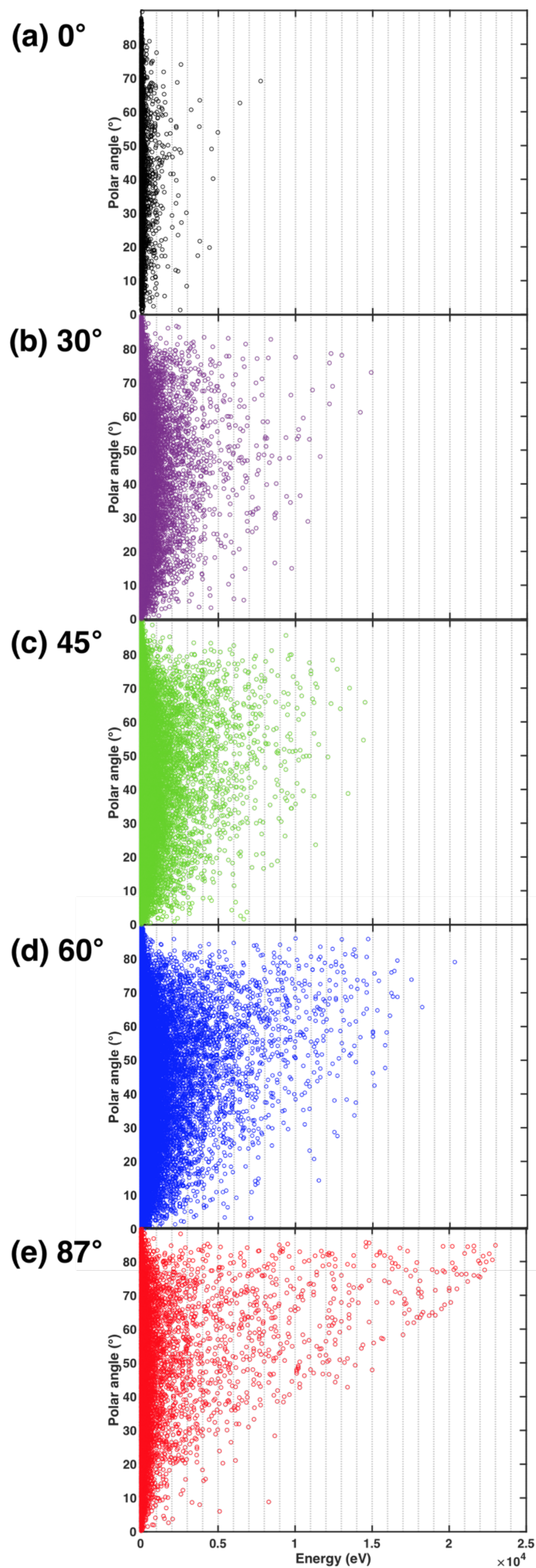


**Fig. 4.10** Energy distribution for 30 keV $Ga^+$ ions in W at the angle of incidence of (a) 0°, (b) 30°, (c) 45°, (d) 60°, and (e) 87° as a function of polar angle.

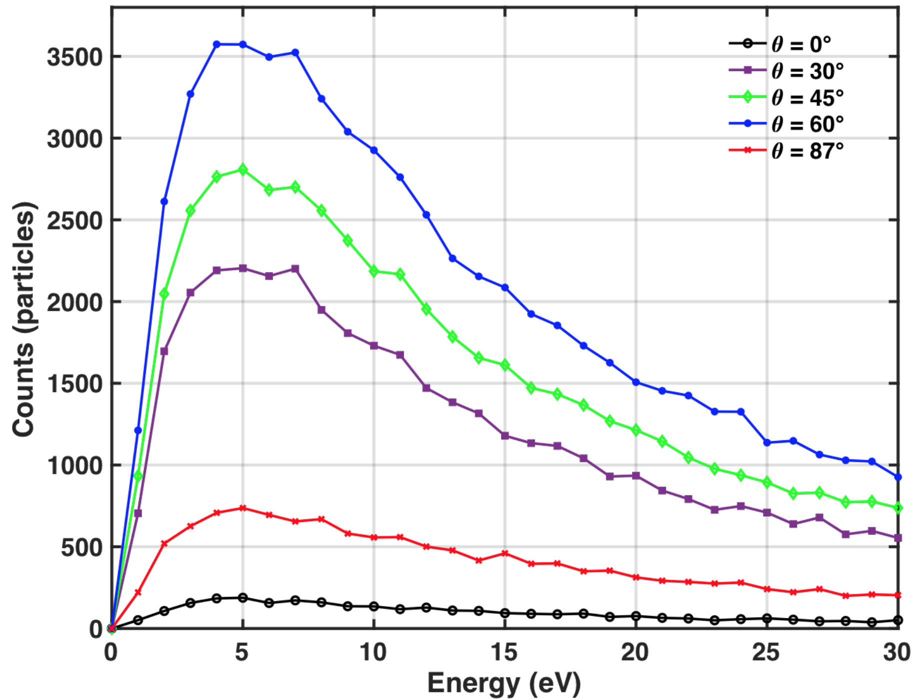


**Fig. 4.11** Energy distribution of sputtered W particles at a range 0-100 eV in accordance angle of incidence.

## 4.5 Conclusion

Monte Carlo simulation is widely used to calculate the sputtering process. Today, there are many Monte Carlo simulations, among them the SDTrimSP binary simulation codes had been known that provide good agreement with experimental data, especially angular distribution better than other programs [4.18]. Therefore, I tried to investigate the angular distribution using SDTrimSP program, but the program had no reference corresponding to shave-off method, which conducted with high energy (>20 keV $Ga^+$) and high angle of incidence. Hence, firstly I simulated the angular distribution with existing shave-off experimental conditions and compared with the experimental data. The comparisons were performed with two conditions; one is high incidence energy of 30 keV $Ga^+$ ions, the other is a high angle of incidence of 87 degrees with 20 keV $Ga^+$ ions.

At high incidence energy, the angular distribution of sputtered gold particles was simulated for 30 keV $Ga^+$ ions irradiation at the normal angle of incidence (0 degree).

The angular distribution was measured by calculating the deposit position, the simulation result showed good agreement with the experimental data.

As the simulation under the condition of high incident angle, the silicon was irradiated with 20 keV of $Ga^{+}$ ions incident at 87 degrees. The angular distribution of sputtered silicon particles showed toward for the polar angle of 0-30 degrees, and the sputtered particles having the energy under 10 eV exhibited a perpendicular direction to the FIB. However, the experimental results showed that the angular distribution of secondary ions is directed to downward with a difference about 18 degrees with simulation results. Although the simulation results are not completely in accordance with shave-off experimental data, they showed an acceptable similar tendency for the experimental data.

The angular distribution and energy distribution of sputtered tungsten particles were investigated by the angle of incidence using the SDTrimSP program. For the 30 keV $Ga^{+}$ ions irradiation on the W sample, the sputtered W particles had clear difference behaviors by the angle of incidence. In particular, at a high angle of incidence (87°) which is conducted at shave-off scan mode, the angular distribution has a direction about emission angle of 15°, and the energy distribution of the sputtered particles was distinguished by the polar angle.

The SDTrimSP simulation is expected to help obtain the angular distribution of sputtered particles under shave-off conditions. Moreover, it will be able to provide the basic parameter for calculating of the secondary ion trajectories along the lens system and detector in development of 3D shave-off SIMS.

## 4.6 References


4.1 Y. Takagi, S. Kang, K. Matsumura, T. Azuma, B. Tomiyasu and M. Owari, *e-Journal Surf. Sci. Nanotechnol.*, 2018, **16**, 324–328.

4.2 J. Ziegler, J.P. Biersack, M.D. Ziegler, SRIM-The Stopping and Ranges of Ions in Solids, SRIM Co., Chester, 2008.

4.3 SRIM www.srim.org.

4.4 W. Möller, W. Eckstein, J.P. Biersack, *Comput. Phys. Commun.*, 1988, **51**, 355–368.

4.5 M. Ullrich, A. Burenkov and H. Ryssel, *Nucl. Instrum. Methods B*., 2005 **228**, 373–377.

4.6 Geant4 http://geant4.cern.ch/

4.7 W. Eckstein, H.M. Urbassek, *“Computer simulation of the sputtering process,”* 110, Springer, Berlin, 2007, pp. 21–32.

4.8 T. Lautenschläger, R. Feder, H. Neumann, C. Rice, M. Schubert and C. Bundesmann, *Nucl. Instruments Methods Phys. Res. Sect. B Beam Interact. with Mater. Atoms*, 2017, **385**, 30–39.

4.9 R. Feder, C. Bundesmann, H. Neumann and B. Rauschenbach, *Nucl. Instruments Methods Phys. Res. Sect. B Beam Interact. with Mater. Atoms*, 2014, **334**, 88–95.

4.10 R. Becerra-Acevedo, J. Bohdansky, W. Eckstein and J. Roth, *Nucl. Inst. Methods Phys. Res. B*, 1984, **2**, 631–634.

4.11 J. Roth, J. Bohdansky and W. Eckstein, *Nucl. Instruments Methods Phys. Res.*, 1983, **218**, 751–756.

4.12 A. Mutzke, R. Schneider, W. Eckstein, R. Dohmen, Max-Planck-Institute for Plasma-physics, IPP-Report, 2011, 12/8, 1–70.

4.13 S. Akiba, A. Yamazaki and D. Shirakura, B. Tomiyasu and M. Owari, *e-Journal Surf. Sci. Nanotechnol.*, 2016, **14**, 87–91.

4.14 浅倉浩之, 2016, 三次元 shave-off 法に向けた イオン放出角に関する研究 修士論文, 東京大学

4.15 M. Ait, El Fqih, *Eur. Phys. J. D*, 2010, **56**, 167–172.

4.16 V. E. Yurasova, V. T. Cherepin and Y. A. Ryzhov, *J. Surf. Investig. X-ray, Synchrotron Neutron Tech.*, 2011, **5**, 465–483.

4.17 J. N. Smith, *J. Nucl. Mater.*, 1978, **78**, 117–124.

4.18 H. Hofsäss, K. Zhang and A. Mutzke, *Appl. Surf. Sci.*, 2014, **310**, 134–141.

# CHAPTER V

## SIMULATION OF SECONDARY IONS POSITION ON THE DETECTOR

In this chapter, I simulated position on the mass detector of sputtered particles from a virtual sample which composed of two species, germanium (Ge) and silicon (Si). The investigation methods that were performed in previous chapters for sputtering parameters were conducted to the sample. In order to investigate the trajectories of the secondary ions from the sputtering process on the sample surface to the detecting on the mass detector, I designated the nine sputtering position on the target and conducted simulation with three steps using the SDTrimSP and SIMION programs. From this simulation, I could confirm that the depth information of secondary ions on the target can be distinguished on the detector in our concept of 3D shave-off SIMS.

### 5.1 Introduction

The secondary ion trajectories in the 3D shave-off SIMS system had been simulated by our members in previous [5.1, 2]. They had constructed ion optic system using Auto desk Inventor and SIMION program and verified the possibility of the magnification lens in 3D SIMS. In the simulation, the lens system could enlarge the secondary ions in only the depth direction (Z-axis) and converge at the detector. However, they had conducted the simulation just in several ranges of energies, emission angles, and elements, not include scanning parameter.

In the SIMS apparatus, the secondary ions are generated by the primary ion beam scanning. Therefore, we should consider the secondary ion trajectories from the shave-off scanning. To simulate ion trajectories along the optical transport system in SIMS apparatus, we need secondary ions information for mass, sputtered position, energy, emission angles. All of these parameters are able to be obtained by the methods used in

the previous chapters. I could measure the angular and energy distribution of sputtered particles by simulation of the SDTrimSP program based on the angle of incidence, and the angle of incidence could be measured by observation of cross-sectional shape. In the same method, I could simulate the total process which from a scanning of a sample to the detection process in the 3D shave-off SIMS system.

In this chapter, I simulated the trajectories of the sample particles through the three steps; (1) shave-off scanning process, (2) sputtering process, and (3) the detection process. From this simulation, I expected to conduct a comparison of the position difference of secondary ions on the multi-anode detector by the following factors.

1. Depth of the sample.
2. Sample species at the same depth.
3. Angle of incidence at the same sample species.

For the evaluation of them, a virtual target composed of two elements was considered and then three steps simulation were carried out.

## 5.2. Simulation model

### 5.2.1 Target

In 3D shave-off SIMS, the secondary ions sputtered from the surface of the target are finally converged on the mass detector. To investigate the position on the detector of the secondary ions, I used a virtual target which composed of two elements, one of the elements is silicon (Si), and the other is germanium (Ge). It is a combination of 27 voxels, 22 voxels of Si and 5 voxels of Ge, and each voxel is 2 μm wide in all lateral dimensions. Figure 5.1(a) illustrates a schematic diagram of the simulation target.

### 5.2.2 Sputtering position on the target

In order to investigate a difference in the position on the detector of the secondary ions by the sputtering position on the target, I designated the sputtering position of 9 points (P1 to P9) on the target. Each point was determined by the type of the elements and the

depth of the sample. Figure 5.1(b) shows the positions to investigate for the sputtering.

From the comparison with positions of P2/P4/P6/P9 on the first layer in Fig. 5.1(b), I can expect to examine the relationship between the depth of the sputtered particles from in the same element sample and detecting position.

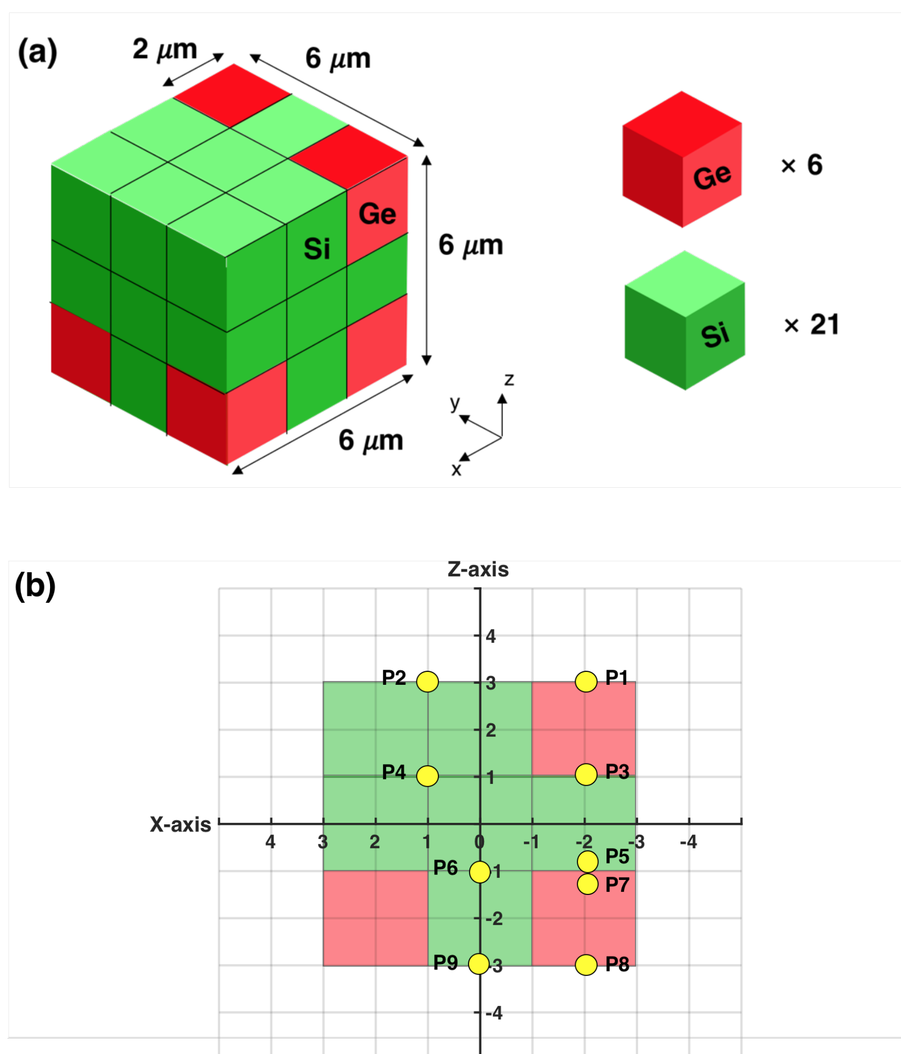


**Fig 5.1** Schematics of a target for simulation (a) Composition of a target for Ge and Si. (b) Sputtering points in a target to sputter on the target in the first layer XZ plane).

The concept of the 3D shave-off SIMS is to magnify the depth locational information of secondary ions to several mm units on the detector. In the SIMS techniques, a sample has usually some μm unit size. Therefore, we can consider the magnification of the lens through the results of this simulation. In addition, the comparison with positions of P3/P4 could verify a difference in positions of Ge and Si on detector sputtered from at the same depth position. As the previous investigation of cross-section shape under shave-off scan method, the cross sections had a slope of 87°, but the upper part of the cross-sectional shape has a smooth curve. This difference by the angle of incidence is also expected to affect the detecting of the secondary ion in the SIMS apparatus. The difference according to the angle of incidence could be examined by comparison with P1/P3/P8 in Ge, and P2/P4/P9 in Si.

### 5.2.3 Procedure of simulation.

To simulate the detection position on the mass detector of the sputtered particles from the target, I needed three information of sputtered particles, i.e., sputtered position from the target, initial energy, and emission angles. Figure 5.2 depicts the required parameters from the target for simulation and diagram of the simulation steps.

Firstly, the surface erosion simulation by the focused ion beam (FIB) was conducted to observe a cross-sectional shape of the target. From the cross-sectional shape, I could measure the angle of incidence at the designated sputtering position (P1-P9), the emission information could be obtained based on the angle of incidence by using SDTrimSP simulation program. I could perform using SIMION 8.1 program with a workbench designed our 3D shave-off SIMS system. The workbench of SIMION program for the apparatus was designed and made by our group members [5.1, 2]. The designed the workbench of 3D shave-off SIMS for SIMION program is shown in Fig. 5.3.

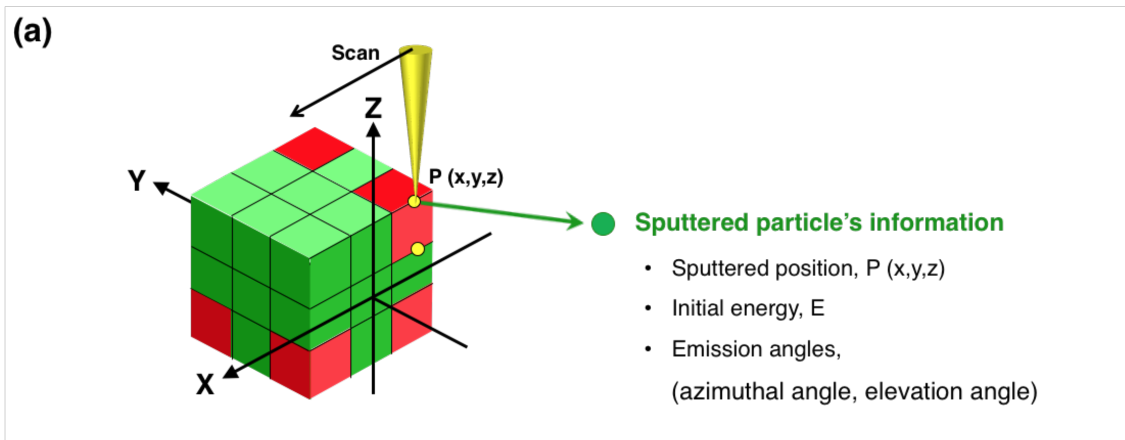


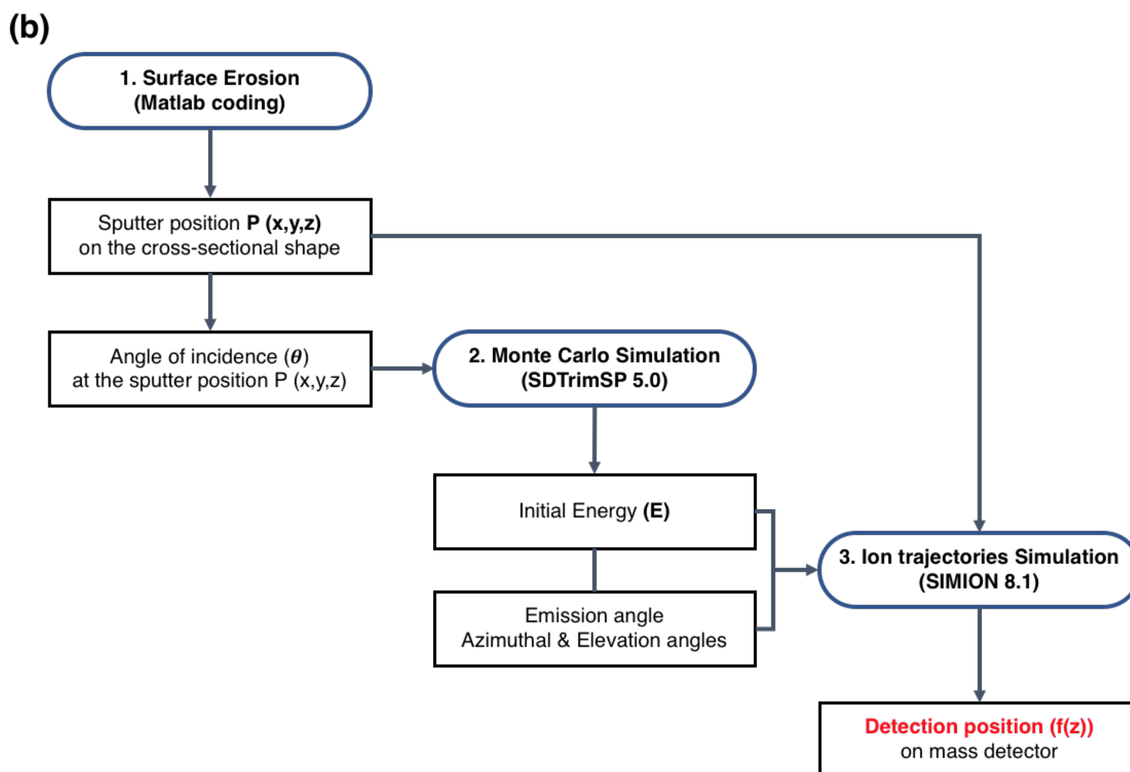


**Fig. 5.2** (a) Required parameters and obtained information from the target. (b) Three-steps for simulation.

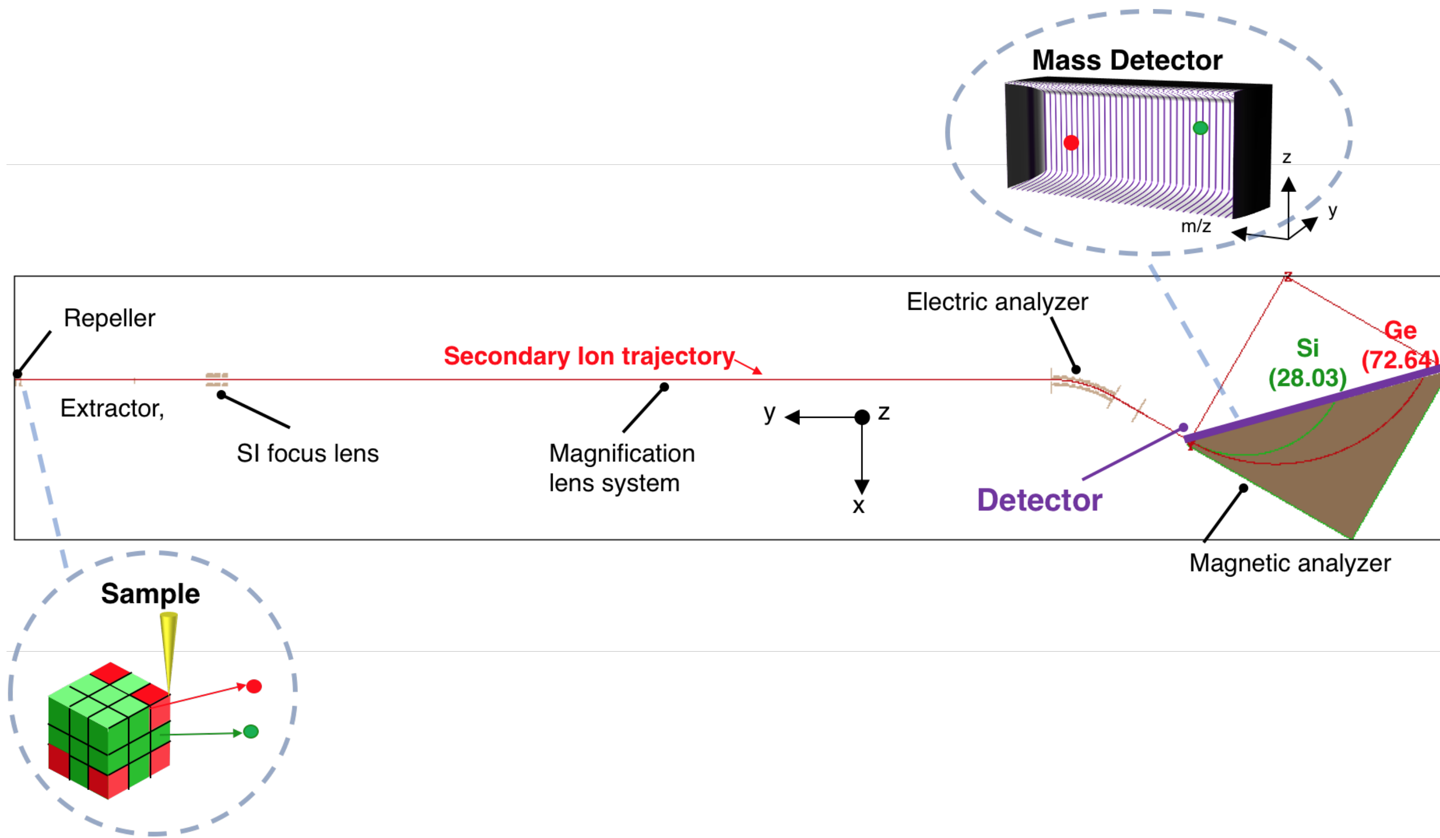


**Fig. 5.3** Design of 3D shave-off SIMS apparatus in SIMION program.

## 5.3. Simulation of surface erosion process

### 5.3.1 Procedure

At the focused ion beam system, the topography of the sputtered surface is usually guided by the assumption that the erosion depth of the target is proportional to the ion beam dose [5.3-7]. The method used for the erosion is based on a mathematical model of the combined beam deflection and sputter removal process. There have been many theoretical studies considering the re-deposition of the sputtered particles and the dependence of the sputtering yield on the incidence angle on the equation [5.8-9], but this simulation was not taken into consideration of these two factors because the shave-off method has less impact by them during the scanning.

Figure 5.4 illustrates the one-dimensional sputter model at steady-state. When the ion beam is incident to a sample with the angle of incidence ($\theta$), the rate of erosion in the ion beam direction (z) can calculate by Eq. 5–1 [5.3, 10-11]

$$\frac{\partial z}{\partial t} = -\left(\frac{J}{N}\right) S(\theta) \qquad (5-1)$$

where $J$ is the incident ion flux (ions/cm$^2$/s), $N$ is the atomic density of the target (atoms/cm$^3$), and $S(\theta)$ is the sputtering yield of the target. The FIB ion flux ($J$) is performed assuming a Gaussian beam profile expressed by Eq. 5–2 [5.12-13]

$$J(x,y) = \frac{I}{2\pi\sigma^2} \exp\left(\frac{x^2 + y^2}{2\sigma^2}\right) \qquad (5-2)$$

where, $I$ [A] is the beam current, and σ [μm] is standard deviation, $J(x,y)$ is the ion flux density at a point (x, y). Standard deviation is calculated from the beam diameter at FWHM = $(8\ln 2)^{1/2}$ σ.

All parameters for this simulation were followed standard shave-off conditions of previous experiments in Chapter III (I = 260 pA, N = $6.3 \times 10^{10}$ atoms/μm$^2$, and the beam diameter of 147 nm). The simulation for the erosion of the sample was implemented by Matlab (R2018b, Mathworks), and the code was included in APPENDIX.

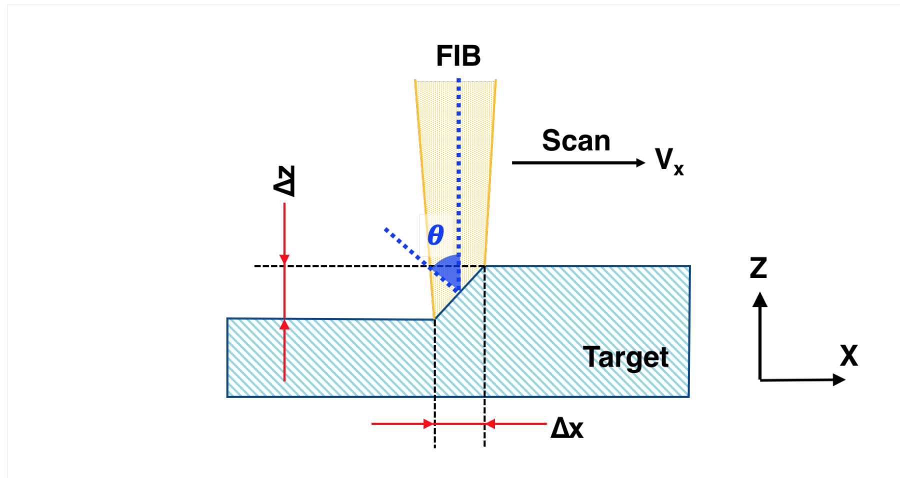


**Fig. 5.4** Schematic diagram of 1D FIB sputtered mode at steady state. The FIB forms an angle $\theta$ (angle of incidence) with sample surface.

The FIB sweep is followed by parallel X-axis, and the center of beam profile is moving with interval length, 10 nm of X-axis, 1.68 nm of Y-axis. The erosion shape was calculated by the sum of the rate of erosion. The Gaussian beam profile calculated from Eq (2) with having a beam diameter of 147 nm is shown in Fig. 5.5.

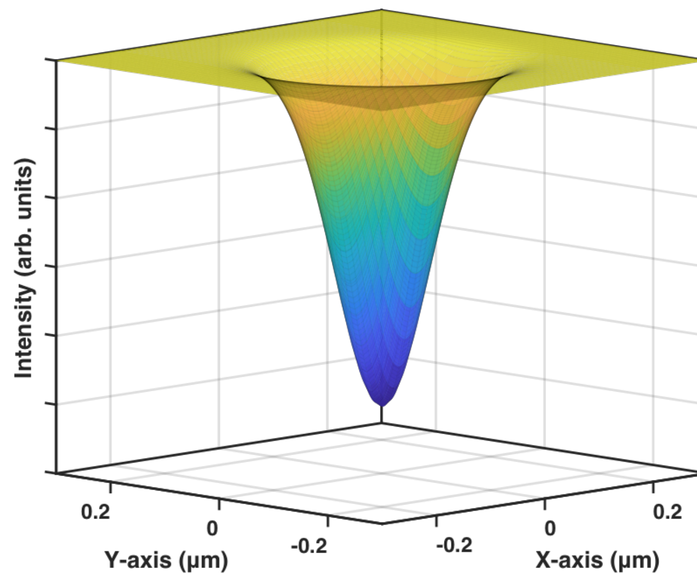


**Fig. 5.5** The gaussian beam profile.

In this simulation, the two kinds of sputtering yield were used for calculation of surface erosion. The angle of incidence is continually changed by the FIB scanning until they have a state-status of cross-sectional shape. However, I used only two sputtering yield values in this simulation because it was too complicated to apply all of the changed sputtering yields every time in the simulation. Sputtering yield for a value of 0º was applied when the cross section has an angle of incidence less than 80º, when over 80º of the angle of incidence, the sputtering yield has applied the value for 87º.

The sputtering yields were simulated by SDTrimSP code for 30 keV $Ga^+$ ions on Si and Ge at ion incidence angles (θ) of 0º and 87º. Figure 5.6 provides the sputtering yield of Si and Ge as a function of the angle of incidence. The sputtering yield of Ge is about two times larger than Si in the range 0 to 80 degrees, but over the degrees, there seems no difference in between Ge and Si. It is expected that at the beginning of the scan, the erosion depth between Ge and Si shows a difference, but when the after a start to be steady-state of shave-off scanning which having a high angle of incidence over the 80 degrees, the difference of them will decrease, and then eventually it will be shown the same erosion depth.

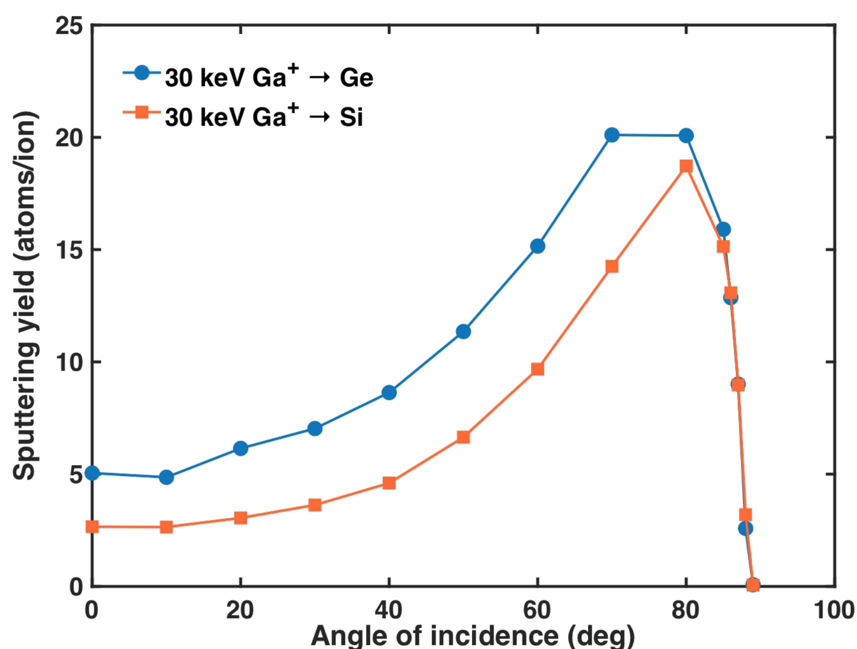


**Fig. 5.6** Dependence of sputtering yield on the angle of incidence of FIB for 30 keV $Ga^+$ ions beam irradiation on Ge (blue) and Si (orange).

### 5.3.2 Cross-sectional shape

The simulation was carried out by scanning once, 8, 14, 20 line scanning (step of Y-axis scanning) until the target will be removed 2, 4, and 6 μm of the depth, and 1015, 2202, and 2380 line scanning until the target will be removed about 2 μm and before/after 4 μm in Y-axis direction, respectively. Figure 5.7 shows the cross-sectional shapes after each step of Y-axis scanning. After twenty of line scanning, the 6 μm entire edge of the target was removed by the beam, and the cross-sectional shape did not change significantly until the entire target was completely removed by the beam. The sputtering yield at the value of 0 degree was applied to the target up to eight of line scanning. The erosion depth of Ge and Si showed about two times difference until that time, but then the difference gradually decreases by applying the sputtering yield at the value of 87 degrees.

From this simulation results, I could designate the sputtering position of P1 to P9 on each cross-sectional shape, and measure the angle of incidence at the point. The upper positions P1 and P2 of the target were determined by the trend line between the sample surface and the cross-sections of the sample. The angle of incidence of the sputtered particles and the positions at the point from P1 to P8 of the target in the cross-sectional shape after each sweep were summarized in Table 5.1.

The obtained sputtering position P (x,y,z) will be used for simulation of secondary ion trajectories in the SIMS optical transport system as starting position, and the angle of incidence will be used the input parameter for simulation of ion bombarding the target.

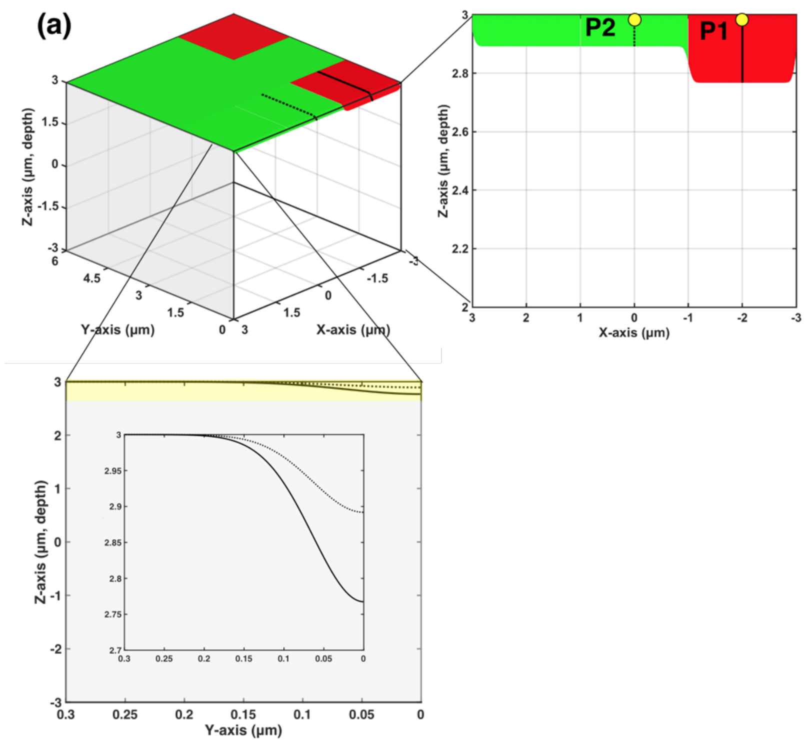


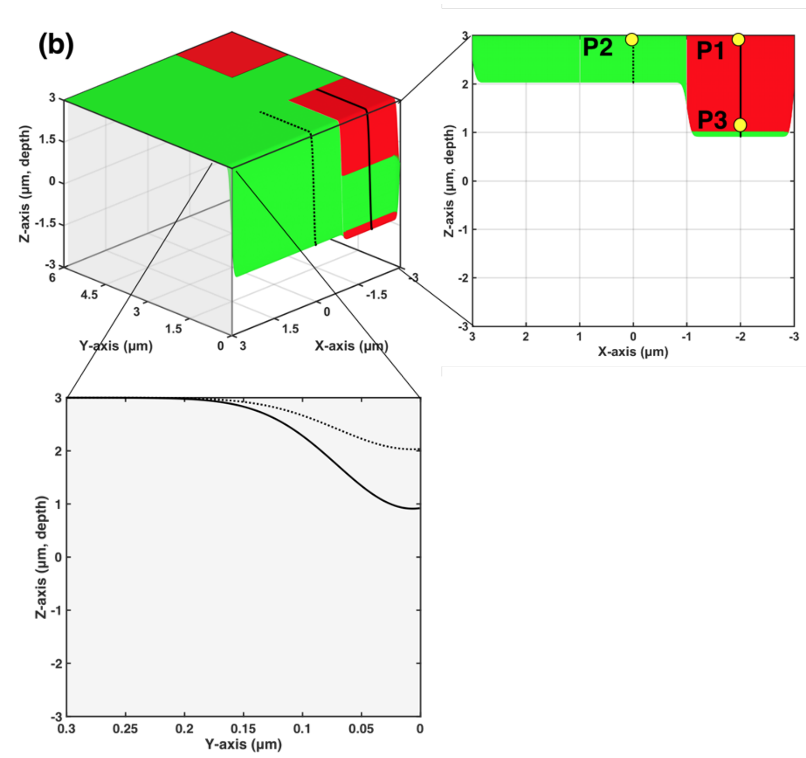


(continued)

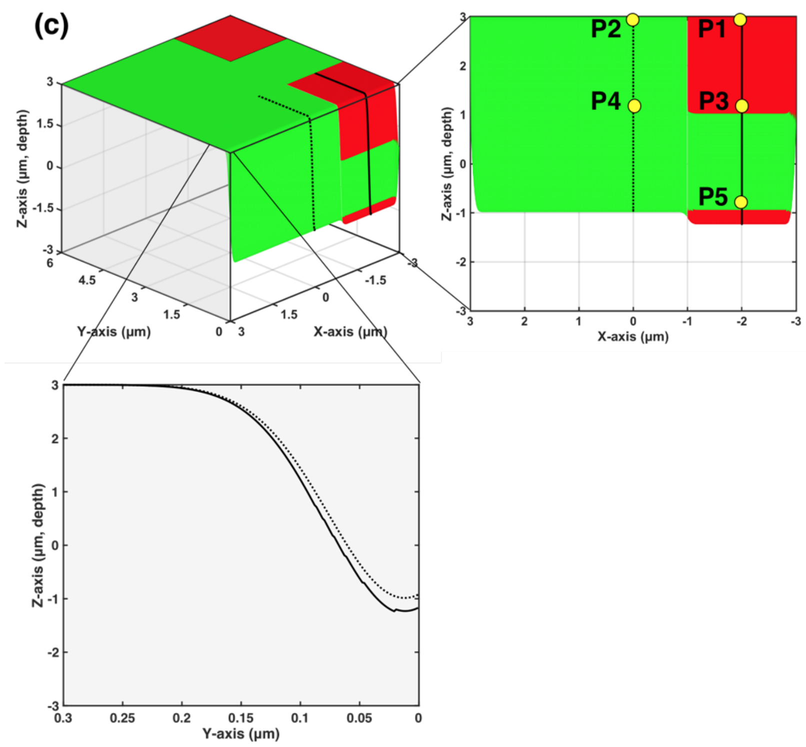


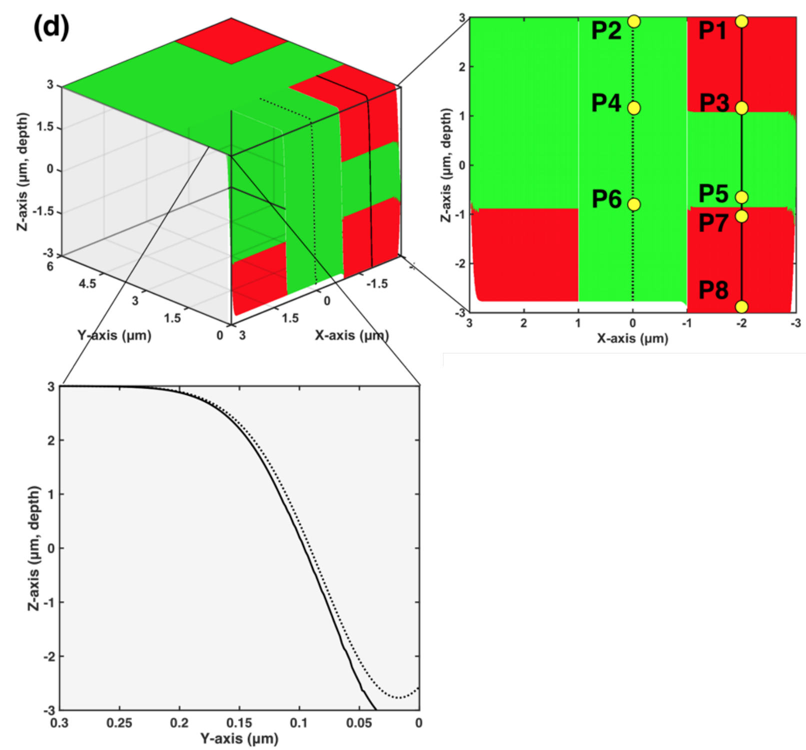


(continued)

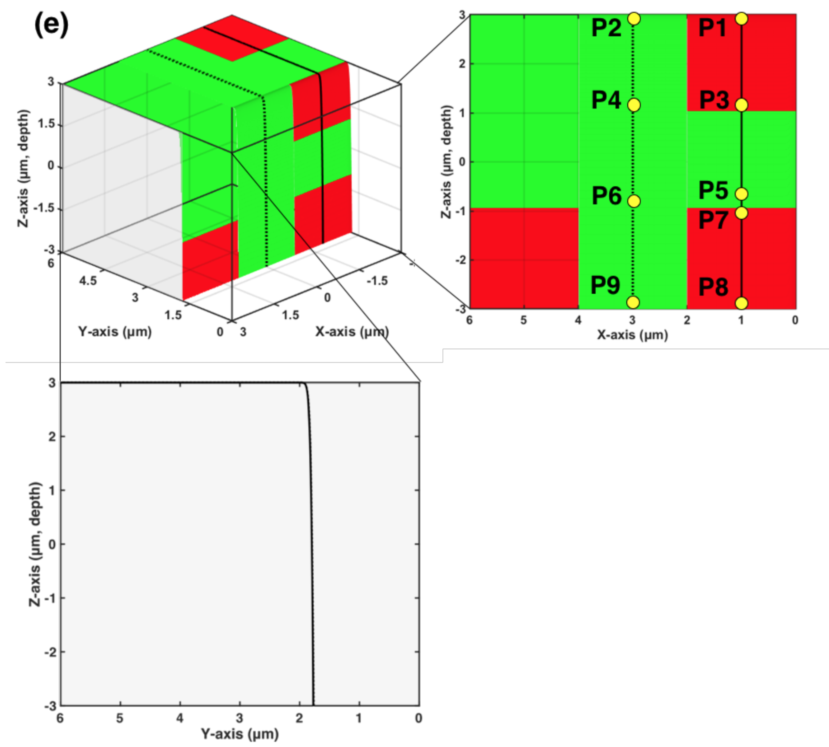


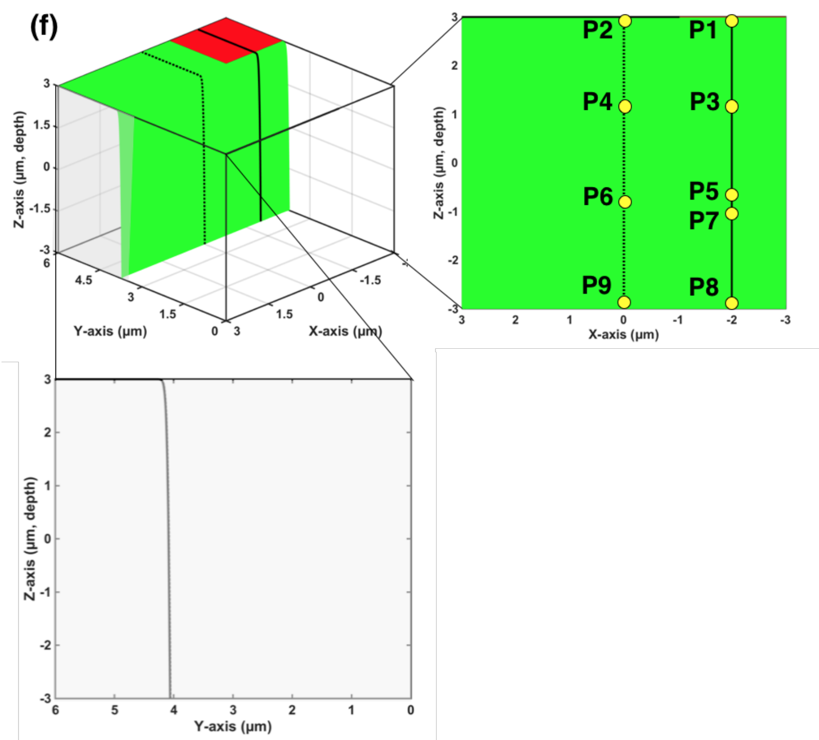


(continued)

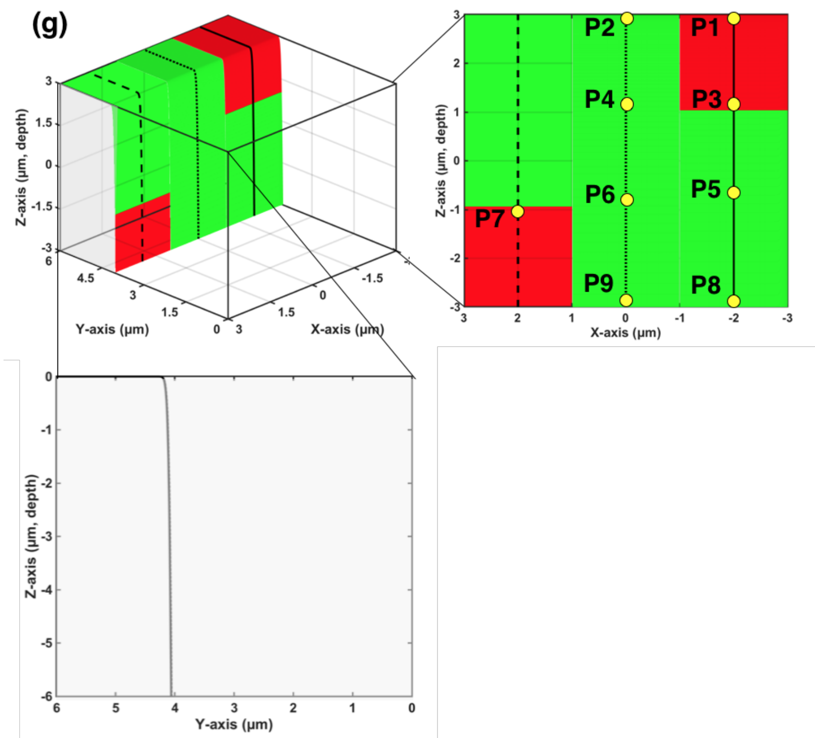


**Fig. 5.7** Cross-sectional shape of the target and sputtering positions. Each figure was measured after FIB line scanning at (a) once, (b) 8 times, (c) 14 times, (d) 20 times, (e) 1015 times, (f) 2202 times and (g) 2380 times. The inset graph in YZ-plane of (a) shows the large plot of the yellow part in the graph.

**Table 5.1** Summarized simulation results of the cross-sectional shape. (*P7 point of 2380 steps of Y-axis scanning is changed as shown in Fig. 5.7(g).)

| Steps of line scan | Point | Element | Sputtering Position, P (x,y,z) | | | Angle of incidence (°) |
|---|---|---|---|---|---|---|
| | | | x (μm) | y (μm) | z (μm) | |
| Once | P1 | Ge | -2 | 0.14 | 2.98 | 35.52 |
| | P2 | Si | 0 | 0.13 | 2.99 | 22.03 |
| 8 times | P1 | Ge | -2 | 0.18 | 2.95 | 64.13 |
| | P2 | Si | 0 | 0.17 | 2.97 | 56.31 |
| | P3 | Ge | -2 | 0.03 | 1 | 83.68 |
| 14 times | P1 | Ge | -2 | 0.20 | 2.94 | 70.84 |
| | P2 | Si | 0 | 0.20 | 2.94 | 70.36 |
| | P3 | Ge | -2 | 0.10 | 1.03 | 88.56 |
| | P4 | Si | 0 | 0.09 | 1.02 | 88.44 |
| | P5 | Si | -2 | 0.04 | -0.98 | 87.49 |
| 20 times | P1 | Ge | -2 | 0.21 | 2.93 | 73.03 |
| | P2 | Si | 0 | 0.21 | 2.94 | 72.09 |
| | P3 | Ge | -2 | 0.12 | 1.00 | 88.81 |
| | P4 | Si | 0 | 0.11 | 1.02 | 88.74 |
| | P5 | Si | -2 | 0.08 | -1.01 | 89.01 |
| | P6 | Si | 0 | 0.07 | -0.98 | 89.01 |
| | P7 | Ge | -2 | 0.08 | -1.05 | 89.01 |
| | P8 | Ge | -2 | 0.04 | -2.99 | 88.95 |
| 1015 times | P1 | Ge | -2 | 1.89 | 2.93 | 74.27 |
| | P2 | Si | 0 | 1.84 | 2.94 | 73.53 |
| | P3 | Ge | -2 | 1.81 | 1.09 | 89.10 |
| | P4 | Si | 0 | 1.81 | 1.02 | 89.10 |
| | P5 | Si | -2 | 1.78 | -0.87 | 89.47 |
| | P6 | Si | 0 | 1.78 | -0.92 | 89.46 |
| | P7 | Ge | -2 | 1.78 | -1.06 | 89.49 |
| | P8 | Ge | -2 | 1.77 | -2.99 | 89.61 |
| | P9 | Si | 0 | 1.76 | -2.97 | 89.59 |
| 2202 times | P1 | Si | -2 | 3.88 | 2.94 | 73.53 |
| | P2 | Si | 0 | 3.88 | 2.94 | 73.53 |
| | P3 | Si | -2 | 3.80 | 1.02 | 89.10 |
| | P4 | Si | 0 | 3.80 | 1.02 | 89.10 |
| | P5 | Si | -2 | 3.77 | -0.92 | 89.46 |
| | P6 | Si | 0 | 3.77 | -0.92 | 89.46 |
| | P7 | Si | -2 | 3.78 | -1.1 | 89.48 |
| | P8 | Si | -2 | 3.76 | -2.97 | 89.59 |
| | P9 | Si | 0 | 3.76 | -2.97 | 89.59 |
| 2380 times | P1 | Ge | -2 | 4.18 | -0.07 | 74.82 |
| | P2 | Si | 0 | 4.18 | -0.07 | 73.53 |
| | P3 | Ge | -2 | 4.10 | -1.91 | 89.10 |
| | P4 | Si | 0 | 4.10 | -1.98 | 89.10 |
| | P5 | Si | -2 | 4.08 | -3.92 | 89.46 |
| | P6 | Si | 0 | 4.08 | -3.92 | 89.46 |
| | P7* | Ge | 2 | 4.08 | -4.06 | 89.49 |
| | P8 | Si | -2 | 4.06 | -5.97 | 89.59 |
| | P9 | Si | 0 | 4.06 | -5.97 | 89.59 |

## 5.4. Monte Carlo simulation for sputtering process

Based on the angle of incidence at each position, the sputtering information, i.e., initial energy, the emission angles (azimuthal angles and elevation angle) of sputtered particles were obtained using SDTrimSP simulation code. The azimuthal angle and elevation angle which are angular conventions for the simulation of ion trajectories (SIMION program) was illustrated in Fig. 5.8. The sputtered particles are generated from 30 keV $Ga^{+}$ ions of $10^{7}$ irradiation on Ge and Si at each angle of incidence, the maximum of $2 \times 10^{5}$ particles were obtained. Among the all sputtered particles, the particle which having the energies less than 10 eV were extracted and assumed to the secondary ions in this simulation.

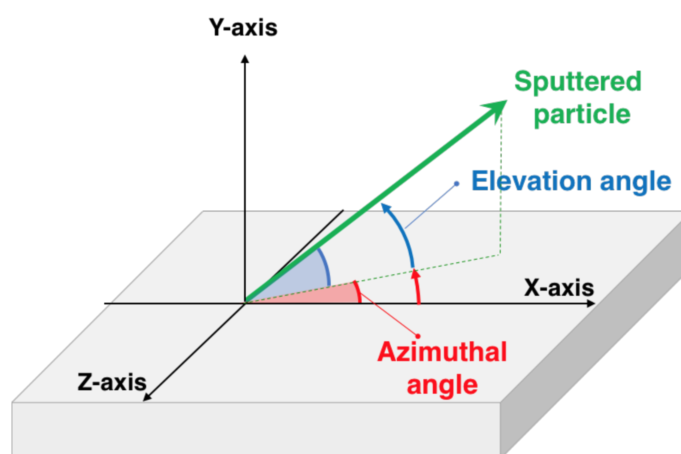


**Fig. 5.8** Illustration of azimuthal angle and elevation angle in SIMION coordinate system.

## 5.5. Simulation of secondary ion trajectories

### 5.5.1 Position on the mass detector of the secondary ions

The sputtered particles which having energy less than 10 eV obtained from the previous SDTrimSP simulation results had been assumed to be secondary ions, and I conducted the simulation of ion trajectories in the 3D shave-off SIMS using SIMION program. Figure 5.8 shows the positions on the mass detector of the secondary ions sputtered from at each point (P1-P8) after 1, 8, 14, and 20 line scanning. The Mattuach-Herzog type mass

analyzer has a feature of the plane focusing characteristics with the dispersion proportional to $m^{1/2}$ along the focal plane (X-axis) multianode detector [5.14], therefore each element of secondary ions, Ge, Si, was detected on the X-axis of the multichannel mass detector corresponding to the mass-to-charge ratio (m/z) of Ge (m/z 72.64) and Si (m/z 28.03) respectively. The same element ions were distributed along the Z-axis based on the m/z of the detector.

In SIMS apparatus, the secondary ions were obtained as data in intensity from the Z-axis of the mass detector. The dotted lines in Fig. 5.9 shows the intensity to the number of the secondary ions within the detected range. This simulation result shows that the peak of the intensity distribution was clearly distinguished by the sputtered depth position of the target as shown in Fig. 5.9. The maximum peak and the range of the secondary ion distribution on the detector are summarized in Table 5.2.

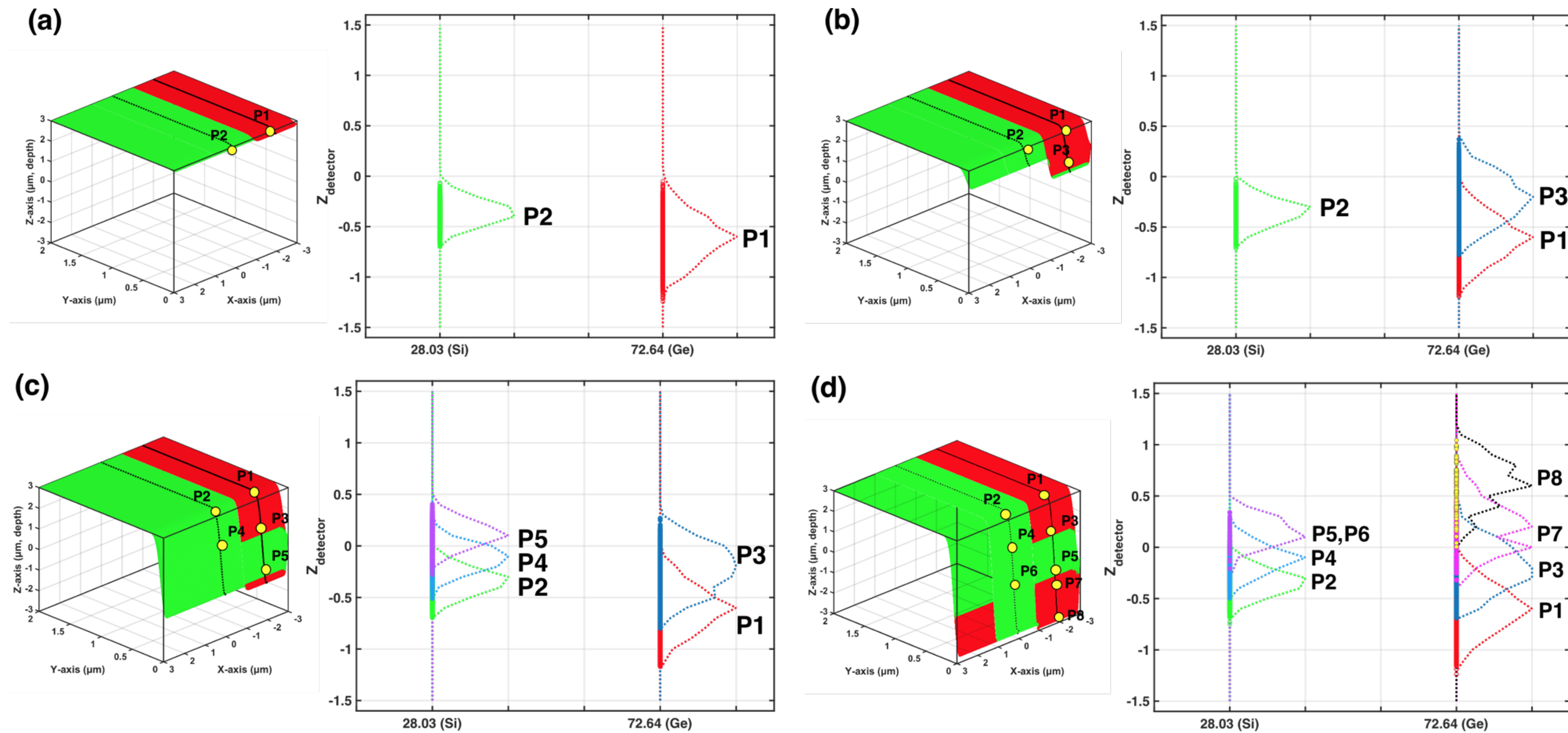


**Fig. 5.9** Position on the detector of secondary ions sputtered from each point (P1-P8). Each figure was measured after FIB line scanning at (a) once, (b) 8 times, (c) 14 times, and (d) 20 times. The dotted line is normalized intensity distribution of the secondary ions along the Z-axis.

**Table 5.2** Summarized simulation results of the secondary ions.

| Steps of line scan | Point | Element | Sputtering Position, P (x,y,z) | | | Angle of incidence (°) | Position on detector ($Z_{detector}$) | | | Peak of distribution (mm) |
|---|---|---|---|---|---|---|---|---|---|---|
| | | | x (μm) | y (μm) | z (μm) | | Max (mm) | Min (mm) | Difference | |
| Once | P1 | Ge | -2 | 0.14 | 2.98 | 35.52 | -0.05 | -1.24 | 1.19 | -0.6 |
| | P2 | Si | 0 | 0.13 | 2.99 | 22.03 | -0.07 | -0.70 | 0.63 | -0.4 |
| 8 times | P1 | Ge | -2 | 0.18 | 2.95 | 64.13 | -0.09 | -1.19 | 1.10 | -0.6 |
| | P2 | Si | 0 | 0.17 | 2.97 | 56.31 | -0.02 | -0.71 | 0.69 | -0.3 |
| | P3 | Ge | -2 | 0.03 | 1 | 83.68 | 0.37 | -0.78 | 1.15 | -0.2 |
| 14 times | P1 | Ge | -2 | 0.20 | 2.94 | 70.84 | -0.03 | -1.17 | 1.14 | -0.6 |
| | P2 | Si | 0 | 0.20 | 2.94 | 70.36 | -0.05 | -0.70 | 0.65 | -0.3 |
| | P3 | Ge | -2 | 0.10 | 1.03 | 88.56 | 0.27 | -0.80 | 1.07 | -0.2 |
| | P4 | Si | 0 | 0.09 | 1.02 | 88.44 | 0.19 | -0.51 | 0.70 | -0.1 |
| | P5 | Si | -2 | 0.04 | -0.98 | 87.49 | 0.41 | -0.28 | 0.69 | 0.1 |
| 20 times | P1 | Ge | -2 | 0.21 | 2.93 | 73.03 | 0.03 | -1.24 | 1.27 | -0.6 |
| | P2 | Si | 0 | 0.21 | 2.94 | 72.09 | -0.02 | -0.75 | 0.73 | -0.3 |
| | P3 | Ge | -2 | 0.12 | 1.00 | 88.81 | 0.38 | -0.69 | 1.07 | -0.2 |
| | P4 | Si | 0 | 0.11 | 1.02 | 88.74 | 0.19 | -0.50 | 0.69 | -0.1 |
| | P5 | Si | -2 | 0.08 | -1.01 | 89.01 | 0.34 | -0.21 | 0.55 | 0.1 |
| | P6 | Si | 0 | 0.07 | -0.98 | 89.01 | 0.34 | -0.21 | 0.55 | 0.1 |
| | P7 | Ge | -2 | 0.08 | -1.05 | 89.01 | 0.72 | -0.32 | 1.04 | 0, 0.2 |
| | P8 | Ge | -2 | 0.04 | -2.99 | 88.95 | 1.04 | 0.00 | 1.04 | 0.6 |

The position on the detector of the secondary ions showed the opposite direction to the sample. The secondary ions sputtered from the upper side of the target (P1, P2) were detected at the bottom of the detector (negative value of Z-axis), and the ions sputtered from the bottom of the sample (P5, P6, P7) appeared at the upper part of the detector. This opposite direction was caused by the electric field effects inside of the 3D shave-off SIMS system.

In addition, the two elements showed a difference in the length of the distribution on the detector. The distribution of the secondary Ge ions in the detector was about 1 mm, and the Si ions were distributed in the length of 0.7 mm. Ge had wide distribution length than Si, and it is due to the difference of flight path length of the elements in the mass analyzer. The Ge, which has high mass weight than Si, has larger magnification due to longer flight path than Si as shown in Fig. 5.3.

Figure 5.10 presents comparison the positions on the detector of secondary ions of Ge (a) and Si (b) according to the depth of the sputtering position after 20 line scanning. The secondary ions of Ge were sputtered from the position of P1, P3, P7 and P8 which are positioned at 0, 2, 4, 6 μm from the target surface, respectively. The Si ions were sputtered from the position of P2, P4, P6 which are positioned at 0, 2, 4, μm from the target. I compared the detection positions of the secondary ions from the peak of the intensity distribution. When the sputtering position of the secondary ions decreases by the 2 μm from the target surface, the peak position of the distribution on the detector was increased to 400 μm for Ge, and 200 μm for Si (Magnification ratio : $2\times10^2$ (Ge), $1\times10^2$ (Si)).

This result is summarized that when the sample was eroded by the 1 μm by the beam, the position on the detector of the secondary ions changed about 0.2 mm for Ge, and about 0.1 mm for Si, and we can distinguish the sample locational information.

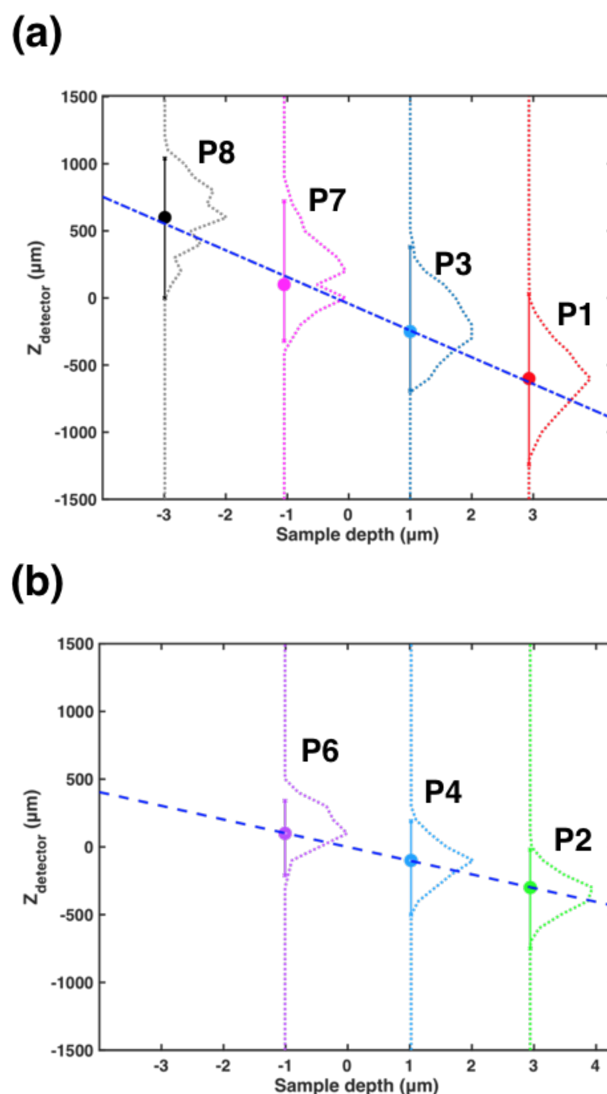


**Fig. 5.10** Sputtering position in depth of the sample versus position on the detector ($Z_{detector}$) of the secondary ions. (a) Ge ions distribution sputtered from at position of P1/P3/P7/P8 in a target. (b) Si ions distribution sputtered from at position of P2/P4/P5,6. The blue dash line is the least squares fitting of each distribution peak.

### 5.5.2. Improvement resolution of secondary ion distribution

The depth of the sputter position distinguished the distribution peak of secondary ions on the detector, but it showed broad distribution at all of the results. In order to improve resolution of distribution of the secondary ions, I have investigated the secondary ions with their initial energy and emission angles (azimuthal angle and elevation angle) as a function of their detected position as shown in Fig. 5.11.

**(a)**

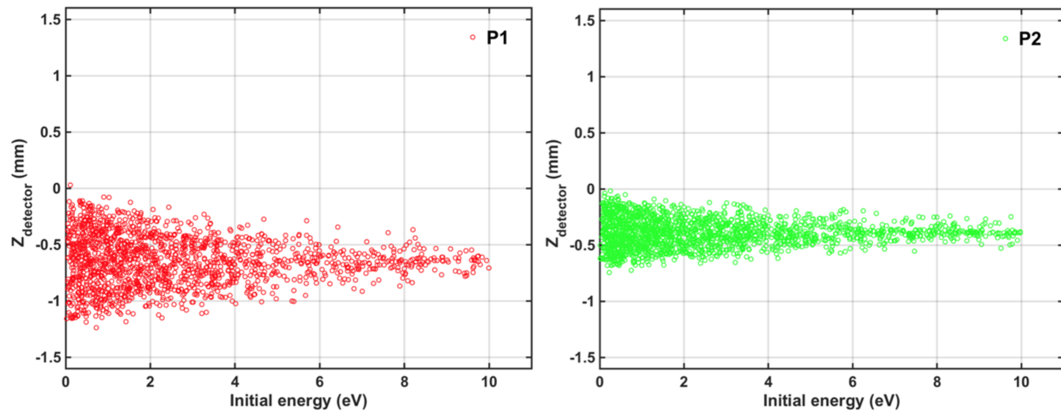


**(b)**

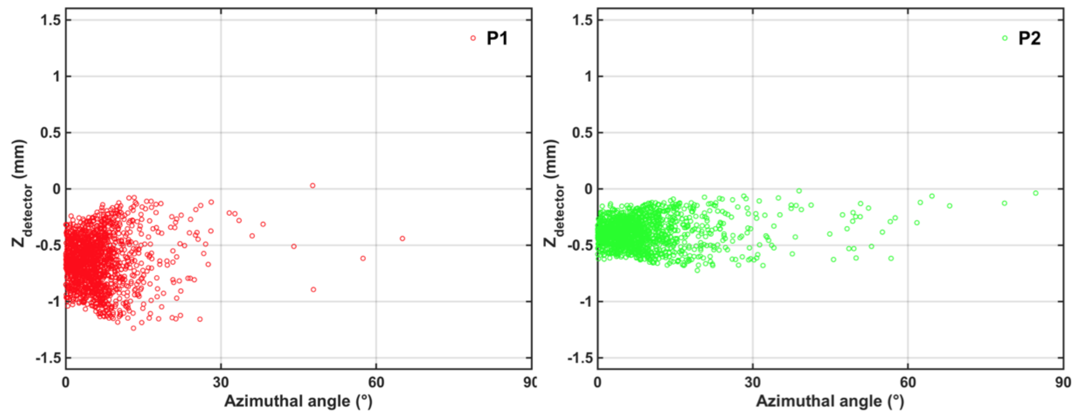


**(c)**

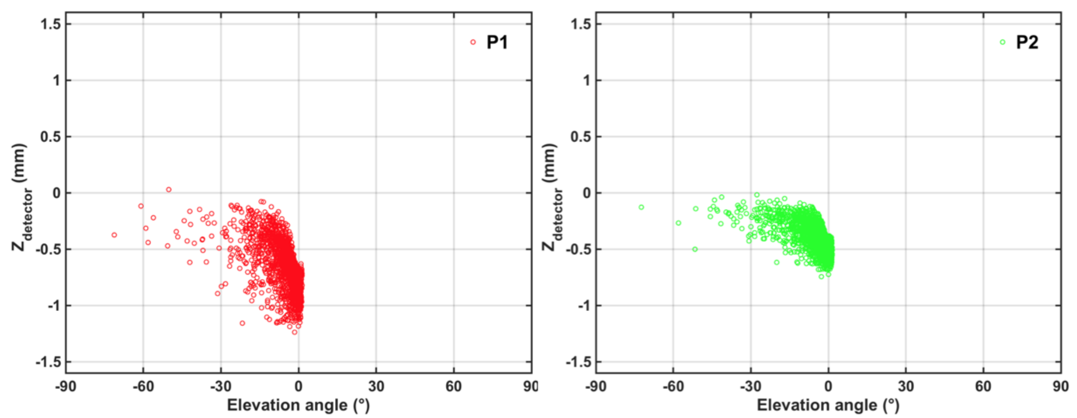


**Fig. 5.11** Position on the detector ($Z_{detector}$) of the secondary ions sputtered from P1 (Ge, red) and P2 (Si, green) as a function of (a) initial energy. (b) azimuthal angle, and (c) elevation angle.

The secondary ions which detected on the mass detector showed similar results in energy and emission angles regardless of the element. In Fig. 5.11(a), the width of the distribution of the secondary ions in the detector decreased with increasing energy, and the distribution width did not change with azimuthal angle or elevation angle (Figs. 5.11 (b) and 5.11(c)). Therefore I have implemented the simulation of ion trajectories with the particles which having 5 eV to 10 eV. Figure 5.12 shows the before and after changing the range of initial energy of the secondary ions generated from the 20 times line scanning. When the range of initial energy change from 0-10 eV (Fig. 5.12(a)) to 5-10 eV (Fig. 5.12(b)), the width of secondary ions distribution on the detector narrowed with maintaining the position of distribution peak. Table 5.3 summarized the secondary ions distribution on the detector of Fig. 5.12 curves with the length, a full width a half maximum (FWHM) and peak position.

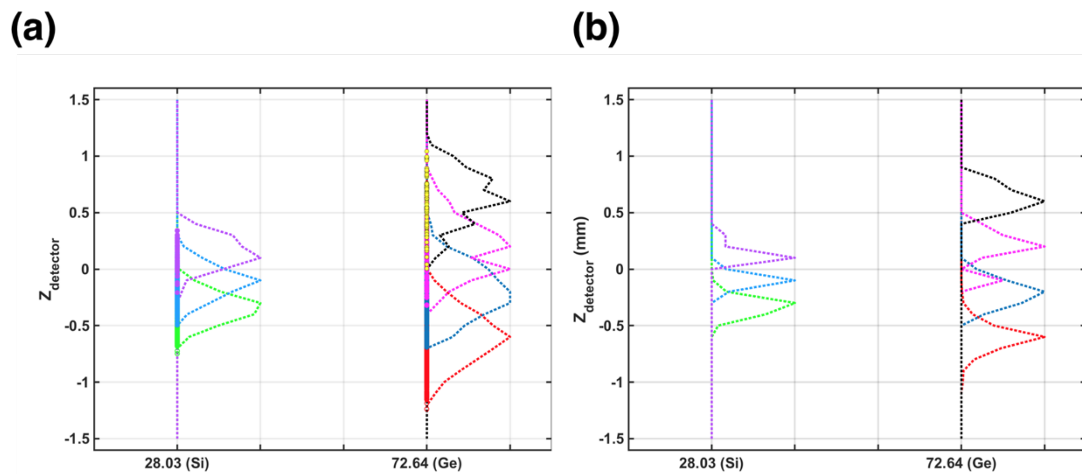


**Fig. 5.12** Position on the detector ($Z_{detector}$) of the secondary ions sputtered by 20 times line scanning. (a) The initial energy range of secondary ions is 0 to 10eV. (b) The initial energy range of secondary ions is 5 to 10eV.

**Table 5.3 Position of secondary ions on the detector and** full width a half maximum (FWHM) and peak position of secondary ion distribution. (a) The initial energy range of secondary ions is 0 to 10eV. (b) The initial energy range of secondary ions is 5 to 10eV.

| Line scan | Point | Element | (a) Range of initial energy (0-10eV) | | | | | (b) Range of initial energy (5-10eV) | | | | |
|---|---|---|---|---|---|---|---|---|---|---|---|---|
| | | | Max | Min | Length (l) | Resolution (R, μm ) | Peak of distribution | Max | Min | Length (l) | Resolution (R, μm) | Peak of distribution |
| | P1 | Ge | 0.03 | -1.24 | 1.27 | 6.35 | -0.6 mm | -0.29 | -1.00 | -0.72 | 3.58 | -0.6 mm |
| | P2 | Si | -0.02 | -0.75 | 0.73 | 7.30 | -0.3 mm | -0.19 | -0.57 | -0.38 | 3.85 | -0.3 mm |
| | P3 | Ge | 0.38 | -0.69 | 1.07 | 5.35 | -0.2 mm | -0.06 | -0.46 | -0.40 | 1.98 | -0.2 mm |
| 20 | P4 | Si | 0.19 | -0.50 | 0.69 | 6.90 | -0.1 mm | -0.01 | -0.27 | -0.25 | 2.52 | -0.1 mm |
| times | P5 | Si | 0.34 | -0.21 | 0.55 | 5.50 | 0.1 mm | 0.23 | 0.01 | -0.22 | 2.19 | 0.1 mm |
| | P6 | Si | 0.34 | -0.21 | 0.55 | 5.50 | 0.1 mm | 0.23 | 0.01 | -0.22 | 2.19 | 0.1 mm |
| | P7 | Ge | 0.72 | -0.32 | 1.04 | 5.20 | 0.2 mm | 0.35 | -0.12 | -0.47 | 2.36 | 0.2 mm |
| | P8 | Ge | 1.04 | 0.00 | 1.04 | 5.20 | 0.6 mm | 0.75 | 0.41 | -0.35 | 1.74 | 0.6 mm |

When the range of initial energy was changed to 5-10 eV, all peak of distribution was not changed, and the length of the secondary ions distribution become two times narrower. The Z-axis positional resolution (R) was calculated by Eq. 5–3,

$$R = \frac{l}{|M|} \quad (5-3)$$

where, $l$ is the length of secondary ion distribution on the detector (μm) and $M$ is magnification ratio ($2\times10^2$ (Ge), $1\times10^2$ (Si)). The average Z-axis positional resolution after changing the range of initial energy (5-10eV) was 2.4 μm for Ge and 2.8 μm for Si. It was to improve about 44% (5.5 μm for Ge) and 45 % (6.3. μm for Si) less than the average Z-axis positional resolution before changing the range of initial energy (0-10eV). It demonstrated to improve the resolution of secondary ions on the detector in existing lens system.

## 5.6. Conclusion

In this chapter, I simulated the secondary ions from the sputtering process by the FIB to detection position on the mass detector along the optics system of our 3D shave-off SIMS apparatus. With a virtual target consisting of two elements (Ge, Si), three-step simulation showed the surface erosion process of the target, the sputtering process of the particles, and the secondary ion trajectories in optical transport system under the shave-off conditions. To compare the position of the secondary ions on the mass detector for the sputtered position in the sample, I designated the nine-point position (P1-P9) in the target, the particles which sputtered from the point were investigated.

In the first step (simulation of surface erosion), the cross-sectional shape of the target eroded by the 30keV $Ga^+$ ions beam with shave-off scanning was observed in accordance with steps (1, 8, 14, and 20 steps) of line scanning. Each step is the number of line scanning to remove the sample depth as 2, 4, 6 μm in the first layer. An edge of the 6 μm target was completely removed by the beam after 20 line scanning. From each step, I could measure the angle of incidence and obtain the position (P1-P9) of sputtered particles.

In the second step, information of the sputtered particle such as initial energy and emission angles was obtained by simulation of SDTrimSP. Based on the incident angle obtained in the first step, $10^7$ $Ga^+$ ions were irradiated to the target, and the maximum 2 × $10^5$ sputtered particles were extracted and investigated for simulation. The sputtered particles which only having the energy under 10 eV were assumed as secondary ions, and its trajectories were simulated in the 3D shave-off SIMS system by using SIMION program.

The secondary ions which sputtered from a different depth of the target showed a different distribution of detection position on the mass detector. The sputtering position along the sample depth is clearly distinguished on the mass detector by the peak of the secondary ion intensity distribution. The secondary ions of Ge which sputtered with a difference in depth of the target about 2 μm showed a different Z-axis position on the detector about 0.4 mm, and the secondary ions of Si showed 0.2 mm of difference on the detector.

The secondary ion distribution of the detector was similar to the secondary ion energy distribution. In the initial energy range of 0-10 eV, the secondary ions showed a narrow distribution with increasing initial energy. Therefore I had calculated again with the initial energy range of the secondary ion to 5-10 eV, and the average Z-axis positional resolution was about 45% narrowed with maintaining the peak position of the distribution as a result.

The results obtained from the three-steps simulations based on the FIB scanning showed the possibility to distinguish about the secondary ions of the sample along depth direction (Z-axis). This simulation is the first step for evaluation of our 3D shave-off SIMS concept. Based on these simulations, the other elements also will be able to perform in the system, and the lens system and the ions transport system will be able to optimized to develop for 3D shave-off SIMS.

## 5.7 References


5.1 Y. Takagi, S. Kang, K. Matsumura, T. Azuma, B. Tomiyasu and M. Owari, *e-Journal Surf. Sci. Nanotechnol.*, 2018, **16**, 324–328.

5.2. K. Matusmura, S. Kang, T. Azuma, B. Tomiyasu and M. Owari, Journal of Surface Analysis, [submitted]

5.3 G. Carter, M. J. Nobes, K. I. Arshak, R. P. Webb, D. Evanson, B. D. L. Eghawary and J. H. Williamson, *J. Mater. Sci.*, 1979, **14**, 728–736.

5.4 I. V. Katardjiev, *J. Vac. Sci. Technol. A Vacuum, Surfaces, Film.*, 1994, **12**, 61–68.

5.5 I. V. Katardjiev, *J. Vac. Sci. Technol. A Vacuum, Surfaces, Film.*, 1988, **6**, 2434–2442.

5.6 T. Ishitani, K. Umemura, T. Ohnishi, T. Yaguchi and T. Kamino, *J. Electron Microsc.*, 2004, **53**, 443–449.

5.7 T. Ishitani, *J. Vac. Sci. Technol. B Microelectron. Nanom. Struct.*, 1998, **16**, 1907–1913.

5.8 H.-B. Kim, G. Hobler, A. Steiger, A. Lugstein and E. Bertagnolli, *Nanotechnology*, 2007, **18**, 245–303.

5.9 T. Ishitani, *J. Vac. Sci. Technol. A Vacuum, Surfaces, Film.*, 1991, **9**, 3084–3089.

5.10 D. Santamore, K. Edinger, J. H. Orloff and J. Melngailis, *J. Vac. Sci. Technol. B Microelectron. Nanom. Struct.*, 1997, **15**, 2346–2349.

5.11 T. Ishitani and T. Ohnishi, *Jpn. J. Appl. Phys.*, 1989, **28**, L320–L322.

5.12 F. Itoh, A. Shimase and S. Haraichi, *J Electrochem Soc*, 1990, **137**, 983–988.

5.13 A. Latif, *"Nanofabrication Using Focused Ion and Electron Beams,"* Darwin Coll. Cambridge, 2000, Chapter 10.

5.14 Y. Nihei, H. Satoh, S. Tatsuzawa, M. Owari, M. Ataka, R. Aihara, K. Azuma and Y. Kammei, *J. Vac. Sci. Technol. A Vacuum, Surfaces, Film.*, 1987, **5**, 1254–1257.

# CHAPTER VI

# CONCLUSION

## 6.1. Conclusion

In this study, I have investigated the several basic parameters of sputtered particles generated by the primary ion beam which required for the development of 3D shave-off SIMS. Before introducing the lens system which magnifies the z-axis of secondary ions in 3D shave-off SIMS, it is necessary to understand and obtain the aspect of the sputtering process. Therefore, I had examined the relationship between the primary ion beam and sputtered sample, and evaluate the emitted particles that will be a basis of the ion transport trajectory in the lens system. In the shave-off scanning, the cross-sectional shape is an important factor in the shave-off method related to an angle of incidence due to the unique scanning method which always scans the edge of the sample. I had investigated the angle of incidence of the focused ion beam by observing the cross-sectional shape after shave-off scanning. The cross-sectional shape had been changed depending on the scan speed of primary ion beam, and it also affected to the sputtering yield and the angle of incidence: the faster the scan speed, the higher the sputtering yield. It is mean that the scan speed in the shave-off method will be a fine control method for increasing the sputtering yield and control the emission angle of sputtered particles.

In the 3D shave-off SIMS, the emission angle of secondary ions is a key parameter to decide the sample depth locational information on to the mass detector. The emission angle of the sample and energy had been investigated as angular distribution of sputtered particles. It could conduct a simulation using SDTrimSP which is one of Monte Carlo binary collision approximation simulation programs. The program had good agreement with experimental data even it had been performed with a shave-off condition conducted

the high energy of the primary ion beam and high angle of incidence. From this result, we had known that the direction of the sputtered particles by the FIB shave-off scanning. The particles which have high energies such as neutral and scattered incidence particle showed downward in the direction of incidence beam, and the particles having low energy had a direction of perpendicular of the sample surface. The sputtered particles by the shave-off FIB scanning have different emission directions depending on the energy, and it could expect that the low energy particles such as ions are emitted in the vertical direction from the cross sections so that the secondary ions will more easily. These investigated various parameters, cross-sectional shape related to the angle of incidence, energy, and angle of sputtered particles, had been applied to a virtual sample which composed two elements (Ge, Si). The simulation had implemented for whether the secondary ions can be distinguished by the depth of the sample at the detector.

The sputtered particles of each element sputtered by 30keV gallium ion beam on the virtual target had been calculated through three-step simulations. This results had shown the possibility of the concept of 3D shave-off SIMS. The secondary ions generated by the ion beam scanning with shave-off method had been distinguished in the lateral direction of the mass detector according to the sputtering position in the depth of the sample. It had expected that our designed cylindrical lens of 3D shave-off SIMS can succeed magnify only the depth information of the secondary ions, and the mass data of the target is expected to obtain the sample depth locational information simultaneously.

This realization of 3D shave-off SIMS implies that we can obtain the high resolution three-dimensional SIMS data with fine focused ion beam at a short time. I expect to complete the fabrication and assemble the magnification lens system from this study.

### 6.2. Summary

In Chapter I, I had discussed the necessity of three-dimensional analysis for the micro-materials, and the suitability of shave-off SIMS through the comparison with other 3D analysis techniques and surface analysis technique. Besides, the basic principles and the composition of the SIMS apparatus, and the shave-off method have been described. In this study, I had investigated the information of sputtered particles for development and instrumentation of 3D shave-off method which is enabled to obtain the sample depth locational information at the lateral axis of the mass detector.

In Chapter II, I could measure the angle of incidence by observing the cross-sectional shape after the shave off scanning. The angle of incidence in shave-off is an important factor which regards with an emission angle of sputtered particles. To verify the effect of the primary ion beam to the sputtered particles, the shave-off scans had been performed on samples with three different depths under the same conditions, and the cross-sectional shapes of the samples had been compared. As a result, the sample had shown the same slope of 87 degrees up to 10 μm in depth, but the lower part had shown different results. It had been demonstrated through simulations that this is the result of incident ions as well as scattered incident ions and sputter particles with heavy energy. In this study, it had been found that the incidence angle of incident ions in tungsten of 30keV gallium ion was about 87 degrees, and the direction of particles generated by ion bombardment could also be predicted.

In Chapter III, the angle of incidence had been investigated according to the scan speed by observing the cross-sectional shape. The scan speed of the primary ion beam could change the cross-sectional shape, it affected the angle of incidence and the sputtering yield. The angle of incidence had been measured by observing the cross-sectional shape, and the sputtering yield could calculate from surface erosion equation with the incident angle. The cross-sectional shape of the tungsten sample had been compared with three different scan speed. The slope of the cross sections increased with decreasing scan speed, and the sputtering yield decreases with decreasing scan speed and with increasing the angle of incidence. In addition, I could assume the beam profile from the results. The cross sections had different shapes as a function of scan speed, but the normalized derivative graphs had shown as one composite graph. It could be estimated as an apparent beam size of 147 nm.

In Chapter IV, the angular distribution and energy distribution of sputtered particles had been simulated using SDTrimSP. The emission angle and initial energy are essential parameters for the development of three-dimensional (3D) shave-off SIMS directly related to the detection position. Through comparison of the existing shave-off experiment, the simulation results of SDTrimSP for the angular, energy distribution of sputtered particles had shown good agreement under shave-off scan conditions. The simulation had been performed for the 30 keV $Ga^+$ ions irradiation on the tungsten sample. The sputtered W particles had been investigated with several angles of incidence. It had clear difference behaviors by the angle of incidence, the angular distribution had a

direction about emission angle of 15° at a high angle of incidence (87°), and the polar angle had distinguished the energy distribution of the sputtered particles.

In Chapter V, I had simulated the position on our parallel multianode mass detector of the secondary ions sputtered from a virtual sample which composed the germanium and silicon. The simulation had been implemented with three steps, from sample surface erosion process to secondary ion trajectories in the 3D shave-off SIMS apparatus.
To compare the position on the detector of secondary ions depending on the sputtering depth position the target, I had decided the nine points on the sample and had investigated the secondary ions sputtered from the point. Each secondary ions sputtered at different depths of the target had different distributions of detection positions on the mass detector. The sputtering position depending on the sample depth had been clearly distinguished on the mass detector by the peak of the secondary ion intensity distribution. The secondary ions of Ge and Si sputtered from the target with a depth of about 2 μm difference had shown at different Z-axis positions of about 0.4 mm and 0.2 mm on the mass detector, and the Z-axis positional resolution was 5.5 μm for Ge and 6.3. μm for Si, respectively. This resolution was able to be improved by adjusting the range of secondary ion initial energy. When decreasing the range of initial energy, the Z-axis positional resolution of secondary ions of Ge and Si were decreased as 2.4 μm and 2.8 μm which are improved by about 45%.

# Appendix

Matlab code to simulate the cross-section shape.

```
% Gaussian_ ymove.m
clear;

%% Step 0) Input parameter

BC = 2.6e-10; % beam current (A)
Br = 0.040; % beam diameter (um)
D0 = 0.002; % dwell time (sec/dot)
dens = 63000000000; % density (atoms/um3)
sy = 2.37;% sputtering yield
Ix = 0.01; % X interval length (um)
Iy = 0.00168; % Y interval length(um)
Bl = 0.3; % beam length arrange (um, -Bl : Bl)
Sx = 5; % Sample X length (um, sample size Sx*Sy um^2)
Sy = 6.7; % Sample Y length (um, sample size Sx*Sy um^2)

%% Step 1) beam profile (one spot, figure 1)

X = -Bl:Ix:Bl; % beam profile X-axis
Y = -Bl:Iy:Bl; % beam profile Y-axis
X1dot = length (X);
Y1dot = length (Y);
K = eye(Y1dot,X1dot); % eye(#1.Ydot,#1.Xdot)
Th2=(Br./2.354820045).^2; %theta^2 Br/((8*LN(2))^0.5)
A0=BC./(2.*pi().*Th2);

for i = 1:Y1dot % 1.Ydot
    for j = 1:X1dot % 1.Xdot
        K(i,j)= -A0.*exp((-(X(1,j).^2+Y(1,i).^2)./(2.*Th2)));
        K(i,j)=K(i,j)./96485.*6.02.*10^23.*D0./dens.*sy;
    end
end

figure(1)
[A1,B1]=meshgrid(X,Y);
mesh(A1,B1,K);

%% Step 2) beam move to X-axis (1-sweep, figure 2)

X2 = -Bl*2:Ix:Sx+Bl*2; % beam total X move %*2
X2dot = length(X2)-X1dot;
K1=K; % k = i*j
E=zeros(Y1dot,1); % #1.Ydot

for n=2:X2dot+1 % n=(2:#2.Xdot+1)
   if n==2 % first
      K_n=[E,K1]+[K1,E];
   else
      E_n=zeros(Y1dot,n-1); % e=2*n+1
      K_n=[E_n,K1]+[K_n,E];
```

```
  end
end

figure(2)
[A2,B2]=meshgrid(X2,Y);
mesh(A2,B2,K_n);

%% Step 3) beam move to Y-axis (after shave-off, figure 3)

Y2 = -Bl*2:Iy:Sy; % beam total Y 1move
Y2dot = length(Y2)-Y1dot;

Ey=zeros(1,X2dot+X1dot); % e (#2.Ydot + #1.Xdot)
K_M= K_n;

for m=2:Y2dot+1
    if m==2
        K_M=[K_n;Ey]+[Ey;K_n];
    else
        Ey_m=zeros(m-1,X2dot+X1dot);
        K_M=[K_M;Ey]+[Ey_m;K_n];
    end
end

figure(3)

[A3,B3]=meshgrid(X2,Y2);
mesh(A3,B3,K_M);
```

## Publications

1. **S. Kang**, K. Matsumura, T. Azuma, B. Tomiyasu and M. Owari, "Angular distribution of sputtered particles in shave-off section processing", Journal of Surface Analysis, The Surface Analysis Society of Japan [Accepted]

2. **S. Kang**, Y. Kim, B. Tomiyasu and M. Owari, "Influence of the Shave-off Scan Speed on the Cross-Sectional Shape", The Japan Society of Vacuum and Surface Science, e-J. Surf. Sci. Nanotech., 2018, **16**, 214-217.

3. **S. Kang**, M. Furushima, H. Asakura, A. Habib, Y. Kim, B. Tomiyasu and M. Owari, Analysis of the shape of cross sections developed under shave-off condition sputtering, Journal of Surface Analysis, The Surface Analysis Society of Japan, 2017, 24, **2**, 164-166.

## International / Domestic Conferences

1. **S. Kang**, K. Matsumura, T. Azuma, B. Tomiyasu and M. Owari, "Angular distribution of sputtered particles in shave-off section processing", Symposium on Practical Surface Analysis 2018 (PSA-18), Shizuoka, Japan, October 15-16, 2018.

2. **S. Kang**, Y. Kim, B. Tomiyasu and M. Owari, 20st international conference on secondary ion mass spectrometry (SIMS 21), "Influence of the Shave-off Scan Speed on the Cross-Sectional Shape", Krakow, Poland, September 10-15, 2017.

3. **S. Kang**, M. Furushima, H. Asakura, A. Habib, Y. Kim, B. Tomiyasu and M. Owari, 7th international symposium on practical surface analysis (PSA-16), "Development of new shave-off simulation method considering the angel between primary ion beam and sample surface", Daejeon, Korea, October 16-21, 2016.

## Acknowledgements

First of all, I would like to thank Professor Owari for supervising my doctoral course for the past three years. I have been received his willingness to help and support for this study and many writing things out. He always came to our request and taught us about problems. I have appreciated all that he has done for me.

I would like to thank my dissertation committee, Professor Tatsuma, Professor Fujioka, Professor Mawatari, Professor Sakamoto for reviews of my dissertation and valuable their suggestions.

Furthermore, I would like to thank Dr. Tomiyasu for guiding and his willingness to help over the past three years. Without his help, I would still be in a lot of technical trouble with the SIMS apparatus at F-basement.

I would like to thank all the former and current our laboratory members for very kind helpful encouragement and support. Dr. 金潤, Professor Ahsan Habib, 古島 弥来, 平井悠太郎, 浅倉 浩之, 江川 拓也, 高木 雄斗, 東 岳輝, 鈴木 匠, 松村 康平, Chen Sunwei, 岸 真之輔, 村上 諒. My experience and study at IIS would have been impossible without them. They had kindly taught me lots of things including Japan & Japanese. Especially, our SIMS group members have been very helpful for their technical support. Although not included in this paper, we had spent most of the time to repair the old machine. Now that I think about it, we had changed and fixed all of the FIB things. I am still strange why it was broken one by one, but we had a good and funny time and learned new techniques that had not previously experienced.

I would like to thank my friends in Korea for their encouragement. I am especially grateful to Jieun Kim. If she were not here, I would not have been enjoyed away from my daily routine on this campus. I was so lucky to be in Tokyo with her.

Finally, I must thank my husband, Seunghyuk Lee for his support and believing in me. Even he has also been a busy time for his study, he has always been a kind husband and a respectable friend to me.
I also thank all of my family. Thanks to them, I could be leaving everything behind and focusing only on Japan life.

This dissertation would not have been possible without the support of many people.
Dear all, I will never forget your help and our time together in the Owari Lab.